

Modelling and Control of a Scaled Car In and Beyond Stable Limit Handling

M.C.W. Baars



Modelling and Control of a Scaled Car In and Beyond Stable Limit Handling

MASTER OF SCIENCE THESIS

For the degree of Master of Science in Systems and Control at Delft
University of Technology

M.C.W. Baars

May 18, 2018

Faculty of Mechanical, Maritime and Materials Engineering (3mE) · Delft University of
Technology

DELFT UNIVERSITY OF TECHNOLOGY
DEPARTMENT OF
DELFT CENTER FOR SYSTEMS AND CONTROL (DCSC)

The undersigned hereby certify that they have read and recommend to the Faculty of
Mechanical, Maritime and Materials Engineering (3mE) for acceptance a thesis
entitled

MODELLING AND CONTROL OF A SCALED CAR IN AND BEYOND STABLE LIMIT
HANDLING

by

M.C.W. BAARS

in partial fulfillment of the requirements for the degree of

MASTER OF SCIENCE SYSTEMS AND CONTROL

Dated: May 18, 2018

Supervisor(s):

Prof. dr. ir. J. Hellendoorn

Dr. M. Alirezaei

Reader(s):

Dr. B. Shyrokau

Dr. W. Pan

Abstract

Over the past century, cars have become the most important means of transportation. With the increasing number of vehicles on the road, safety has become an important topic. The introduction of driver assistance systems, like Electronic Stability Control, has led to a significant decrease in fatal accidents. By preventing the vehicle from entering unstable behaviour, it remains controllable for the average driver. In rally racing, though, unstable manoeuvres, like drifting, are widely used for improved agility on low friction surfaces and in sharp corners. The average driver, however, is unable to perform such a manoeuvre safely.

With the development of autonomous driving systems, steps are taken to increase driver safety by removing the effects of human error. By taking over full control of the vehicle, these systems do not need to consider the driving skills of the average driver. Furthermore, the driving skills of the autonomous driving system are a result of its design. The autonomous driving system could, therefore, be designed to use advanced driver techniques, like drifting, to increase the safety of the passengers and other road users.

The objective of this research is to develop a vehicle controller that is capable of path-tracking within and beyond the limits of stable handling. To reduce the costs of testing, the controller is developed for an experimental platform in the form of a 1/10 scale radio controlled car. A nonlinear vehicle model of the scaled vehicle is developed and analysed regarding unstable vehicle behaviour. Since the behaviour and actuation of a vehicle differ in typical cornering and limit handling conditions, two separate controllers are used. In typical cornering conditions, a steering controller is used for path-tracking. Beyond stable limit handling, the lateral motion is actuated by both the steering angle and throttle input. A drift controller is used to determine the appropriate actuator inputs to sustain the drift, based on the yaw rate and direction of motion. The main contribution of this research is an extension of that controller to add path-tracking capabilities. Simulation analysis shows the controller can enter and sustain a drift, while successfully tracking the given path. Implementation of the controller in the scaled car shows great path-tracking performance in typical cornering conditions. Furthermore, the controller is able to, on command, make the vehicle enter and sustain a drift.

Contents

| | | |
|----------|---|-----------|
| 1 | Introduction | 1 |
| 1-1 | The limits of stable handling | 2 |
| 1-2 | Control of a drifting vehicle | 4 |
| 1-3 | Implementation of a drift controller | 5 |
| 1-4 | Research objectives | 6 |
| 1-5 | Thesis outline | 6 |
| 2 | Vehicle modelling | 7 |
| 2-1 | Model complexity | 7 |
| 2-2 | Vehicle model definition | 8 |
| 2-2-1 | Equations of motion | 9 |
| 2-2-2 | Load transfer | 10 |
| 2-2-3 | Tyre modelling | 10 |
| 2-2-4 | Compliance and play | 11 |
| 3 | Vehicle model identification | 13 |
| 3-1 | Measurement | 13 |
| 3-2 | Actuator modelling | 14 |
| 3-2-1 | Steering dynamics | 14 |
| 3-2-2 | Motor dynamics | 16 |
| 3-3 | Axle modelling | 18 |
| 3-4 | Tyre modelling | 20 |
| 3-4-1 | Cornering stiffness and yaw moment of inertia | 20 |
| 3-4-2 | Longitudinal tyre dynamics | 22 |
| 3-4-3 | Combined tyre dynamics | 23 |
| 3-5 | Full vehicle model validation | 26 |

| | |
|--|-----------|
| 4 Vehicle model analysis | 29 |
| 4-1 Phase trajectories | 29 |
| 4-2 Combined tyre slip | 32 |
| 4-3 Drift equilibria | 33 |
| 5 Vehicle Control | 37 |
| 5-1 Error definition | 37 |
| 5-2 Controller structure | 39 |
| 5-3 Typical cornering | 40 |
| 5-3-1 Lateral control | 40 |
| 5-3-2 Longitudinal control | 41 |
| 5-4 Drift controller | 41 |
| 5-4-1 Controller definition | 42 |
| 5-4-2 Control input coordination | 46 |
| 6 Simulation | 49 |
| 6-1 Typical cornering controller | 49 |
| 6-2 Drift controller | 50 |
| 6-2-1 Sensitivity analysis | 51 |
| 6-3 Entering the drift | 59 |
| 7 Implementation | 65 |
| 7-1 Actuator control and sensor reading | 65 |
| 7-2 State estimation | 66 |
| 7-2-1 Accelerations and yaw rate | 66 |
| 7-2-2 Wheel speeds | 67 |
| 7-2-3 Position | 67 |
| 7-2-4 Heading | 69 |
| 7-2-5 Velocities | 69 |
| 7-3 Implementation in the Delft Scaled Vehicle (DSV) | 70 |
| 7-3-1 Typical cornering with Lidar | 70 |
| 7-3-2 Typical cornering with Motion capture system | 72 |
| 7-3-3 Drifting | 74 |
| 8 Conclusions and recommendations | 77 |
| 8-1 Conclusions | 77 |
| 8-2 Recommendations for future work | 78 |

| | |
|---|------------|
| A System identification | 81 |
| A-1 Actuator dynamics | 81 |
| A-1-1 Steering dynamics | 81 |
| A-1-2 Motor dynamics | 82 |
| A-2 Axle and tyre modelling | 86 |
| A-2-1 Axle friction | 86 |
| A-2-2 Cornering stiffness and yaw moment of inertia | 88 |
| A-2-3 Longitudinal tyre dynamics | 90 |
| A-2-4 Combined tyre dynamics | 93 |
| A-2-5 Full vehicle model validation | 95 |
| B Comparison between desired curvature definitions | 97 |
| Glossary | 105 |
| List of Acronyms | 105 |
| List of Symbols | 105 |

List of Figures

| | | |
|------|--|----|
| 1-1 | The friction ellipse, formed by the tyre force limit. | 2 |
| 1-2 | | 3 |
| 2-1 | Vehicle model schematic | 9 |
| 3-1 | Servo dynamics model schematic | 14 |
| 3-2 | Ackerman geometry | 15 |
| 3-3 | Steady-state steering relationship | 15 |
| 3-4 | Manoeuvre for motor parameters estimation: Slowly increasing throttle input for free rotating rear wheels. | 17 |
| 3-5 | Manoeuvre for motor parameters estimation: Circular driving with increasing throttle input. | 18 |
| 3-6 | Dynamic and static friction estimation for front and rear axle | 19 |
| 3-7 | Rear axle moment of inertia estimation based on a free rolling vehicle. | 20 |
| 3-8 | Estimated linear bicycle model versus measurement data. Driving at a fixed throttle input and a sine steering input. | 21 |
| 3-9 | Longitudinal tyre force versus pure longitudinal wheel slip | 22 |
| 3-10 | Estimated longitudinal dynamics versus measurement data. Sine throttle input. . | 23 |
| 3-11 | Lateral tyre force versus wheel slip angle for the front wheels | 24 |
| 3-12 | Estimated combined tyre dynamics versus measurement data. Varying motor and steering inputs. | 25 |
| 3-13 | Estimated combined tyre dynamics versus measurement data. Varying motor and steering inputs. | 25 |
| 3-14 | Closed-loop vehicle model schematic | 26 |
| 3-15 | Manoeuvre for motor parameters estimation: Varying steering inputs for a near constant throttle input. | 27 |
| 3-16 | Manoeuvre for motor parameters estimation: Varying motor and steering inputs. | 27 |

| | | |
|------|--|----|
| 4-1 | Phase portrait for initial velocity $v = 1.5$ m/s and steering angle $\delta = 0^\circ$. The marker stable (○) and unstable (□,△) drift equilibria | 30 |
| 4-2 | Phase portrait for initial velocity $v = 1.5$ m/s and steering angle $\delta = 6^\circ$ and $\delta = 11^\circ$ | 31 |
| 4-3 | Representation of the three equilibria for a steering angle of $\delta = 6^\circ$ and a velocity of 1.5 m/s | 31 |
| 4-4 | Influence of a wheel slip angle on the longitudinal tyre force and influence of longitudinal wheel slip on the lateral tyre force. | 32 |
| 4-5 | Friction ellipse of the rear wheel at a load of 6.2 N | 33 |
| 4-6 | Equilibrium analysis for $v = 1.8$ m/s | 34 |
| 4-7 | Comparison between maximum curvature for typical cornering and drifting, at a velocity of 1.8 m/s. | 35 |
| 5-1 | Various look-ahead error definitions | 38 |
| 5-2 | Two problems arising when using the look-ahead error definition from Equation 5-1 at large body sideslip angles. | 38 |
| 5-3 | Path-tracking error definition as used in this research | 39 |
| 5-4 | Controller structure | 39 |
| 5-5 | The feedback-curvature based on the look-ahead error | 41 |
| 5-6 | The feedback-curvature based on the look-ahead error | 43 |
| 5-7 | Comparison between two definitions of the desired curvature, with (1) the path curvature, (2) the desired curvature, as used in the typical cornering conditions, and (3) the desired curvature used in drift conditions | 44 |
| 6-1 | Response of the vehicle to initial offsets in lateral position and orientation | 52 |
| 6-2 | Phase plot of the response of the vehicle to initial offsets in lateral position and orientation | 52 |
| 6-3 | Response of the vehicle to perturbations in body sideslip angle and yaw rate | 54 |
| 6-4 | Phase plot of response of the vehicle to perturbations in body sideslip angle and yaw rate | 54 |
| 6-5 | Range of equilibria, around the tuned equilibrium, where the controller succeeds in stabilising the vehicle | 55 |
| 6-6 | Steady-state lateral error for various drift equilibria | 55 |
| 6-7 | Equilibrium body sideslip angle and yaw rate for different velocities | 56 |
| 6-8 | Response of the failing stabilisation of the vehicle at an equilibrium point with $v_{des} = 1.8$ m/s and $\beta^{eq} = -0.26$ rad. | 57 |
| 6-9 | Response for changes in tyre-road friction | 58 |
| 6-10 | Response for changes in cornering stiffness | 59 |
| 6-11 | Comparison between direct switching and delayed switching to transfer the vehicle from typical cornering conditions to the reference drift equilibrium. | 60 |
| 6-12 | The transition from straight-ahead driving to drifting in a circle. | 63 |
| 6-13 | Trajectory of the transition from straight-ahead driving to drifting in a circle | 63 |
| 7-1 | The DSV. With 1: Arduino, 2: Lidar, 3: Onboard computer, 4: IMU, 5: Router, 6: Battery, 7: Servo, 8: Motor controller, 9: Motor, 10: Encoders. | 66 |

| | | |
|------|--|----|
| 7-2 | Position estimation from a polynomial fit to current and previous poses | 68 |
| 7-3 | Trajectory of the implemented typical cornering controller, segment 1 and 2 | 71 |
| 7-4 | Trajectory of the implemented typical cornering controller, segment 3, 4 and 5 | 71 |
| 7-5 | Path-tracking errors of the implemented typical cornering controller with Lidar | 71 |
| 7-6 | Trajectory of the implemented typical cornering controller with Motion capture system | 73 |
| 7-7 | Path-tracking errors of the implemented typical cornering controller with Motion capture system | 73 |
| 7-8 | States, path-tracking errors and control inputs during a drifting manoeuvre with the DSV | 75 |
| 7-9 | Driven trajectory during a drifting manoeuvre with the DSV | 75 |
| A-1 | Steering input and duration of steering action of servo dynamics test | 81 |
| A-2 | Manoeuvre for motor parameters estimation: Circular driving with increasing motor input. | 82 |
| A-3 | Manoeuvre for motor parameters estimation: Fixed motor input of 100 from rest. | 82 |
| A-4 | Manoeuvre for motor parameters estimation: Sine motor input. Frequency: 0.8 Hz, Amplitude: 6, Lowest value: 95.5 | 83 |
| A-5 | Manoeuvre for motor parameters estimation: Oval driving with throttle release. | 83 |
| A-6 | Manoeuvre for motor parameters estimation: Sine motor input. Frequency: 0.8 Hz, Amplitude: 5, Lowest value: 95.5 | 84 |
| A-7 | Manoeuvre for motor parameters estimation: Sine motor input. Frequency: 1 Hz, Amplitude: 7, Lowest value: 95.5 | 84 |
| A-8 | Manoeuvre for motor parameters estimation: Slowly increasing motor input for free rotating rear wheels. | 85 |
| A-9 | Manoeuvre for motor parameters estimation: Various step inputs for free rotating wheels. | 85 |
| A-10 | Measurement data used for axle friction estimation: Decreasing angular velocity of free rotating front axle. | 86 |
| A-11 | Measurement data used for axle friction estimation: Decreasing angular velocity of free rotating rear axle. | 86 |
| A-12 | Measurement data used for axle friction estimation: Decreasing velocity of free rolling vehicle. | 87 |
| A-13 | Measurement data used for axle friction estimation: Decreasing velocity of free rolling vehicle. | 87 |
| A-14 | Measurement data used for axle friction estimation: Decreasing velocity of free rolling vehicle. | 87 |
| A-15 | Manoeuvre used for linear cornering stiffness estimation: Driving with a fixed steering input of 77 and a slowly increasing longitudinal velocity. | 88 |
| A-16 | Manoeuvre used for linear cornering stiffness estimation: Driving with a fixed steering input of 103 and a slowly increasing longitudinal velocity. | 88 |
| A-17 | Manoeuvre used for linear cornering stiffness estimation: Driving at a fixed motor input and a sine steering input. Frequency: 0.4 Hz, Steering input range: 67 – 113 | 89 |
| A-18 | Manoeuvre used for linear cornering stiffness estimation: Driving at a fixed motor input and a sine steering input. Frequency: 0.24 Hz, Steering input range: 70 – 110 | 89 |
| A-19 | Manoeuvre used for linear cornering stiffness estimation: Driving at a fixed motor input and a sine steering input. Frequency: 0.4 Hz, Steering input range: 70 – 110 | 90 |

| | |
|--|----|
| A-20 Manoeuvre used for longitudinal tyre stiffness estimation: Sine motor input. Frequency: 0.8 Hz, Amplitude: 6, Lowest value: 95.5 | 90 |
| A-21 Manoeuvre used for longitudinal tyre stiffness estimation: Sine motor input. Frequency: 0.95 Hz, Amplitude: 5, Lowest value: 95.5 | 91 |
| A-22 Manoeuvre used for longitudinal tyre stiffness estimation: Fixed motor input of 100 | 91 |
| A-23 Manoeuvre used for longitudinal tyre stiffness estimation: Sine motor input. Frequency: 0.95 Hz, Amplitude: 7, Lowest value: 95.5 | 92 |
| A-24 Manoeuvre used for longitudinal tyre stiffness estimation: Sine motor input. Frequency: 0.6 Hz, Amplitude: 7, Lowest value: 95.5 | 92 |
| A-25 Manoeuvre used for combined tyre dynamics estimation: Varying motor and steering inputs | 93 |
| A-26 Manoeuvre used for combined tyre dynamics estimation: Low lateral acceleration, constant steering angle, slowly increasing velocity | 93 |
| A-27 Manoeuvre used for combined tyre dynamics estimation: Sine steering input. Frequency: 0.4 Hz, Steering input range: 70 – 110 | 94 |
| A-28 Manoeuvre used for combined tyre dynamics estimation: Varying motor and steering inputs. | 94 |
| A-29 Manoeuvre for motor parameters estimation: Varying steering inputs for a near constant motor input. | 95 |
| A-30 Manoeuvre for motor parameters estimation: Circular driving with increasing motor input. | 95 |
| A-31 Manoeuvre for motor parameters estimation: Varying motor and steering inputs. | 96 |
| B-1 Comparison between the desired curvature used in the typical cornering and drift controller for a small corner radius. | 98 |
| B-2 Response of the path tracking errors for the drift controller with the modified desired curvature definition. | 99 |
| B-3 Response of the path tracking errors for the drift controller with the original desired curvature definition. | 99 |

List of Tables

| | | |
|-----|--|----|
| 2-1 | List of symbols used in the vehicle model | 9 |
| 3-1 | Measured parameters of the DSV | 13 |
| 3-2 | Parameter estimation results of the motor dynamics | 17 |
| 3-3 | Front axle friction values and rear axle scaled friction | 19 |
| 3-4 | Rear axle moment of inertia and friction values | 20 |
| 3-5 | Estimation results cornering stiffnesses and yaw moment of inertia | 21 |
| 3-6 | Parameter estimation results of the 5 degrees of freedom longitudinal dynamics . | 23 |
| 3-7 | Parameter estimation results 5 degrees of freedom (DOF) combined slip behaviour | 24 |
| 6-1 | Controller gains for the typical cornering controller | 50 |
| 6-2 | Equilibrium point to which the controller is tuned | 51 |
| 6-3 | Controller gains of the drift controller | 51 |
| 6-4 | Controller gains for the transition from typical cornering to drifting | 61 |
| 7-1 | Overview of sensor output frequencies and actuator input frequencies | 66 |
| 7-2 | Overview of the sensors used to estimate the vehicle states | 66 |
| 7-3 | Reference states for implementation of the drift controller | 74 |
| 7-4 | Controller gains of the implemented drift controller | 74 |

Chapter 1

Introduction

Over the past century, cars have transformed from luxury products for the lucky few to one of the most important means of transportation. Where over the years the technology used in cars has changed much, one thing has not changed; a human driver drives the car. In road accidents all around the world, every year around 1.25 million people lose their lives[1]. The vast majority of accidents involving cars can be assigned to human error, with loss of control being one of the main causes[2, 3]. The introduction of driver assistance systems like the Anti-lock Braking System and Electronic Stability Control has led to a significant decrease in fatal accidents and newer systems like Automated Emergency Braking and Lane Departure Warning show promising results[4, 5]. These driver assistance systems take over tasks from the driver and try to keep the vehicle in an easily controllable envelope to reduce the effects of human error. However, (temporarily) taking over full control of the vehicle, could reduce the fatalities even more[6].

In recent years, (semi-)autonomous driving systems have found their ways to public roads. The fleet of self-driving cars of *Waymo*, one of the largest players in the development self-driving technology, has driven nearly six million fully autonomous kilometres on public roads[7]. Car manufacturer *Tesla* was one of the first to bring (semi-)autonomous technology to the public with the *Autopilot*. This system can take over highway driving, including lane changes and cornering. In critical situations, however, the driver is asked to take back control. A lot of effort is put into improving the ability to detect hazardous situations as early as possible, so that they can be avoided. But, since avoiding is not always possible an autonomous driving system should be able to handle the situation without human interaction.

In critical driving situations, such as collision avoidance, the direction of motion of the vehicle often has to change quickly. A quick steering or braking action, however, can destabilise the vehicle and result in unexpected behaviour[8]. In current vehicles, Electronic Stability Control uses individual wheel braking to prevent the car from entering unstable behaviour, in which an average driver is unable to maintain control. A skilled driver, though, would not necessarily use the same technique to control the vehicle in such a situation. In rally racing, for example, extreme manoeuvres, like drifting, are regularly used to negotiate sharp turns at high velocities[9]. Drifting is a difficult and highly unstable cornering condition,

which, if controlled by an average driver, would likely result in a spinning vehicle. For that reason, systems like Electronic Stability Control try to prevent the vehicle from entering such behaviour. However, the fact that advanced drivers, in for example rally racing, make use of these unstable cornering conditions, implies that there is a benefit to driving outside of the safety envelope of current driver assistance systems. Considering an autonomous car is controlled by a computer instead of a human driver, the driving skills of the autonomous driving system are a result of its design. Using the driving techniques of advanced drivers as a reference for the development of an autonomous driving system, could, therefore, be the solution to making autonomous driving systems capable of dealing with all sorts of driving scenarios.

1-1 The limits of stable handling

A drifting vehicle is best characterised by sideways sliding, counter-steering front wheels and spinning rear wheels[10]. To understand why this manoeuvre is used by rally drivers, the physics behind it are investigated, starting at the spinning rear wheels.

Tyre forces are generated as result of slip between the tyre and road surface. This slip is described by a longitudinal slip factor, λ , and a wheel slip angle, α , which is the angle between the wheel's direction of motion and its longitudinal axis. The force a tyre can deliver to the road is limited, with its magnitude depending on load, friction and direction[11]. An increase in longitudinal wheel slip will result in a force increase in the longitudinal direction, whereas an increase in wheel slip angle will result in an increasing lateral tyre force. Moreover, a change in either of the slip factors will also affect the magnitude of the force in other direction. The relationship between the slip factors and the tyre force is nonlinear and complex, however, when the tyre force limits are reached (i.e. the tyre is saturated), the relationship becomes more insightful. The maximum force a tyre can deliver in any direction, can be described by an ellipse, called the friction ellipse.

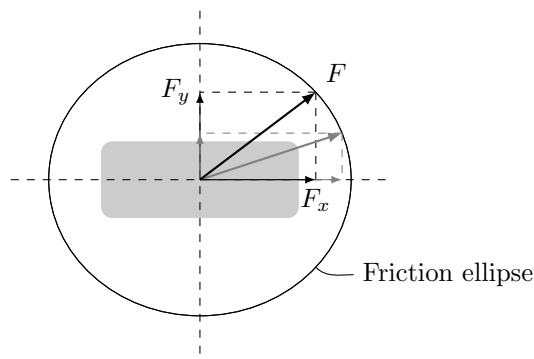


Figure 1-1: The friction ellipse, formed by the tyre force limit.

In Figure 1-1 the concept of the friction ellipse is visualised. The tyre force, F , is described in a longitudinal component, F_x , and a lateral component, F_y , and cannot exceed the friction ellipse. An increase in longitudinal tyre force, therefore, results in a decrease in lateral tyre force, as indicated by the grey arrows in the figure. This means that when a tyre is saturated,

the magnitude lateral of the tyre force can be manipulated by changing the longitudinal tyre force, which is achieved by altering the longitudinal wheel slip.

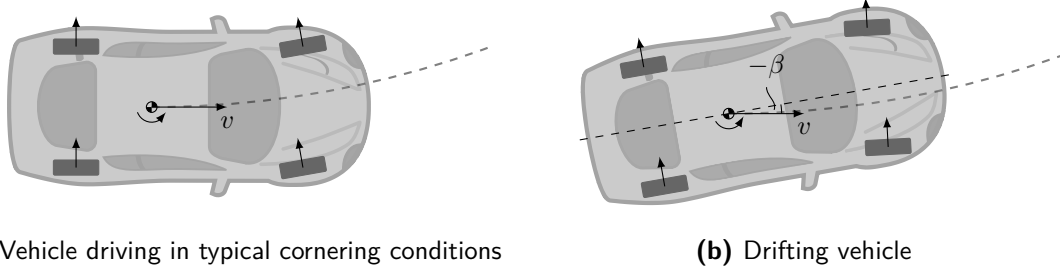


Figure 1-2

The forces between the four tyres and the road surface create a yaw moment around the centre of gravity of the vehicle. In Figure 1-2a a vehicle is shown that is driving in typical cornering conditions. The vehicle is moving forward with velocity v . Because the front wheels are steered to the left, they are slightly sliding sideways. This increased wheel slip angle results in a lateral tyre force. The yaw moment imposed by these forces make the vehicle rotate and drive in a certain curvature. Because of the rotation of the vehicle and the lateral accelerations resulting from the cornering motion, the rear tyres also generate a lateral tyre force. In typical cornering conditions, the opposing yaw moment created by the rear lateral tyre forces is large enough to prevent the vehicle from sliding sideways. When the rear wheels are spinning, however, the lateral tyre force has decreased due to the large longitudinal wheel slip, resulting in the rear-end of the vehicle sliding sideways. Since, in this situation, the rear tyres are saturated, the lateral tyre force can be manipulated by increasing or decreasing the longitudinal wheel slip. In other words, the yaw moment can now not only be controlled with the steering angle, but also with the throttle input on the rear wheels.

Since the lateral tyre forces of the rear wheels have decreased, the vehicle starts sliding sideways, and the direction of motion of the vehicle does not align with the centreline of the vehicle anymore. This situation is visualised in Figure 1-2b. The angle between the direction of motion and the centreline of the vehicle is the body sideslip angle, β . A positive angle means sliding to the left. To keep the vehicle at a certain body sideslip angle, the yaw moment around the vehicle has to be balanced. Since the rear lateral tyre forces have decreased, the front lateral tyre forces also have to decrease to prevent the vehicle from spinning. This is achieved by counter-steering, which means that the front wheels are steered to the right, while the vehicle is cornering to the left. The wheel slip angle of the front wheels decreases, and thus the lateral tyre forces too.

Drifting is a steady-state cornering condition, albeit an unstable one[12]. The instability makes drifting a challenging manoeuvre and the risks of losing control points out the danger for an average driver. On the other hand, drifting is widely used in rally racing to get around sharp corners as fast as possible[9]. An analysis of the sensitivity of drift equilibria gives some insight into the reasoning behind that.

During drifting the sensitivity of the vehicle motion to variations in friction is very low, compared to typical cornering near the friction limits[13]. Furthermore, an approximately linear relationship between the steering angle and body sideslip angle, with a slope independent of

both velocity and friction, is found[13]. Additionally, drifting provides the ability to negotiate sharper corners at an equal velocity, compared to typical cornering[14]. In other words, the response of a drifting vehicle is, to some extent, predictable and constant, even for varying friction. This is not only convenient in rally racing but can also be useful in collision avoidance manoeuvres. Chapter 4 elaborates on the behaviour of a drifting vehicle and provides a comprehensive insight into drift equilibria.

1-2 Control of a drifting vehicle

In typical cornering conditions, the lateral motion of a vehicle is only affected by the steering angle. The throttle input is only used to control the longitudinal motion. During drifting, the lateral motion is affected by both the steering angle and the throttle input[10]. Consequently, a controller developed for typical cornering conditions will be unable to control a drifting vehicle, since it does not take saturation of the rear wheels into account. A different control approach for drifting is, therefore, required.

Sustaining a drift does not necessarily require actively controlling both control inputs (steering angle and throttle) at the same time[10, 13]. Hindiyeh shows that with a constant rear longitudinal wheel slip, drift control based on the steering angle solely can maintain a drift and stabilise the vehicle when in danger of spinning[10]. When the vehicle is in danger of exiting the drift, however, the controller fails to prevent this. The yaw moment is controlled by the steering angle only. When the vehicle is in danger of exiting the drift, the yaw moment is increased by increasing the front lateral tyre forces. Since, however, these tyre forces are limited, a situation could occur where the front tyre cannot induce sufficient yaw moment to prevent the vehicle from exiting the drift. In this situation, a decrease in rear lateral tyre force is required[10]. A drift controller that uses only the throttle input and keeps the steering angle constant can stabilise the vehicle and prevent it from both spinning and exiting the drift. However, the throttle input affects not only the lateral tyre force, but also the longitudinal tyre force of the rear wheels. The use of this controller, therefore, results in large velocity variations[10]. For that reason, a combination of both control inputs is required.

In [10], a control approach is proposed that switches between the two controllers mentioned above. The controller is based on equations of motion and determines a combination of the front and rear lateral tyre forces to resolve the velocity, yaw rate and body sideslip errors. Initially, the throttle input is only used to control the longitudinal velocity. Based on the velocity error, a desired rear longitudinal wheel slip is determined. A low-level wheel slip controller brings the longitudinal wheel slip to its desired value via the throttle input. With the resulting rear longitudinal wheel slip, the rear lateral tyre force can be estimated. This tyre force is then used to determine the desired steering angle. In the case that the required front lateral force cannot be reached, due to tyre saturation or actuator limits, the throttle input is used to control the drift. The proposed controller is very simplistic; it is based solely on model equations and proportional feedback control. Nevertheless, it performs great in maintaining a sustained drift, albeit only in a limited range of equilibria.

Alternatively, Nonlinear Model Predictive Control (NMPC) can be used to find the control inputs corresponding to the determined combination of tyre forces[15]. NMPC uses a vehicle model to predict the future motion of the vehicle. By comparing the responses of different

control inputs, an optimal input sequence can be found. Additional to controlling the vehicle in a drift, this controller is shown to be able to follow a predefined path simultaneously. By the addition of estimated safety regions, the proposed controller can decide between typical cornering and drifting conditions, while keeping the vehicle within the controllable region. Although this controller showed tremendous results, a large amount of computational power is required to implement this controller real-time. Addition of varying driving conditions and higher model complexities will, therefore, be difficult.

In [16] the control problem is approached differently. In both the typical cornering as the high sideslip conditions, the same steering controller is used. This steering controller takes care of path-tracking by minimising the lateral distance to the path and difference in orientation between the vehicle and the path. The throttle input is used to control the yaw rate, sideslip angle and velocity to their desired equilibrium values. A State-Dependent Riccati Equation (SDRE) controller is used to find the optimal controller gains, in real-time. Even with the simple control structure, where the throttle input during drifting was only based on feedback, the SDRE controller was able to maintain a drift in changing conditions. However, this control method is little insightful, since the feedback gains are a result of an optimisation process. Understanding the behaviour and improving the performance of this controller is shown to be difficult.

Controlling a drifting vehicle can be achieved by various control approaches. Even though the NMPC approach in [15] showed tremendous performance in combined path-tracking and drifting, the required computational resources for real-time application are a large drawback. The SDRE controller proposed in [16] showed promising results even though it was only based on simple error dynamics. However, improvement of the performance is shown to be difficult, since it is little insightful. The approach, proposed in [10], is unable to follow a path but is able to maintain a drift with a simple controller based on the vehicles equations of motion and proportional control only. Addition of path-tracking capabilities to this controller could, therefore, be a basis for a simpler and more insightful drift controller.

1-3 Implementation of a drift controller

Before an autonomous driving system is allowed on public roads, the system has to go through a range of tests. Performing tests with an actual vehicle, however, could run into high costs. For that reason, an experimental platform, in the form of a 1/10 scale Radio Controlled (RC) car, is developed at the Delft Center for Systems and Control (DCSC). The Delft Scaled Vehicle (DSV) is rear wheel driven, has low grip 'drifting'-tyres and is equipped with multiple sensors; an Inertial Measurement Unit (IMU) for measurement of horizontal accelerations, yaw rate and orientation, encoders in every wheel for wheel speed measurement and a Light Detection And Ranging (Lidar) sensor for position and velocity estimation. The sensors and control inputs of the vehicle are connected to an onboard computer running the Robotic Operating System (ROS), enabling closed-loop vehicle control and sensor reading. The sensors and systems on the DSV are explained in detail in chapter 7.

1-4 Research objectives

The main goal of this research is the development of a lateral controller, capable of path-tracking in both typical cornering and high body sideslip conditions. The controller will be designed for implementation in the DSV. Therefore, a system identification needs to be performed. The objectives of this master thesis are formulated as follows:

- Develop a vehicle model that can accurately simulate the DSV's nonlinear behaviour;
- Design a lateral controller that
 - can follow a given feasible path in both typical cornering and high body sideslip conditions, given that
 - can intentionally enter a drift,
 - is simple and insightful by deducing the error dynamics from equations of motion;
- Evaluate the controller in a simulation environment, considering real-time implementation constraints;

1-5 Thesis outline

The main body of this thesis is structured as follows; Chapter 2 describes the requirements and the definition of the vehicle model used to model the DSV. The estimation process of the parameters of the vehicle model is discussed in chapter 3. Next, the resulting vehicle model is analysed regarding vehicle behaviour within and beyond the limits of stable handling in chapter 4. After that, the drift controller is defined in chapter 5. This controller is implemented and evaluated in a simulation environment, the results are discussed in chapter 6. Subsequently, the steps taken to implement the controller in the DSV and the results of the implementation are discussed in chapter 7. Finally, the conclusions are drawn, and recommendations for future work are given in chapter 8.

Chapter 2

Vehicle modelling

In this chapter, the vehicle model for the Delft Scaled Vehicle (DSV) will be defined. First, an explanation of the model complexity will be given. After that, the vehicle model equations will be defined and explained.

2-1 Model complexity

The objective of this research is to develop a system that can control the motion of the DSV within and beyond the limits of stable handling. The vehicle model of the DSV should, therefore, be able to simulate the vehicle's behaviour in these driving conditions accurately. The DSV is built up out of many different parts. Taking the characteristics and effects of all of these parts into account would result in an overly complex vehicle model. The following assumptions are made to decrease the complexity of the vehicle model:

- The body of the vehicle is assumed to be a point mass at the centre of gravity with a roll, pitch and yaw moment of inertia.
- The road surface is assumed smooth and horizontal. The vertical motion of the vehicle body and the wheels, with respect to the road, is, therefore, neglected.
- The road surface is assumed homogeneous, the friction is, therefore, assumed constant,
- Experiments are performed at velocities below 3 m/s, the effects of air resistance are, therefore, be neglected.
- The steering angles of both front wheels are assumed to be equal.

With these assumptions, the vehicle motion can be described by nine degrees of freedom; longitudinal and lateral motion, three body rotations and four wheel rotations. The necessity of incorporating these degrees of freedom in a vehicle model depends on the vehicle and the planned driving conditions[17].

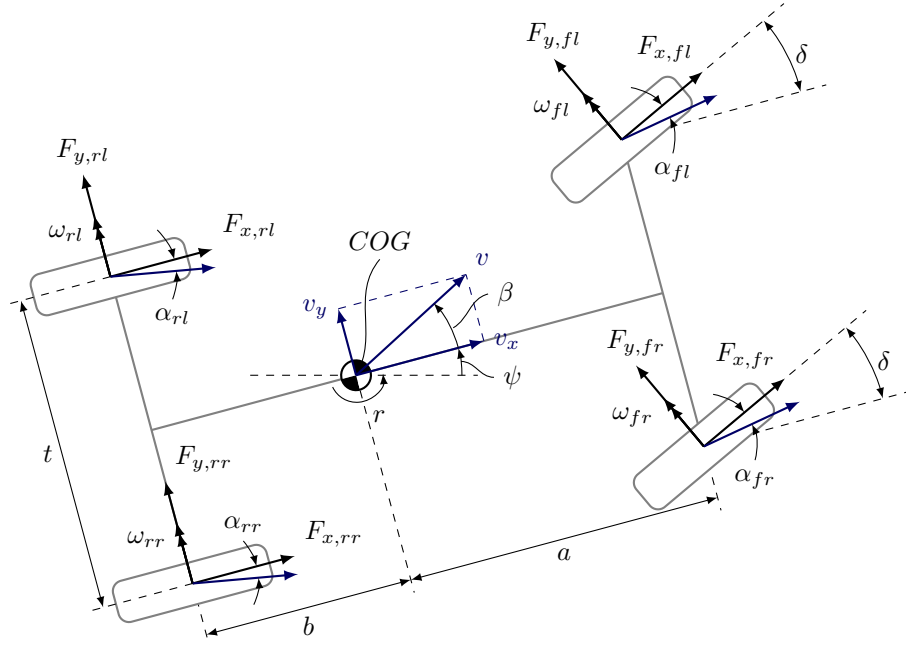
In driving conditions with lateral accelerations below $0.2g$, a two degrees of freedom bicycle model provides adequate modelling accuracy[17]. This model earns the name 'bicycle model' from the fact that the front and rear tyres are lumped together, resulting in a bicycle shape. Furthermore, only lateral motion, yaw motion and linear tyre characteristics are taken into account.

Beyond lateral accelerations of $0.2g$, the assumption of a constant velocity for a constant throttle becomes invalid due to wheel slip and high yaw rates. Longitudinal motion, therefore, needs to be taken into account. Furthermore, due to accelerations and roll and pitch motion, load transfer results in changing normal forces acting on the four tyres. The relationship between the force a tyre delivers and the normal force is nonlinear; the rate of change of maximum tyre force decreases with an increase in load [18]. Driving conditions with significant load changes, thus, require a vehicle model to include load transfer, i.e. roll and pitch motion and four separate wheels. Additionally, the force a tyre can deliver to the road is limited and nonlinear near these limits. During high lateral accelerations, the linear approximation will, therefore, be insufficient[17]. Moreover, the axle differential, placed at the powered axle, divides the available engine torque equally over the wheels, meaning that the longitudinal force of both wheels is never greater than the longitudinal force of the wheel with the lowest potential longitudinal force [16]. In combination with lateral load transfer, this results in a decrease in total longitudinal force for an increase in lateral acceleration. The effects of an axle differential should, therefore, be taken into account.

The driving conditions in which the DSV will be driven, include high lateral accelerations and tyre behaviour beyond the friction limits. For that reason, all above-mentioned characteristics need to be taken into account. However, an additional simplification is made, based on characteristics specific to the DSV. The high stiffness of the suspension results in little roll and pitch motion, and due to the low centre of gravity of the vehicle body, roll and pitch motion have a little influence on the load transfer. For that reason, the effects of roll and pitch motion are neglected.

2-2 Vehicle model definition

Following from the previous section, the resulting vehicle model should include longitudinal, lateral and yaw motion, load transfer and nonlinear tyre dynamics. In Figure 2-1 a schematic of the required vehicle model is shown, with the x -axis pointing in the longitudinal direction, the y -axis in the lateral direction and the z -axis pointing upwards. The four wheels are denoted by the subscripts fl , fr , rl and rr for the front-left, front-right, rear-left and rear-right wheel, respectively. The definitions of the symbols used in the vehicle model equations are summarised in Table 2-1.

**Figure 2-1:** Vehicle model schematic**Table 2-1:** List of symbols used in the vehicle model

| Symbol | Definition |
|------------|---|
| α_j | Wheel slip angle of wheel $j \in \{fl, fr, rl, rr\}$ |
| β | Body sideslip angle |
| δ | Steering angle |
| ψ | Vehicle heading |
| ω_j | Angular velocity of wheel $j \in \{fl, fr, rl, rr\}$ |
| a | Distance from the front axle to the Centre of Gravity (COG) |
| b | Distance from the rear axle to the COG |
| ℓ | Wheelbase ($\ell = a + b$) |
| t | Axle track |
| m | Vehicle mass |
| v | Vehicle velocity |
| v_x | Longitudinal velocity |
| v_y | Lateral velocity |
| $F_{i,j}$ | Tyre force in direction $i \in \{x, y, z\}$ of wheel $j \in \{fl, fr, rl, rr\}$ |
| I_z | Yaw moment of inertia at the COG |

2-2-1 Equations of motion

The equations of motion of the vehicle model describe the longitudinal, lateral and yaw motion and are given by

$$\dot{v}_x = \frac{1}{m} [(F_{x,fl} + F_{x,fr}) \cos \delta + F_{x,rl} + F_{x,rr} - (F_{y,fl} + F_{y,fr}) \sin \delta] + rv_y, \quad (2-1)$$

$$\dot{v}_y = \frac{1}{m} [(F_{y,fl} + F_{y,fr}) \cos \delta + F_{y,rl} + F_{y,rr} + (F_{x,fl} + F_{x,fr}) \sin \delta] - rv_x, \quad (2-2)$$

$$\begin{aligned} \dot{r} = \frac{1}{I_z} & [a((F_{y,fl} + F_{y,fr}) \cos \delta + (F_{x,fl} + F_{x,fr}) \sin \delta) - b(F_{y,rl} + F_{y,rr}) \\ & - \frac{t}{2}((F_{x,fl} - F_{x,fr}) \cos \delta - (F_{y,fl} - F_{y,fr}) \sin \delta + F_{x,rl} - F_{x,rr})], \end{aligned} \quad (2-3)$$

where m is the mass of the vehicle, $F_{i,j}$ denotes the tyre forces for direction i of wheel j , with $i \in \{x, y, z\}$ and $j \in \{fl, fr, rl, rr\}$, δ is the steering angle, r is the yaw rate, v_i is the velocity in direction i , I_z is the yaw moment of inertia at the centre of gravity and a and b are the distances from the centre of gravity to the front and rear axle, respectively.

2-2-2 Load transfer

The wheel loads on the four wheels, based on static load and load transfer due to accelerations, are defined by

$$\begin{aligned} F_{z,fl} &= \frac{1}{2} \frac{b}{\ell} mg - \frac{1}{2} \frac{h}{\ell t} ma_x + \frac{bh}{\ell t} ma_y, \quad F_{z,fr} = \frac{1}{2} \frac{b}{\ell} mg - \frac{1}{2} \frac{h}{\ell t} ma_x - \frac{bh}{\ell t} ma_y, \\ F_{z,rl} &= \frac{1}{2} \frac{a}{\ell} mg + \frac{1}{2} \frac{h}{\ell t} ma_x + \frac{ah}{\ell t} ma_y, \quad F_{z,rr} = \frac{1}{2} \frac{a}{\ell} mg + \frac{1}{2} \frac{h}{\ell t} ma_x - \frac{ah}{\ell t} ma_y, \end{aligned} \quad (2-4)$$

where ℓ is the wheelbase ($\ell = a + b$), h is the height of the centre of gravity, t the axle track (i.e. the distance between the centreline of two wheels) and a_i is the acceleration in direction i .

2-2-3 Tyre modelling

Tyre forces originate from slip between the tyre and the road surface. This slip is described by the longitudinal slip coefficient, λ_j , and the wheel slip angle, α_j , defined by

$$\lambda_j = \frac{|v_{x,j} - \omega_j R_e|}{\max(v_{x,j}, \omega_j R_e)} \quad (2-5)$$

and

$$\alpha_j = -\arctan\left(\frac{v_{y,j}}{v_{x,j}}\right), \quad (2-6)$$

where $v_{x,j}$ and $v_{y,j}$ are the longitudinal and lateral velocity of wheel j , respectively. The velocities at the four wheel hubs are given by

$$\begin{aligned} v_{x,left} &= v_x - \frac{t}{2}r, \quad v_{x,right} = v_x + \frac{t}{2}r, \\ v_{y,front} &= v_y + ar, \quad v_{y,rear} = v_y - br. \end{aligned} \quad (2-7)$$

Since the rear wheels are not steered, these velocities are the same as the velocities of the wheel. The velocities of the front wheels are calculated by

$$\begin{aligned} v_{x,fl/r} &= v_{x,left/right} \cos(\delta) - v_{y,front} \sin(\delta), \\ v_{y,fl/r} &= v_{x,left/right} \sin(\delta) + v_{y,front} \cos(\delta). \end{aligned} \quad (2-8)$$

At low longitudinal and lateral accelerations, the tyre behaviour can be approximated by a linear tyre model[17]. The linear relationship between the slip values and the tyre forces are given by

$$F_{x,j} = C_\sigma \lambda_j \quad \text{and} \quad F_{y,j} = C_\alpha \alpha_j, \quad (2-9)$$

where C_σ is the longitudinal tyre stiffness and C_α is the lateral tyre stiffness. At high acceleration manoeuvres, though, the linear relationship will be inaccurate, since it does not model tyre force limits and combined longitudinal and lateral slip behaviour. A nonlinear tyre model is required to model tyre characteristics at a larger operating range.

Nonlinear tyre models are available in various types and complexities. A widely used tyre model is the Magic Formula[19], which captures nonlinear tyre behaviour at high accuracy but requires a minimum of eight parameters to be estimated. In this research, a modified version of de Dugoff tyre model[11] is used, as proposed in [20], since it is able to capture nonlinear tyre dynamics with only three parameters to estimate. The modification adds the characteristics of a peak tyre force, which is not present in the regular Dugoff tyre model. The modification parameters are found by fitting the model to Magic Formula estimations of multiple tyres, resulting in a similar shape. Although the accuracy and flexibility in curve shape, of the modified Dugoff tyre model, are lower in comparison with the Magic Formula, the low number of parameters makes it preferable for this research. The modified Dugoff tyre model is defined by

$$F_x = C_\sigma \frac{\lambda}{\lambda+1} f(\theta) G_\sigma \quad \text{and} \quad F_y = C_\alpha \frac{\tan(\alpha)}{\lambda+1} f(\theta) G_\alpha, \quad (2-10)$$

with

$$f(\theta) = \begin{cases} \theta(2 - \theta) & \text{if } \theta < 1 \\ 1 & \text{if } \theta \geq 1 \end{cases}, \quad (2-11)$$

$$\theta = \frac{\mu F_z (1 + \lambda)}{2 \sqrt{(C_\sigma \lambda)^2 + (C_\alpha \tan(\alpha))^2}}, \quad (2-12)$$

$$G_\sigma = (1.15 - 0.75\mu)\lambda^2 - (1.63 - 0.75\mu)\lambda + 1.27, \quad (2-13)$$

$$G_\alpha = (\mu - 1.6) \tan \alpha + 1.155, \quad (2-14)$$

where μ is the tyre-road friction coefficient.

The forces estimated by the tyre model, are steady-state tyre forces. Actual tyre forces, however, are not applied instantaneously. Therefore transient tyre behaviour has to be taken into account. The transient behaviour is added by

$$\dot{F}_{i,trans} = \frac{(F_{i,ss} - F_{i,trans})v_{x,j}}{\sigma_{rl,i}}, \quad (2-15)$$

where $\sigma_{rl,i}$ is the relaxation length.

2-2-4 Compliance and play

The wheels of a vehicle are allowed to move in vertical direction and, in case of the front wheels, rotate around the vertical axis. While driving, however, the suspension and steering

system of a vehicle are subject to compliance and play. This means that the wheels can also move and rotate in other directions. Even though this movement is small, it influences the vehicle's behaviour[21]. At a high lateral acceleration, for example, the steering angle could slightly change, while the steering input remains equal. This change in steering angle results in a change wheel slip angle and, thus, a different lateral tyre force. In general, the influence of compliance and play result in a decreased axle stiffness. The effective lateral stiffness of the axle and wheels combined, is, therefore, lower than the cornering stiffness of the two wheels. Even though the four wheels are equal, the effective stiffness of the front and rear wheels is different, because of the differences in suspension. In chapter 3 the tyre parameters will be estimated based on driven manoeuvres. Since the compliance and play are not directly implemented in the vehicle model, the estimated cornering stiffnesses will be the effective stiffnesses. The front and rear wheels should, therefore, have a separate lateral stiffness parameter.

Chapter 3

Vehicle model identification

Values for the vehicle model parameters have to be estimated, to make the vehicle model respond like the Delft Scaled Vehicle (DSV). The estimation process is divided into multiple steps. First, the parameters that are directly measurable are obtained. Subsequently, the actuator dynamics are estimated. Next, the axle and tyre dynamics are estimated, and, finally, a full model validation is performed.

3-1 Measurement

A large part of the vehicle model parameters can be obtained by direct measurement. In Table 3-1 an overview of the measured parameters is shown.

Table 3-1: Measured parameters of the DSV

| Symbol | Value | Description |
|--------|--------------------------|--|
| m | 2.286 kg | Vehicle mass ¹ |
| m_f | 0.998 kg | Front axle load |
| m_r | 1.288 kg | Rear axle load |
| R_e | 0.0313 m | Effective wheel radius |
| t | 0.1515 m | Axle track |
| ℓ | 0.26 m | Wheelbase |
| a | 0.1465 m | Distance from COG to front axle |
| b | 0.1135 m | Distance from COG to rear axle |
| h | 0.054 m | Distance from COG to the road surface |
| m_w | 0.04 kg | Wheel mass |
| I_z | 0.04 kg · m ² | Initial estimate of the yaw moment of inertia based on the assumption of a homogeneous beam shape |

¹The mass of the vehicle includes the vehicle body with: battery, onboard computer, router, Arduino, Encoders and Inertial Measurement Unit (IMU). The weight of the Lidar is not taken into account.

3-2 Actuator modelling

3-2-1 Steering dynamics

A servo controls the steering angle of the front wheels of the vehicle. The input of the servo, u_s , can be varied from 65 to 115, with 90 as neutral position, resulting in a steering angle range of approximately -15 to 15 degrees². The dynamics of the steering system can be divided into two parts; from servo input to servo angle, δ_s , and from servo angle to steering angle, δ , as shown in Figure 3-1. First, the dynamics of the servo are estimated. After that, the relationship between the servo angle and the steering angle is found.

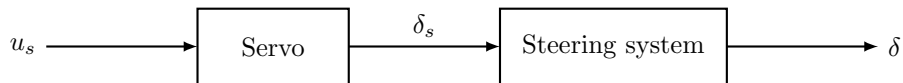


Figure 3-1: Servo dynamics model schematic

Servo dynamics

When a steering input is given, the servo starts rotating to the desired angle. The time it takes to reach the desired angle is based on the latency in the connection and the dynamics of the servo. By filming different steering actions in the full steering range, the duration of a change in steering angle can be found. Since equal changes in steering angle often resulted in different durations, the servo dynamics are fitted to the fastest steering behaviour measured (Figure A-1). A transfer function of the steering dynamics is given by

$$\delta_s = \frac{u_s}{0.035s + 1} \quad \text{with } |\dot{\delta}_s| \leq 380, \quad (3-1)$$

where $\dot{\delta}_s$ is the rate of change of the servo angle, which is limited to ± 380 deg/s.

Steady-state steering

The relationship between the servo angle and the steering angle can be obtained by direct measurement. However, due to a large amount of play in the system, the actual steering angle during driving will differ from this mentioned relationship. A more reliable method for the estimation of the steering relationship is via the Ackerman geometry[22]. By assuming low velocity and small wheel slip angles, and thus a small body sideslip angle, it can be assumed that perpendicular lines from each wheel cross each other in the same point, as shown in Figure 3-2. From this assumption, the steering angle can be estimated by

$$\tilde{\delta} = \arctan\left(\frac{\ell}{R}\right) \approx \left(\frac{\ell}{R}\right). \quad (3-2)$$

The radius of the driven curvature can be derived from the yaw rate and velocity by

$$R = \frac{v}{r} \approx \frac{v_x}{r}. \quad (3-3)$$

²At a later stage in the research, a larger steering range is made possible. This is, however, not taken into account in the system identification

Note that the longitudinal velocity, v_x , can only be assumed equal to the absolute velocity, v , for a small body sideslip angle. Substitution of Equation 3-3 in Equation 3-2 results in

$$\tilde{\delta} \approx \left(\frac{\ell r}{v_x} \right). \quad (3-4)$$

At steady-state, the servo input and servo angle are equal. The relationship between the servo angle and steering angle can, therefore, be found by finding the steady-state relationship between the servo input and steering angle. The vehicle is driven at multiple fixed steering angles, in the full steering range, at a velocity of approximately 0.7 m/s. The longitudinal velocity is derived from the angular velocities of the two front wheels. Since these are not powered, the longitudinal wheel slip approaches zero, and the longitudinal velocity can, thus, be estimated by

$$\tilde{v}_x \approx R_e \frac{\omega_{fl} + \omega_{fr}}{2}. \quad (3-5)$$

For all the servo inputs, the steady state-steering angle is estimated with Equation 3-4. The results are shown in Figure 3-3. A linear fit results in the following relationship:

$$\tilde{\delta} = -0.010042\delta_s + 0.899. \quad (3-6)$$

The final steering dynamics are formed by substitution of Equation 3-1 in Equation 3-6 and result in

$$\tilde{\delta} = -0.010042 \frac{u_s}{0.035s + 1} + 0.899 \quad \text{with} \quad |\dot{\delta}| \leq 3.816 \text{ deg/s}. \quad (3-7)$$

Additionally, Figure 3-3 also shows estimates of a dynamic steering angle. These points are obtained by driving with various sine inputs on the steering angle and estimated with the steering dynamics into account. In general, the dynamic steering angles are in correspondence with the steady-state steering relationship. Near the actuator limits, the effects of wheel slip become more apparent, resulting in the slight offset.

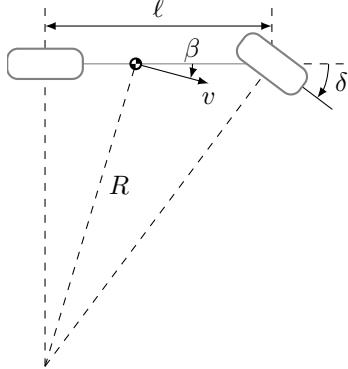


Figure 3-2: Ackerman geometry

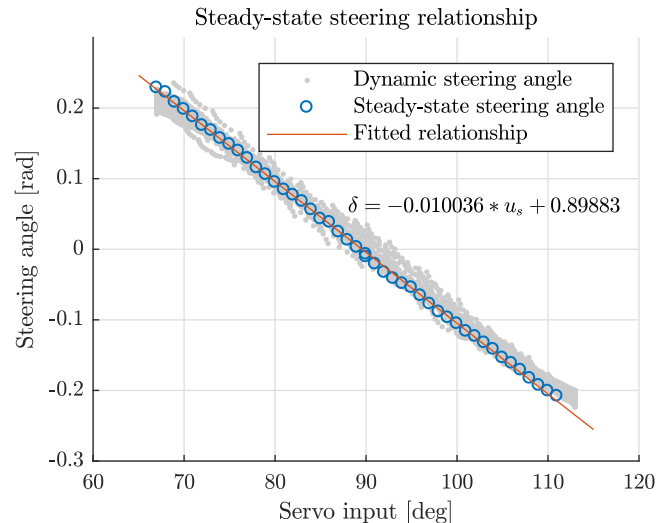


Figure 3-3: Steady-state steering relationship

3-2-2 Motor dynamics

The DSV is driven by a brushless DC motor, controlled by an Electric Speed Controller (ESC), which translates a Pulse Width Modulation (PWM) signal to a three-phase motor input. The throttle input signal (u_t) is scaled from 0 to 180, with 0 resulting in maximum reverse rotation, 90 in rest and 180 in maximum forward rotation. For indoor use, though, the maximum throttle input is limited to 110. The motor starts rotating at an input value of 95.5.

The amount of torque a brushless DC motor can deliver depends on the input power and the rotating speed. Since an ESC controls the motor, however, the relationship between the throttle input and the power delivery is unknown. The relationship between the torque and rotating speed of a brushless DC motor, in general, is approximately linear. But, during the estimation process, it became clear that adding a quadratic term improved the model accuracy. The torque equation of the motor, used for estimation is given by

$$T = (c_1 + c_2\omega_r + c_3\omega_r^2)(c_4 + c_5u_t + c_6u_t^2), \quad (3-8)$$

where c_k with $k \in \{1, 2, 3, 4, 5, 6\}$ are constants and ω_r is the average of the two rear wheel angular velocities. For the estimation, both datasets of free rotating rear wheels and driven manoeuvres are used. For the first type of datasets, the throttle input is taken as input and the rear wheel speed as output. For the second type of datasets, additionally the longitudinal velocity measurement is used. The following manoeuvres are used for the estimation:

- Slowly increasing throttle input for free rotation rear wheels
- Sine throttle input with different amplitudes and frequencies for a fixed steering angle
- Constant throttle input
- Varying throttle input

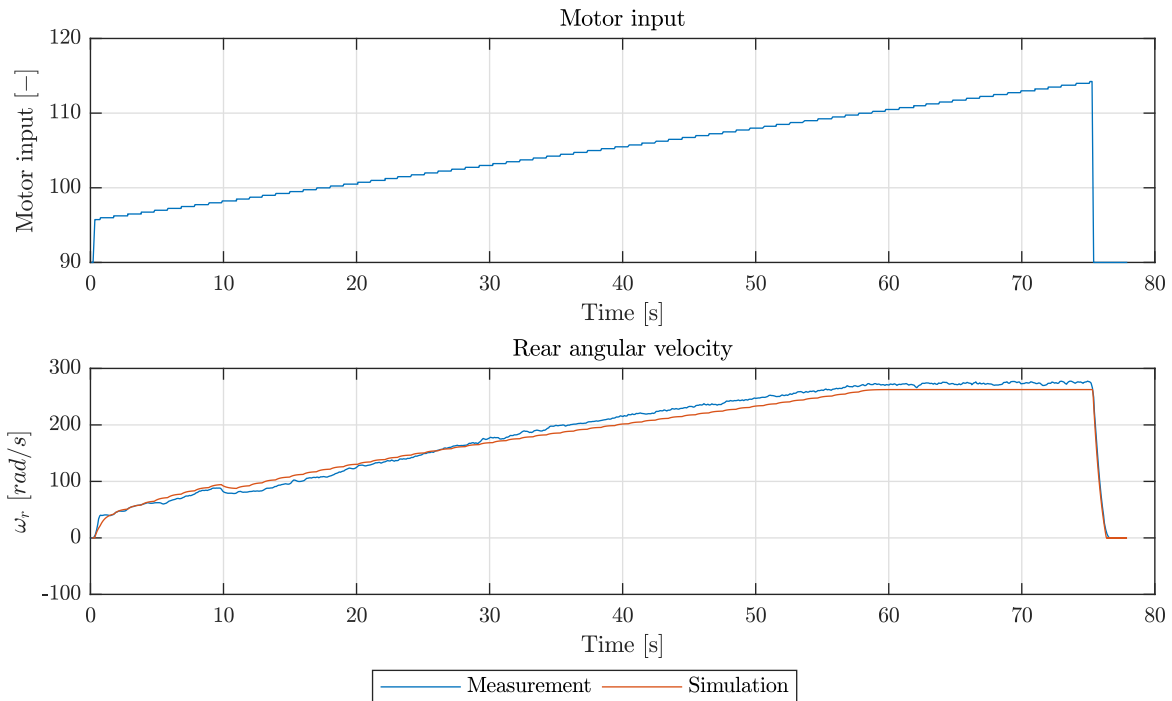
To use the measurements of driven manoeuvres, a model with longitudinal dynamics and tyre dynamics is required. The motor model is, therefore, the final part of the vehicle model to be estimated. The five degrees-of-freedom bicycle model and the parameters as found later in this chapter will be used for this estimation.

A nonlinear-least-squares optimisation is used together with the MATLAB parameter estimation toolbox to estimate the six motor model parameters. In Table 3-2 the found parameters are summarised. Figure 3-4 and Figure 3-5 show the response of three of the manoeuvres used for the estimation. In subsection A-1-2 responses of the other used manoeuvres are shown. The slowly increasing throttle input in figure Figure 3-4 is used to model the steady-state motor behaviour. The response of the simulation with free rotating wheels is, with a maximum difference of 5 percent, comparable to the measurement.

Table 3-2: Parameter estimation results of the motor dynamics

| Symbol | Value |
|--------|-----------------------|
| c_1 | 28.9266 |
| c_2 | -0.1335 |
| c_3 | $2.213 \cdot 10^{-4}$ |
| c_4 | 0.0017 |
| c_5 | $7.239 \cdot 10^{-4}$ |
| c_6 | $1.099 \cdot 10^{-5}$ |

In Figure 3-5, the response for a slowly increasing velocity, while driving, is shown. With this manoeuvre, a larger deviation between measured and simulated velocity is found, especially after 40 seconds. What happens at this time instant, though, also happens in the first figure at a simulation time of 10 seconds; the angular velocity decreases, while the throttle input keeps increasing. Around a throttle input of 98, the output torque of the motor drops, as if the throttle input jumped back to around 97. The size of this jump, however, is not constant, which is one of the characteristics that makes it difficult to model the motor dynamics accurately. Another difficulty is the influence of the state of charge of the battery, driving a fully charged battery results in a higher velocity than when driving at the same throttle input, with a half-empty battery. In the remainder of this research, however, the output of the motor will be controlled by a low-level wheel slip controller, which will compensate for the model mismatch and make sure the torque input is at the desired magnitude.

**Figure 3-4:** Manoeuvre for motor parameters estimation: Slowly increasing throttle input for free rotating rear wheels.

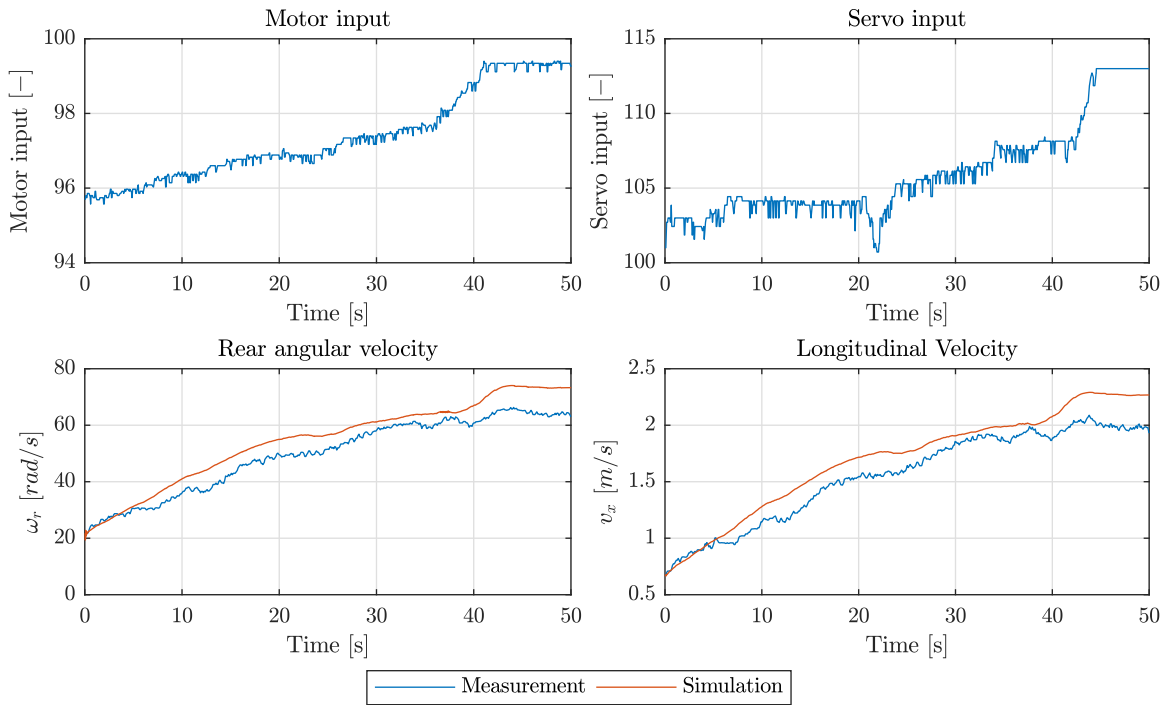


Figure 3-5: Manoeuvre for motor parameters estimation: Circular driving with increasing throttle input.

3-3 Axle modelling

The front and rear axle of the vehicle are subject to friction, both static and dynamic. Additionally, roll friction between the road and tyres is present. However, since both the tyres and the road surface are made of hard and smooth materials, the roll friction is neglected. The magnitude of the friction in the axle can be found by measuring the change in angular velocity of a free rotating wheel, after a rotational input. The wheel dynamics are given by

$$\dot{\omega} = \frac{T_m - F_x R_e - T_f}{I_w}, \quad (3-9)$$

where T_m is the torque input from the motor (only for the rear axle), F_x is the longitudinal tyre force, T_f is the torque resulting from friction and I_w the angular moment of inertia of the wheel including wheel hub. The torque resulting from friction is given by

$$T_f = \omega T_{f,dyn} + \text{sign}(\omega) T_{f,st}, \quad (3-10)$$

where $T_{f,dyn}$ is the friction dependent on the angular velocity and $T_{f,st}$ the static friction.

For a free rotating wheel, without actuation, the wheel dynamics result in

$$\dot{\omega} = \frac{-\omega T_{f,dyn} + \text{sign}(\omega) T_{f,st}}{I_w}. \quad (3-11)$$

The moment of inertia of the wheel is estimated with a 3D model of the wheel with equal weight and is approximately $4 \cdot 10^{-5} kg \cdot m^2$. For the rear wheels, however, the inertia is

higher due to the direct connection to the motor. Therefore, for the rear wheels, first the relationships $\frac{T_{f,dyn}}{I_w}$ and $\frac{T_{f,st}}{I_w}$ are estimated. After that the moment of inertia of the rear wheels is estimated.

A nonlinear least-squares optimisation method is used to estimate the friction parameters corresponding to the measurement data. The found parameters per wheel are shown in Table 3-3. In Figure 3-6a and Figure 3-6b, a comparison of the measured versus the simulated response for both the front and rear axle is shown. Other datasets which are used for this estimation can be found in subsection A-2-1. The found parameters show that the friction in the rear axle is much higher than the friction in the front axle, this is because the rear axle is directly connected to the motor, whereas the front wheels can rotate freely. This direct connection with the motor poses a difficulty in the estimation of the rear axle friction since the friction in the motor can be different during operation. However, since the motor can easily overcome the friction, the change in friction can be neglected.

Table 3-3: Front axle friction values and rear axle scaled friction

| Symbol | Value | Description |
|---------------------------|--|--|
| $I_{w,f}$ | $4 \cdot 10^{-5} \text{ kg} \cdot \text{m}^2$ | Front axle moment of inertia per wheel |
| $T_{f,dyn,f}$ | $1.477 \cdot 10^{-5} \text{ Nm} \cdot \text{s}/\text{rad}$ | Front axle dynamic friction per wheel |
| $T_{f,st,f}$ | $3.098 \cdot 10^{-4} \text{ Nm}$ | Front axle static friction per wheel |
| $\frac{T_{f,dyn,r}}{I_w}$ | 1.234 | Scaled rear axle dynamic friction |
| $\frac{T_{f,st,r}}{I_w}$ | 129.3 | Scaled rear axle static friction |

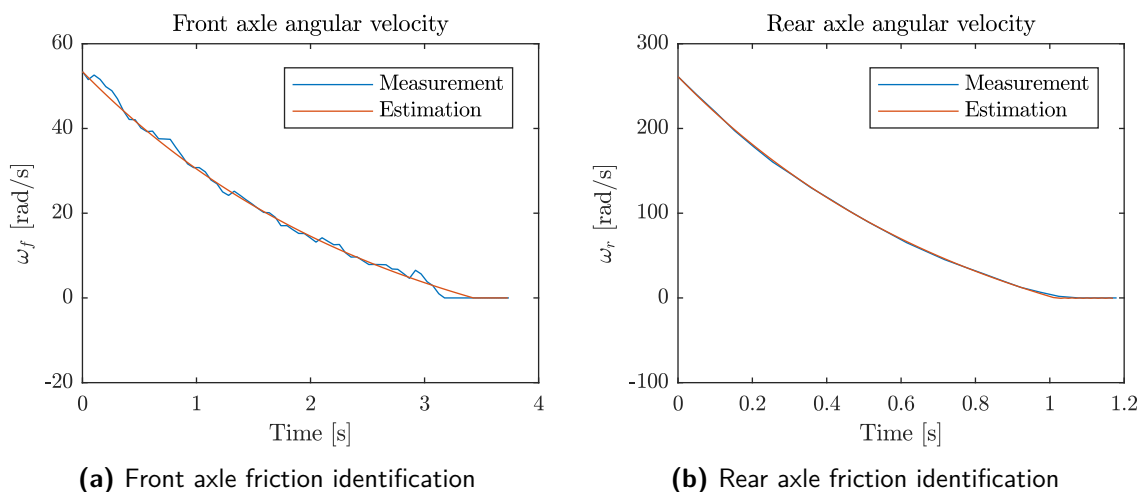


Figure 3-6: Dynamic and static friction estimation for front and rear axle

To find the moment of inertia of the rear axle, the deceleration of the vehicle, without actuation, is measured. In order to perform this test, however, knowledge about the longitudinal tyre forces is required. Therefore the vehicle parameters and model as used in subsection 3-4-2 are used. The resulting rear axle moment of inertia and corresponding friction values are shown in Table 3-4. Figure 3-7 shows one of the simulated response versus the measurement

of the decreasing velocity from the free rolling vehicle. In subsection A-2-1 the responses of other comparable measurements are shown.

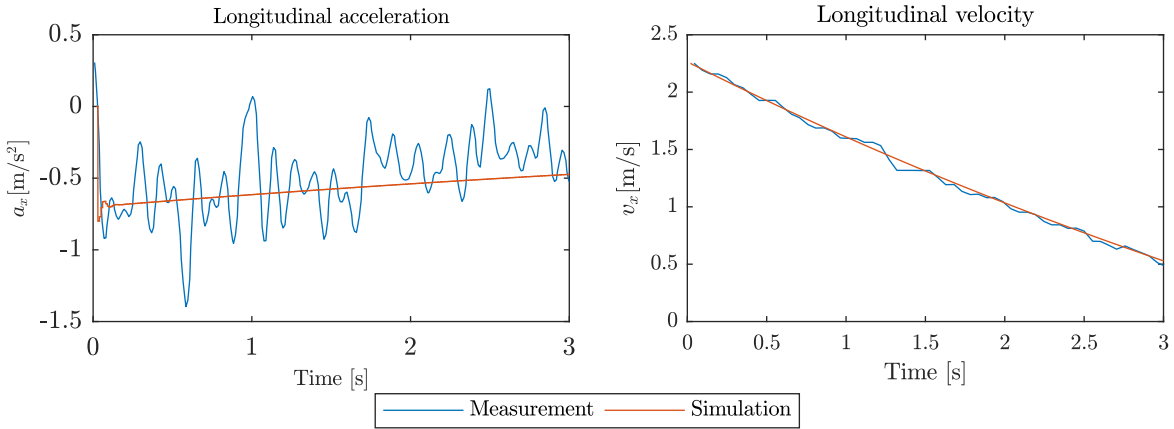


Figure 3-7: Rear axle moment of inertia estimation based on a free rolling vehicle.

Table 3-4: Rear axle moment of inertia and friction values

| Symbol | Value | Description |
|---------------|-----------------------------------|---------------------------------------|
| $I_{w,r}$ | $1.2559 \cdot 10^{-4}$ | Rear axle moment of inertia per wheel |
| $T_{f,dyn,r}$ | $1.5506 \cdot 10^{-4}$ Nm · s/rad | Rear axle dynamic friction per wheel |
| $T_{f,st,r}$ | 0.0162 Nm | Rear axle static friction per wheel |

3-4 Tyre modelling

3-4-1 Cornering stiffness and yaw moment of inertia

The simplest form of a vehicle model is the two degrees of freedom linear bicycle model, with its equations of motion given by

$$\dot{v}_y = -\frac{C_{\alpha,f} + C_{\alpha,r}}{mv_x} v_y + \frac{bC_{\alpha,r} - aC_{\alpha,f}}{mv_x} r + \frac{C_{\alpha,f}}{m} \delta - rv_x, \quad (3-12)$$

$$\dot{r} = \frac{bC_{\alpha,r} - aC_{\alpha,f}}{I_z v_x} v_x - \frac{b^2 C_{\alpha,r} + a^2 C_{\alpha,f}}{I_z v_x} r + \frac{aC_{\alpha,f}}{I_z} \delta. \quad (3-13)$$

With the linear bicycle model, it is possible to estimate the cornering stiffness and the yaw moment of inertia of the vehicle, all other parameters are known. Since this model is only accurate for low acceleration manoeuvres, the following two manoeuvres are used for estimation:

- Fixed steering angle with a slowly increasing longitudinal velocity
- Constant (low) velocity and a sine steer input

Both manoeuvres are performed multiple times with variations in steering angle, sine frequency and amplitude.

The control inputs of the two degrees-of-freedom linear bicycle model are the longitudinal velocity and steering angle. The measured outputs are the yaw rate, lateral acceleration and lateral velocity. Because of a large amount of noise in the acceleration measurements, and the lack of sensors to measure the lateral velocity, only the yaw rate is used in the optimisation process.

A nonlinear-least-squares optimisation and the parameter estimation toolbox of MATLAB are used to estimate the three model parameters. The found parameters are shown in Table 3-5. In Figure 3-8 a comparison of the measurement versus the simulation for one of the manoeuvres is shown. Figures of the other manoeuvres used in the estimation process are shown in subsection A-2-2.

The results show a large difference in front and rear cornering stiffness. This is probably due to the compliance and play in the steering system.

Table 3-5: Estimation results cornering stiffnesses and yaw moment of inertia

| Symbol | Value | Description |
|----------------|---------------------------|---------------------------|
| $C_{\alpha,f}$ | 18.13 N/rad | Front cornering stiffness |
| $C_{\alpha,r}$ | 30.08 N/rad | Rear cornering stiffness |
| I_z | 0.042 kg · m ² | Yaw moment of inertia |

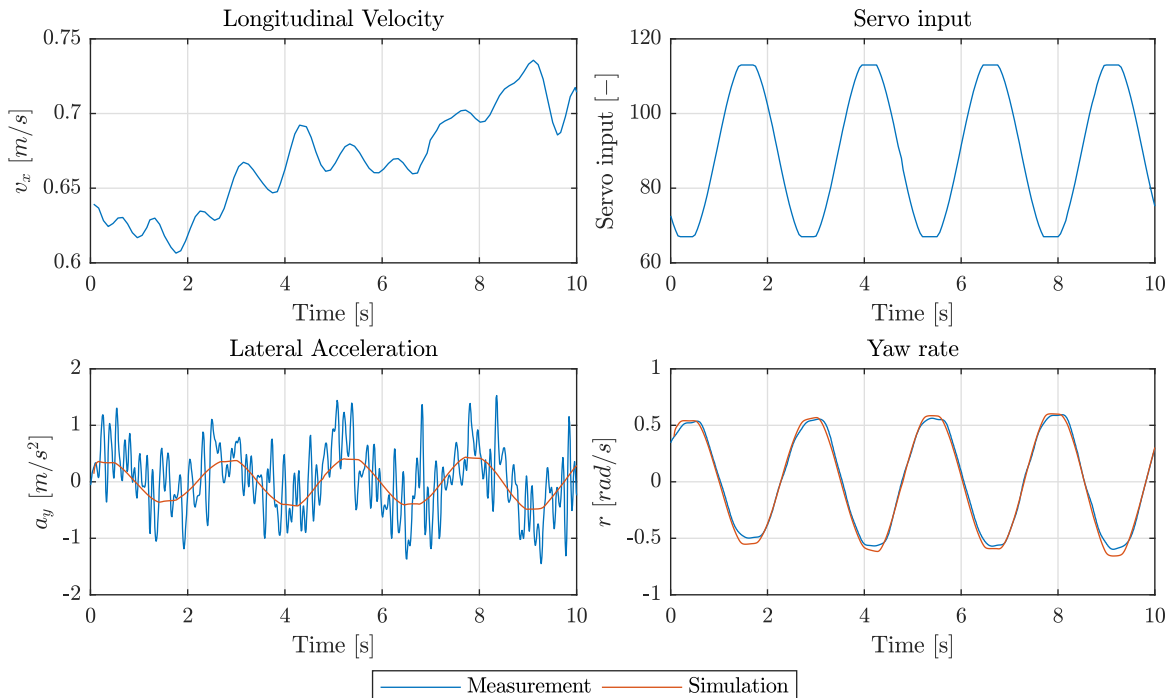


Figure 3-8: Estimated linear bicycle model versus measurement data. Driving at a fixed throttle input and a sine steering input.

3-4-2 Longitudinal tyre dynamics

Because of the smooth tyres and large motor power of the DSV, spinning wheels during driving is a common thing. Estimation of the longitudinal tyre parameters should, therefore, be performed with nonlinear tyre behaviour taken into account. Additionally, longitudinal dynamics and longitudinal load transfer need to be added to the linear bicycle model from the previous estimation steps. The resulting model equations are as stated in Equation 2-1, Equation 2-2 and Equation 2-3. Since lateral load transfer is not required for pure longitudinal manoeuvres, the left and right tyre forces are equal. The cornering stiffnesses found in the previous estimation step are used as parameters for the modified Dugoff tyre model, remaining the longitudinal tyre stiffness, maximum tyre-road friction coefficient and the longitudinal relaxation length as unknown parameters. The inputs of the vehicle model are the steering angle and rear wheel angular velocity. The outputs used for estimation are the yaw rate, longitudinal velocity and front wheel angular velocity. The following manoeuvres are used for estimation:

- Constant throttle input from a standstill
- Sine throttle input with different amplitudes and frequencies

All manoeuvres are performed with a fixed steering angle of zero degrees.

A nonlinear-least-squares optimisation is performed to estimate the parameters corresponding to the measured data. The resulting parameters are shown in Table 3-6. Figure 3-10 shows a comparison of the measurement data versus the simulation data for two of the manoeuvres. In subsection A-2-3 the comparisons of more manoeuvres can be found.

The results from the simulation are similar to the measurement. However, a small peak in longitudinal velocity during the decrease in rear wheel speed can be observed. This is a result of the curve shape of the tyre model, as shown in Figure 3-9; after reaching the peak tyre force, the force decreases for an increasing wheel slip. In the figures, this can be observed by the dip in longitudinal acceleration when the rear angular velocity peaks. The decreasing rear wheel slip after the peak, results in a momentarily increasing longitudinal force, before it decreases again, with a small increment in longitudinal acceleration as a result. Solving this small model mismatch requires altering the curve of the tyre model, which introduces four extra parameters (from Equation 2-13) to the estimation process. Since the mismatch is small and added complexity to the estimation process is large, the small mismatch is accepted.

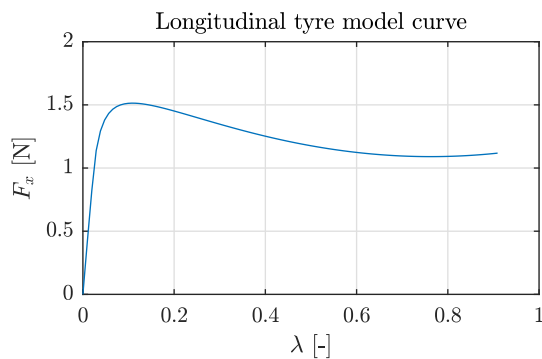
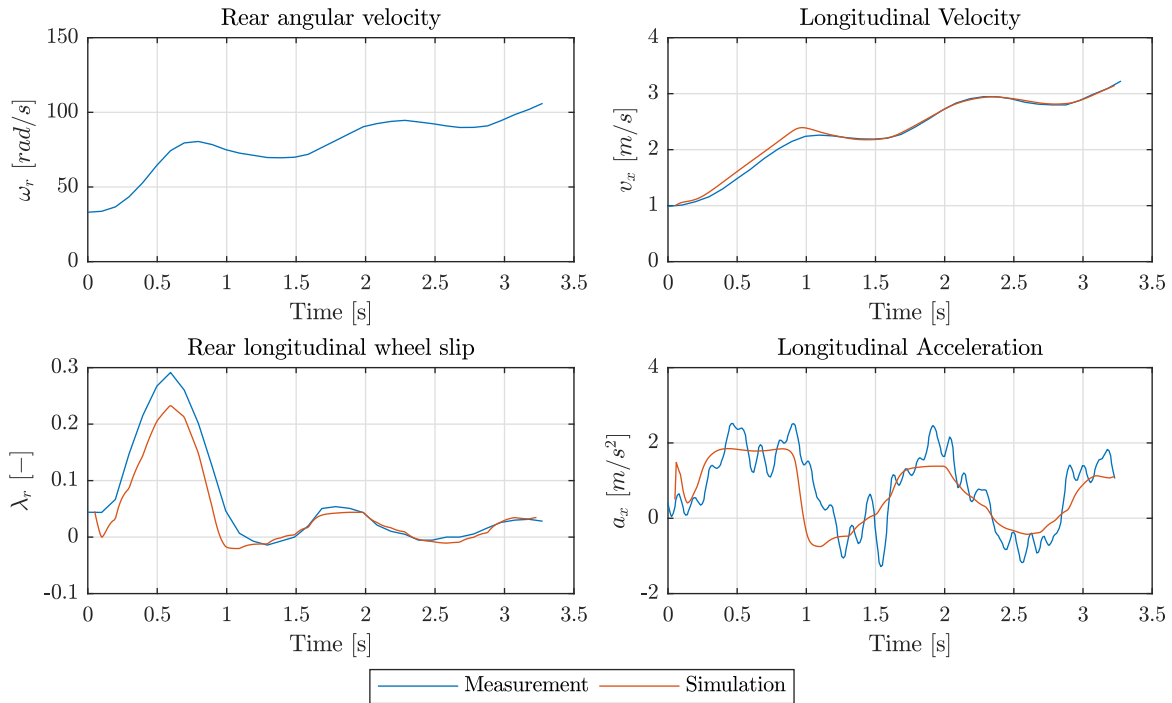


Figure 3-9: Longitudinal tyre force versus pure longitudinal wheel slip

Table 3-6: Parameter estimation results of the 5 degrees of freedom longitudinal dynamics

| Symbol | Value | Description |
|---------------------|-------------|--------------------------------|
| C_σ | 34.45 N/rad | Longitudinal tyre stiffness |
| μ_{max} | 0.35 | Tyre-road friction coefficient |
| $\sigma_{rl, long}$ | 0.04 m | Longitudinal relaxation length |

**Figure 3-10:** Estimated longitudinal dynamics versus measurement data. Sine throttle input.

3-4-3 Combined tyre dynamics

From the previous two parameter identification steps, all parameters for the Dugoff tyre model are estimated. However, the cornering stiffnesses are only estimated for linear tyre behaviour, and the parameters are not tested for combined slip behaviour. An extra estimation step is performed to find the tyre model parameters for combined nonlinear tyre behaviour. The rear angular velocity and steering angle are used as input. The longitudinal velocity, front wheel angular velocity, lateral acceleration and yaw rate are used as outputs. Multiple manoeuvres with varying motor and steering inputs are used, especially exciting the nonlinear tyre behaviour, but also gentle manoeuvres to make sure the parameters fit the linear behaviour.

The resulting parameters from the nonlinear-least-squares optimisation are stated in Table 3-7. Figure 3-12 and Figure 3-13 show a comparison between the measured and simulated data, for a manoeuvre with varying motor and steering inputs. Both figures show a large correspondence between the simulation and measurement. However, the yaw rate in Figure 3-13 shows an increasing deviation in yaw rate. This is a result of the shape of the lateral tyre

force curve, as shown in Figure 3-11. After the peak lateral tyre force, the force decreases for an increasing slip angle. The steepness of this curve is defined in the modification of the Dugoff tyre model, changing those would require extra parameters, which increases the complexity of the estimation process. Increasing the tyre-road friction, would increase the grip and would, therefore, reduce the difference in yaw rate and acceleration. However, it would also increase the peak lateral tyre force and consequently increase the difference in yaw error in the first figure. For that reason, a value which results in the lowest deviation for all the manoeuvres is used.

Table 3-7: Parameter estimation results 5 DOF combined slip behaviour

| Symbol | Value | Description |
|-------------------|-------------|------------------------------|
| $C_{\alpha,f}$ | 13.82 N/rad | Front lateral tyre stiffness |
| $C_{\alpha,r}$ | 25.21 N/rad | Rear lateral tyre stiffness |
| $\sigma_{rl,lat}$ | 0.0144 m | Lateral relaxation length |

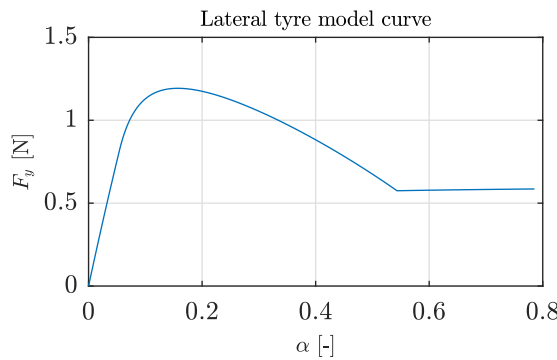


Figure 3-11: Lateral tyre force versus wheel slip angle for the front wheels

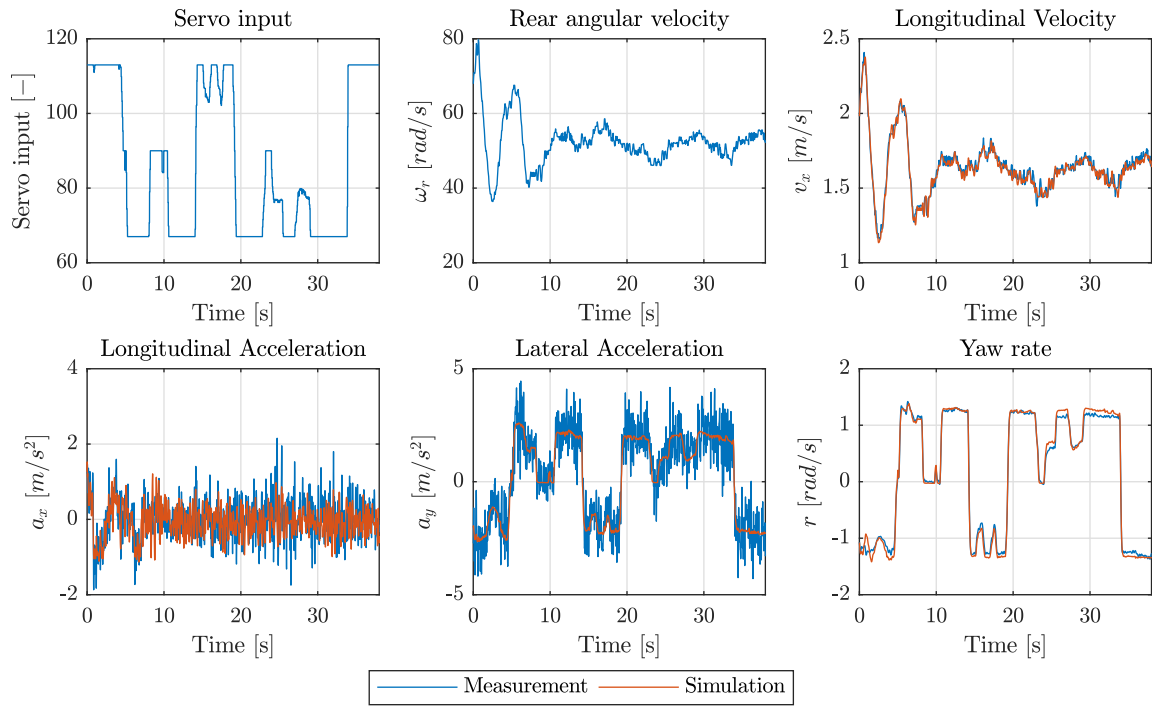


Figure 3-12: Estimated combined tyre dynamics versus measurement data. Varying motor and steering inputs.

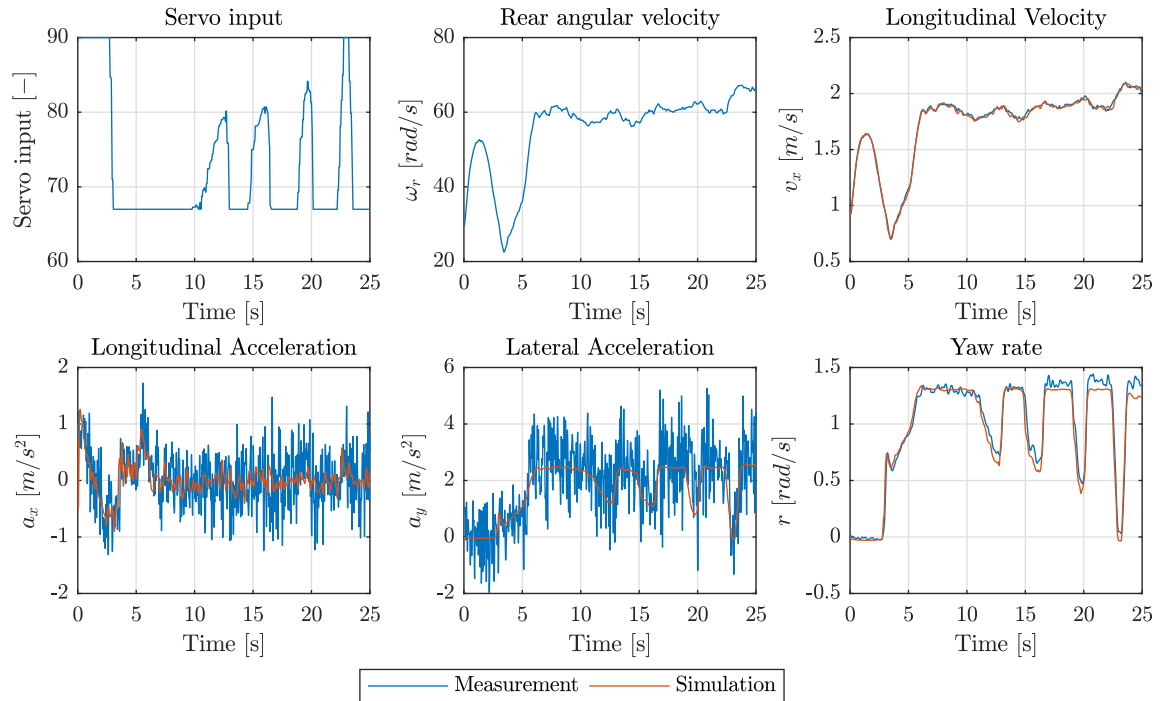


Figure 3-13: Estimated combined tyre dynamics versus measurement data. Varying motor and steering inputs.

3-5 Full vehicle model validation

The final step in the system identification is the validation of the estimated parameters for the full vehicle model since all parameters are estimated for simplified vehicle models. A seven degrees-of-freedom vehicle model, as defined in section 2-2, is created in Simulink Simscape Multibody, a Simulink toolbox that enables simulating a mechanical system by defining it as a 3D multibody model. This has the benefit that equations of motion are generated automatically, which reduces the chance of calculation errors. Additionally, by creating a vehicle model based on a 3D model, geometry of, for example, the steering system can be included as well.

The full vehicle model, with parameter values obtained in the previous estimation steps, is compared to multiple measurement datasets with varying motor and steering inputs. Direct input of the throttle input from the measurement data, however, results in a significant deviation in longitudinal velocity, because of a mismatch in the motor model. This makes it hard to validate the model. Therefore, a feedback controller is used to make sure the angular velocity of the rear wheels matches the measurement data. The schematic for this feedback loop is displayed in Figure 3-14.

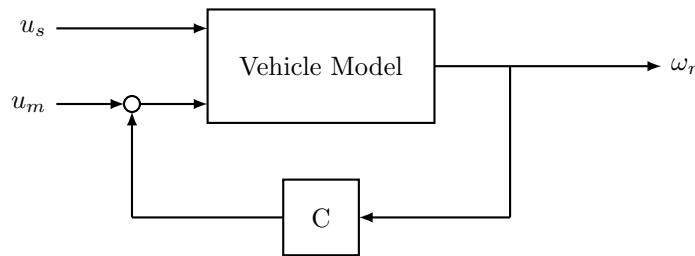


Figure 3-14: Closed-loop vehicle model schematic

The response of the full vehicle model, compared to measured data, is shown in Figure 3-15 and Figure 3-16. The manoeuvres performed in both dataset excite the vehicle's dynamics in various ways. The first manoeuvre shows large changes in lateral acceleration and yaw rate at a nearly constant velocity. The second manoeuvre shows the vehicle response for large variations in both lateral as longitudinal motion. For both manoeuvres, the simulation data shows a very comparable response. For that reason, no extra estimation steps with the full vehicle model are taken.

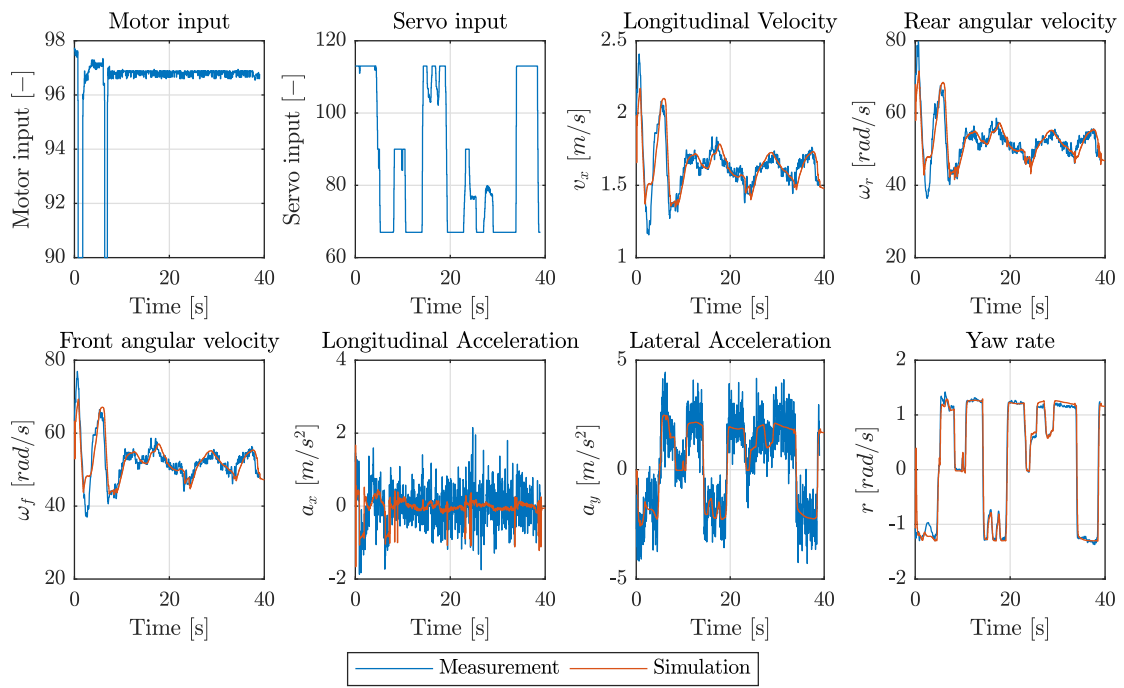


Figure 3-15: Manoeuvre for motor parameters estimation: Varying steering inputs for a near constant throttle input.

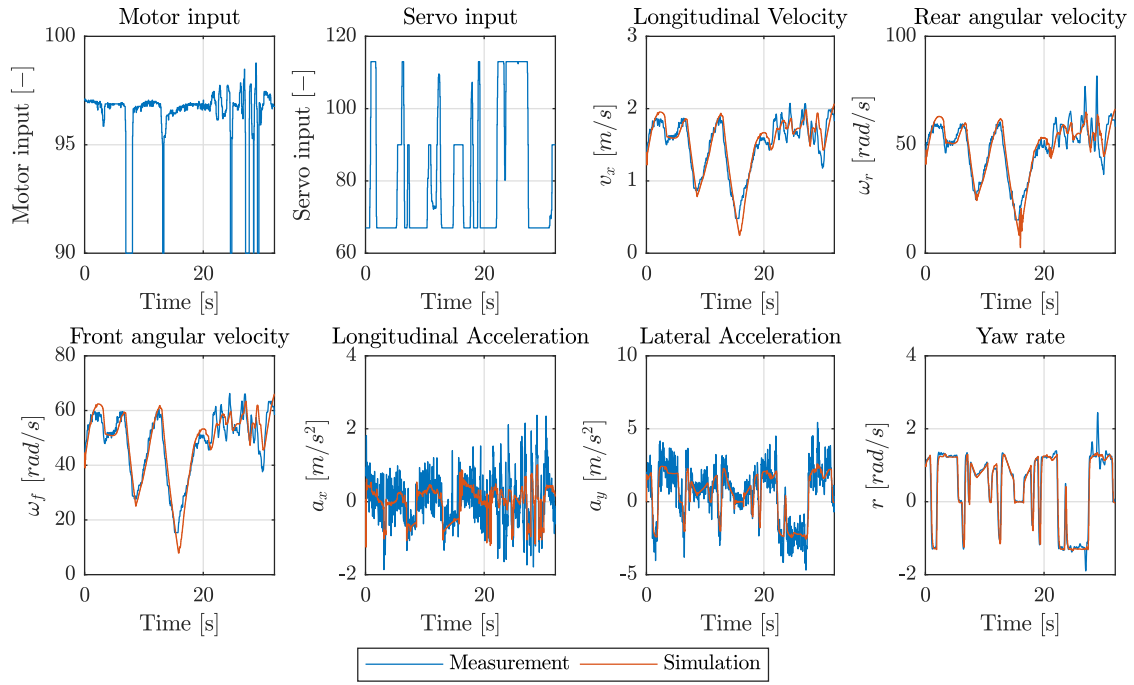


Figure 3-16: Manoeuvre for motor parameters estimation: Varying motor and steering inputs.

Chapter 4

Vehicle model analysis

Before the vehicle can be brought into a drift, the behaviour of the vehicle in various situations has to be analysed. In order to do this, first, the phase trajectories of the vehicle for a range of initial conditions are discussed. After that, the tyre characteristics are researched, and finally, an analysis of the vehicle model equilibria is performed.

Because the full vehicle model resulting from chapter 3 has a large number of degrees-of-freedom, calculation of the equilibria is very time-consuming. For that reason a five degrees of freedom (DOF) nonlinear bicycle model is used in this chapter. The equations of motion of this model are as stated in Equation 2-1, Equation 2-2 and Equation 2-3. The tyres are modelled by the modified Dugoff tyre model from subsection 2-2-3. Since, however, no load transfer is taken into account, the wheels at the front and rear axle are lumped together.

4-1 Phase trajectories

The phase portrait in Figure 4-1, shows the response of the vehicle model for various initial sideslip angles and yaw rates at a steering angle of zero degrees. In this response, one minimum and two saddle points can be found. The minimum (indicated by the \circ) is positioned at zero yaw rate and sideslip angle. It represents straight-ahead driving and is a stable equilibrium. The two saddle points, indicated by the \square and \triangle , are characterised by large sideslip angles and yaw rates. They are unstable drift equilibria, where the \square indicates a left-hand drift and the \triangle a right-hand drift.

In Figure 4-2a the phase trajectories for a steering angle of 6 degrees are shown. As result of the increased steering angle, the stable and left-hand drift equilibria have moved closer toward each other, whereas the right-hand drift equilibrium has moved towards a larger sideslip angle. A schematic of the orientation of a bicycle model in each of the equilibria is shown in Figure 4-3. For the right-hand drift equilibrium, a positive steering angle means it is counter-steering, i.e. the front wheels are steered in the opposite direction of the curvature in which the vehicle is moving. At the left-hand drift equilibrium, a positive steering angle means that it is steering along with the curve. The wheel slip angle of the front wheel is larger at the left-hand

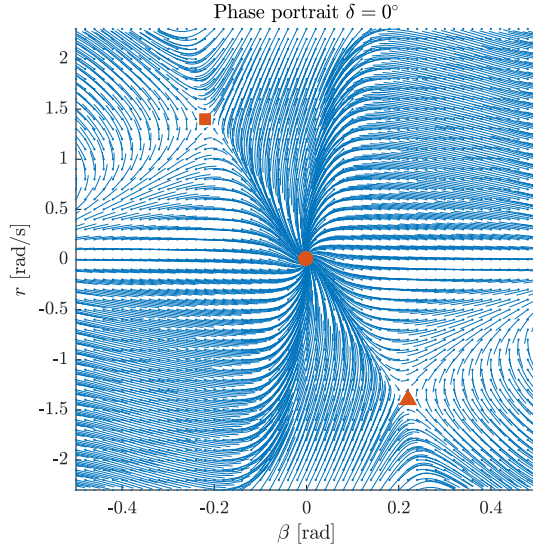


Figure 4-1: Phase portrait for initial velocity $v = 1.5 \text{ m/s}$ and steering angle $\delta = 0^\circ$. The marker stable (\circ) and unstable (\square, \triangle) drift equilibria

equilibrium than at the right-hand drift equilibrium. When the steering angle is increased further, the left-hand drift equilibrium will move closer towards the stable equilibrium; the body sideslip angle becomes smaller and the yaw rate decreases. This results in an increased front wheel slip angle and thus an increased front lateral tyre force. Increasing the wheel slip angle more will result in a decreasing front lateral force, up to the point that the lateral force is insufficient to generate the yaw moment around the vehicle to maintain the negative sideslip angle. In Figure 4-2b the phase portrait of a steering angle of 11 degrees is shown. This phase portrait only contains two equilibria, since the steering angle is too large for a left-hand drift equilibrium to exist.

Next to three equilibria found in the first phase portrait, Figure 4-2a also shows a whole range of equilibria around a yaw rate of 0.8 rad/s and a sideslip angle around -0.4 rad . In this range, however, front wheels slip angles have values of 0.4 rad and larger, which is far beyond the lateral tyre force peak. As a consequence, a large steering angle is required to change the magnitude of the lateral tyre force, which makes it difficult to control the vehicle around a drift equilibrium like these. Moreover, in chapter 3 it was noted that for wheel slip angles of this magnitude the accuracy of the tyre model decreases. Therefore, equilibria in this range are neglected.

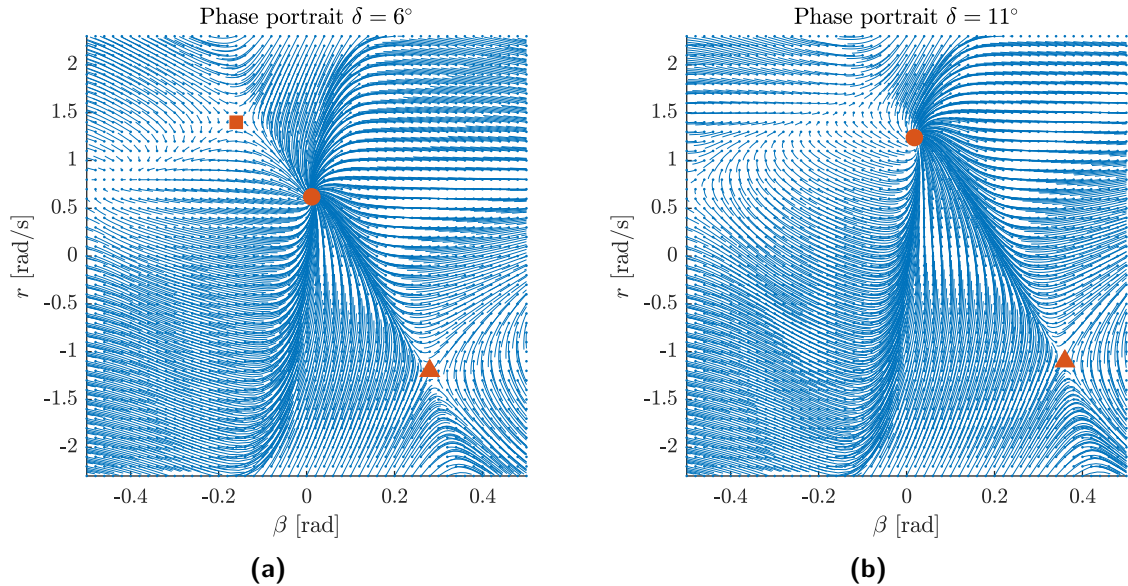


Figure 4-2: Phase portrait for initial velocity $v = 1.5$ m/s and steering angle $\delta = 6^\circ$ and $\delta = 11^\circ$.

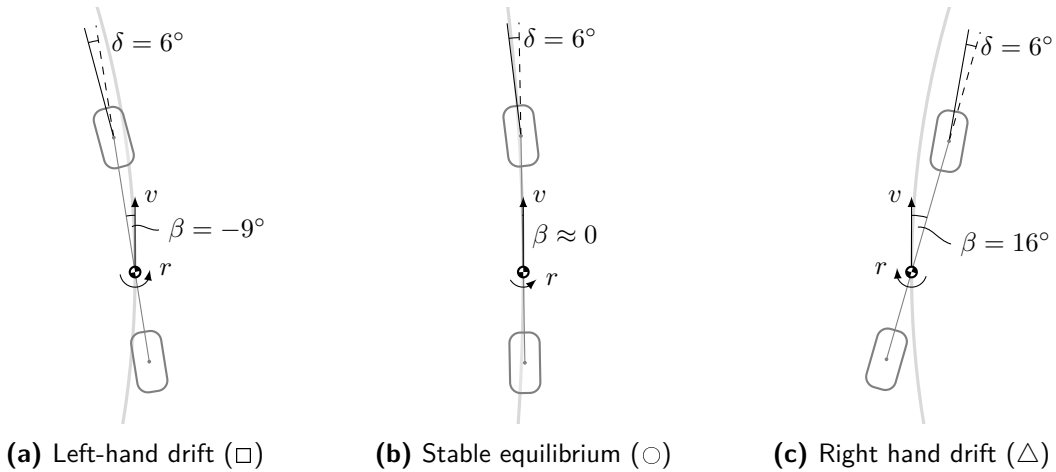


Figure 4-3: Representation of the three equilibria for a steering angle of $\delta = 6^\circ$ and a velocity of 1.5 m/s

The phase portraits are created with the assumption of a constant longitudinal velocity. Due to lateral wheel slip and friction in the system, however, a motor input is required to maintain a constant velocity. The addition of this longitudinal force affects the lateral force, the found equilibria, therefore, are not representative for actual drift conditions. To get a better understanding of drift equilibria, first, the relationship between longitudinal and lateral tyre forces needs to be researched.

4-2 Combined tyre slip

In section 1-1 the effects of combined wheel slip are introduced. To get a better understanding of the tyre behaviour of the Delft Scaled Vehicle (DSV), the effects of combined slip in the vehicle model are investigated. In Figure 4-4 the influence of the wheel slip angle on the longitudinal force and longitudinal wheel slip on the lateral force are shown. A significant influence of both slip values on both forces can be observed. Figure 4-4b shows a significant decrease in lateral force for an increase in longitudinal slip, especially in the lower range of wheel slip angles. Additionally, the peak of the lateral force moves to a larger wheel slip angle. The latter is convenient for drifting since, beyond the lateral tyre force peak, control of the yaw motion of the vehicle becomes more difficult. The reason for this is that, beyond the peak, the lateral force decreases for an increase in wheel slip angle. A decrease in lateral force results in a decrease in compensation for the yaw moment induced by the front lateral force, resulting in an increasing yaw moment and over time an increasing rear wheel slip angle. Without quick action, a spinning vehicle will be inevitable.

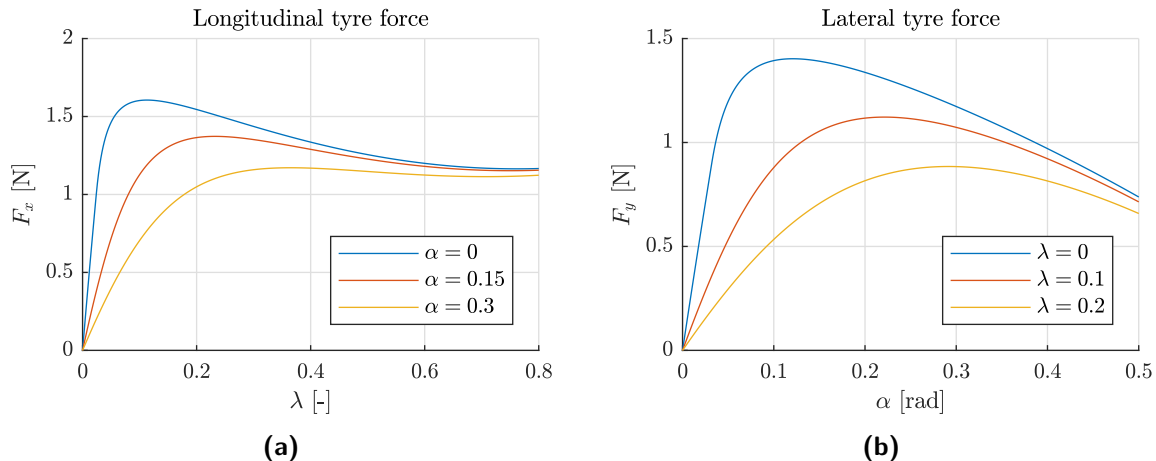


Figure 4-4: Influence of a wheel slip angle on the longitudinal tyre force and influence of longitudinal wheel slip on the lateral tyre force.

In Figure 4-5, the friction ellipse of the rear wheels is shown. The friction ellipse is a useful tool to understand the behaviour of a saturated tyre, since, although it is not a perfect ellipse, it seems much more straightforward than for a non-saturated tyre. The ellipse shows, for example, that during typical cornering, the rear tyre can be saturated by increasing the longitudinal wheel slip to 0.16. After that, the wheel slip required for a certain maximum lateral force can simply be found by following the ellipse.

In summary, a torque input on the rear wheels has a large influence on the lateral tyre forces. Realistic drift equilibria can, therefore, only be found when taking rear longitudinal wheel slip into account.

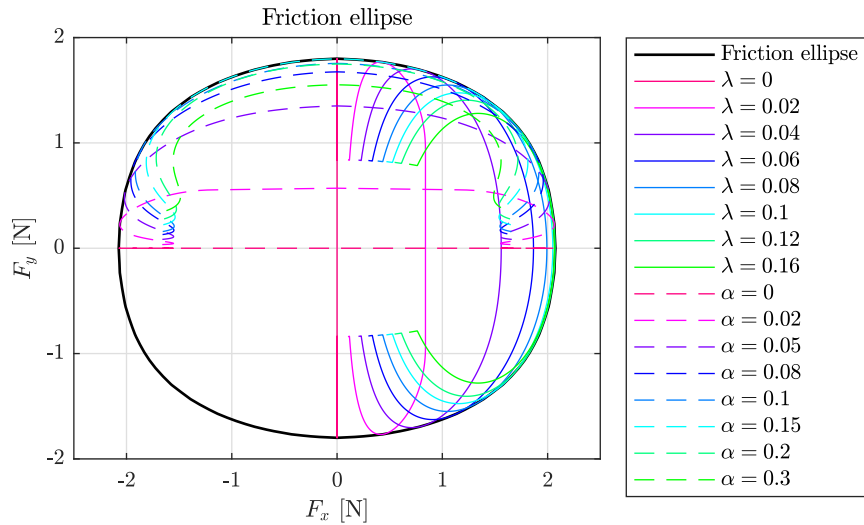
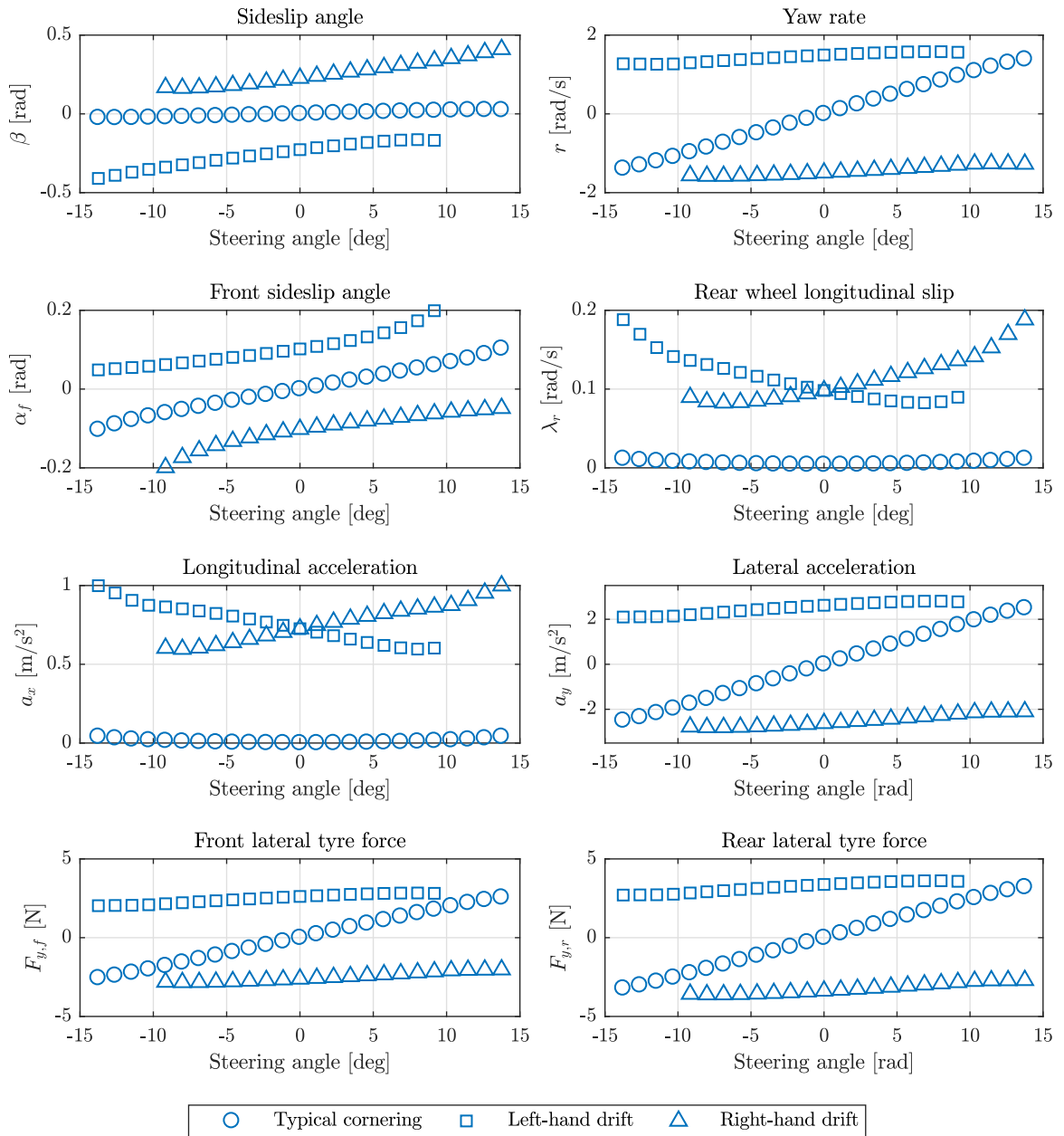


Figure 4-5: Friction ellipse of the rear wheel at a load of 6.2 N

4-3 Drift equilibria

The equilibria of the vehicle model are found by performing a steady-state operation point search with MATLAB. The found equilibria are shown in Figure 4-6. The influence of the longitudinal wheel slip directly stands out, the wheel slips of all drift equilibria are much higher than for the typical cornering conditions, showing that the rear wheels in these equilibria are saturated. Furthermore, to balance the yaw equation of moment, a linear relationship between the magnitude of the front and rear lateral tyre forces can be observed in the bottom two plots of Figure 4-6. This relationship holds, up to saturation of the front tyres at a steering angle of 10 degrees for the left-hand drift equilibrium. Next, for a constant absolute velocity, a large range in equilibrium yaw rates is found. This means the trajectory can have a varying curvature, without having to change the velocity. This is convenient, since, due to the relationship between the longitudinal and lateral tyre force, the velocity is difficult to directly control during drifting. Moreover, the largest equilibrium yaw rate corresponds to a drift equilibrium. In Figure 4-7 the trajectory for both the stable and left-hand drift equilibrium with the highest yaw rate are visualised. The drifting vehicle is able to drive a sharper curvature compared to the non-drifting vehicle. At higher velocities, this difference decreases, but a larger yaw rate remains achievable by drifting.

**Figure 4-6:** Equilibrium analysis for $v = 1.8$ m/s

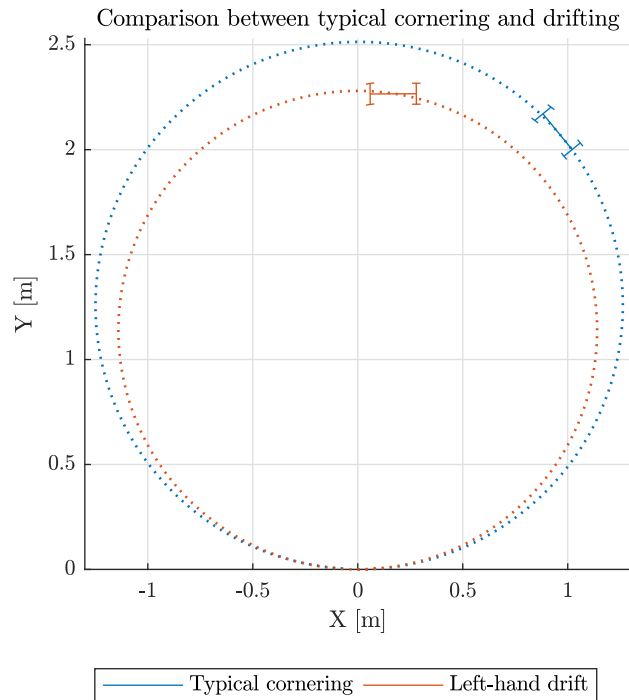


Figure 4-7: Comparison between maximum curvature for typical cornering and drifting, at a velocity of 1.8 m/s.

The phase trajectories of the vehicle model have shown the existence of drift equilibria. After analysis of the tyre model, a simple relationship between the longitudinal and lateral tyre forces of a saturated tyre was found. With the effects of this relationship taken into account, a more thorough equilibrium analysis is performed. The found equilibria show that drifting with the DSV should be possible and can be achieved in large part of the steering range. With this knowledge, the next step is to develop a controller to bring the vehicle to an equilibrium point and keep it there.

Chapter 5

Vehicle Control

In the previous chapter, it is shown that various drift equilibria for the Delft Scaled Vehicle (DSV) exist. Controlling the vehicle around these equilibria, while following the desired path, is the next step. This chapter will first elaborate on path tracking and its error definitions. Subsequently, a control approach for drifting is discussed and, finally, expanded with path tracking capabilities.

5-1 Error definition

Path-following is an intensively studied topic, with one of the first systems originating from the early 1950's. The first systems used sensors in the vehicle's front bumper, to detect an inductive cable in the road surface[23]. Various look-down approaches like these have existed, experiments showed instability above velocities of 20 m/s [24]. By placing the sensors a meter in front of the vehicle, path tracking at higher velocities became possible. Although these systems were rather impractical, currently used systems, like computer vision, are based on the same look-ahead principle. The use of an even larger look-ahead distance provides closed-loop stability and damping, which makes it usable at higher speeds[25].

In Figure 5-1 various error-definitions that are used in path tracking are visualised. Just like the above mentioned look-ahead system, a camera can detect the lateral look-ahead error, y_{la} . This is the distance between the vehicle centreline and a point on the path at distance x_{la} in front of the vehicle. Since this error is only based on the path in front of the vehicle, however, lateral control based on this error will result in corner cutting[26]. But, with knowledge of the road geometry, the look-ahead error e_{la} can be defined. This error is the distance between the same look-ahead point and the tangent of the path at a point sideways of the centre of gravity[27, 24]. This look-ahead error can also be calculated by

$$e_{la} = y_e + x_{la} \sin(\psi_e), \quad (5-1)$$

where y_e is the lateral distance from the Centre of Gravity (COG) to the path and ψ_e , the heading error, is the angle between the centreline of the vehicle and the path tangent[24]. This definition makes it easier to use other sensors next to, or instead of, a camera.

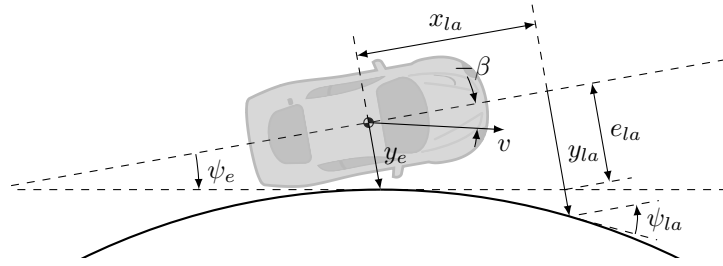


Figure 5-1: Various look-ahead error definitions

At high body sideslip manoeuvres, the look-ahead definition from Equation 5-1 causes two problems; the first one is shown in figure Figure 5-2a. The look-ahead error is based on the vehicle orientation, thus, for a non-zero body sideslip angle, a cornering condition exists where the look-ahead error is zero for a non-zero heading and lateral error. Using the vehicle course instead of orientation, by adding the sideslip angle to the error definition, solves this problem. Direct input of the sideslip angle, however, results in reduced stability margins and yaw oscillations at high lateral accelerations[28]. By using a predicted steady-state body sideslip angle, β_{ss} , stability remains for a slightly lower performance[28].

The second problem with the above-mentioned error definition is the measurement of the lateral error. At larger body sideslip angles, this error is not representative for the real distance to the path and, furthermore, a path tangent at a previous point on the path will be taken, as shown in figure Figure 5-2b. To solve this problem, the shortest distance between the COG and the path, e_y , is used, instead of the distance to the path in the lateral direction of the vehicle. The resulting look-ahead error definition, as used in this research, is given by

$$e_{la} = e_y + x_{la} \sin(\psi_e + \beta_{ss}) \quad (5-2)$$

and visualised in Figure 5-3.

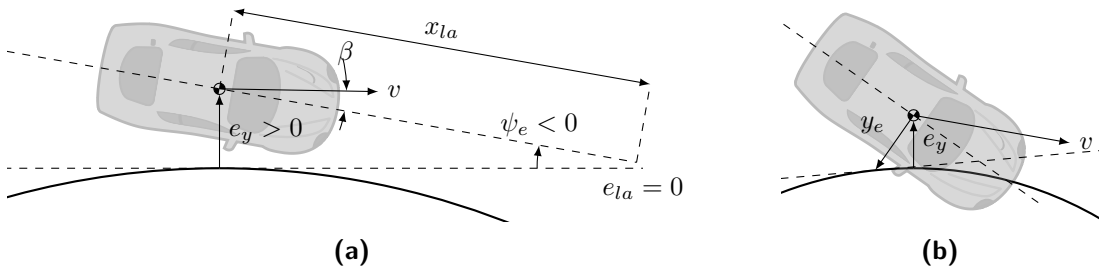


Figure 5-2: Two problems arising when using the look-ahead error definition from Equation 5-1 at large body sideslip angles.

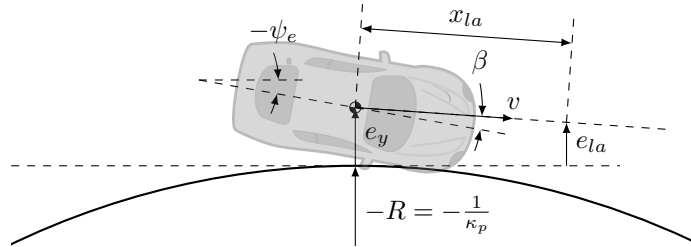


Figure 5-3: Path-tracking error definition as used in this research

5-2 Controller structure

The response of the vehicle to steering and throttle inputs differs in typical cornering conditions and for large body sideslip manoeuvres[10]. For that reason, a separate controller for both conditions is used. A schematic of the controller structure is shown in Figure 5-4.

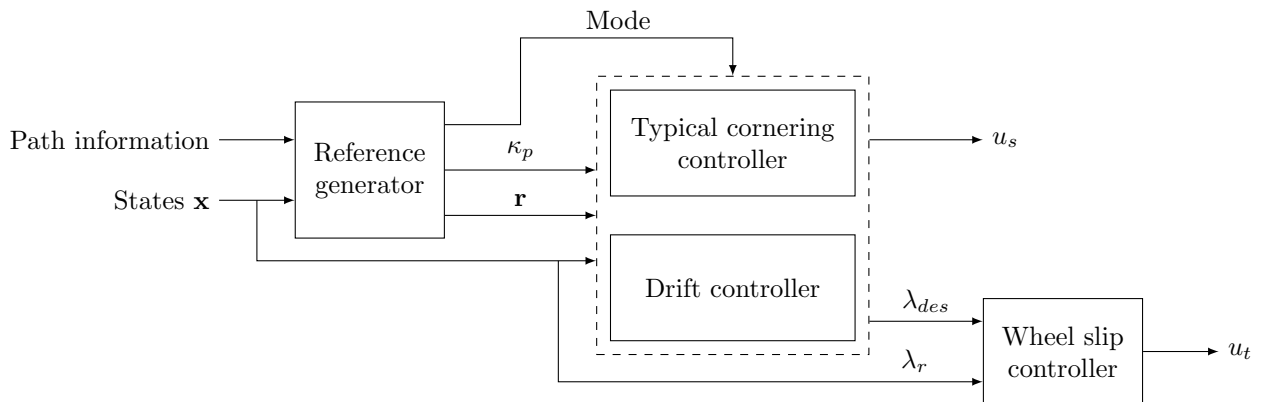


Figure 5-4: Controller structure

The reference generator uses path information (curvature and path-tracking errors) from the positioning system and the vehicle states, \mathbf{x} , to select a controller and define the state references, \mathbf{r} . Selection of the controller is based on the equilibria found in section 4-3. From the path curvature, κ_p , and desired absolute velocity, v_{des} , a desired vehicle yaw rate can be obtained by

$$r_{des} = \kappa_p v_{des} \quad (5-3)$$

By matching this yaw rate to the equilibrium yaw rates, the desired driving condition (typical cornering or drifting) and equilibrium states are obtained. The equilibrium states are used in the drift controller; the yaw rate and sideslip angle as a reference and the longitudinal wheel slip as feedforward.

As control inputs, the DSV receives a servo input, u_s and throttle input, u_t . A desired steering angle can be transformed to a servo input via inversion of Equation 3-6. The relationship between throttle input and drive torque, however, depends on a lot of factors, as discussed in subsection 3-2-2. A low-level longitudinal wheel slip controller is implemented, to coop with

the complex and variable motor dynamics. Both the typical cornering and drift controller will provide a desired wheel slip, λ_{des} . The wheel slip controller will then minimise the error $e_{\lambda_r} = \lambda_{des} - \lambda_r$ via the throttle input. The controller equation of the wheel slip controller is given by

$$u_m = K_\lambda e_\lambda + K_{\lambda,i} \int_0^t e_r(t) dt \quad (5-4)$$

where K_λ and $K_{\lambda,i}$ are the proportional and integral controller gain, respectively.

5-3 Typical cornering

In typical cornering conditions the steering angle and throttle input both have control authority over different driving tasks. The steering input is used for lateral control and the throttle input for longitudinal control. Path tracking can, therefore, be achieved by controlling the steering angle only. The throttle input is used to maintain the desired velocity.

5-3-1 Lateral control

The objective of a path-following controller is to minimise the look-ahead error. With a pure feedback controller, this goal can be achieved. However, a feedback controller only acts after an error is detected. A feedforward controller, on the other hand, uses vehicle states, the curvature of the path and an inverse vehicle model to estimate the required steering angle to keep all errors at zero. The feedback controller will then cover errors resulting from model mismatches.

The steering command is given by

$$\delta = \delta_{FF} + \delta_{FB}, \quad (5-5)$$

where the subscripts *FF* and *FB* denote feedforward and feedback respectively. The feedforward steering angle is obtained with

$$\delta_{FF} = \left(\ell + \frac{K_{us} v_x^2}{g} \right) \kappa, \quad (5-6)$$

where $K_{us} = \frac{F_{zf}}{C_{\alpha,f}} - \frac{F_{zr}}{C_{\alpha,r}}$ is the understeer gradient. This is a widely used steering feedforward, based on vehicle kinematics and steady-state cornering[29, 9]. The feedback controller is based on the same equation, but with a feedback curvature based on the look-ahead error. The look-ahead error can be seen as Sagitta of a circle with radius $\frac{1}{\kappa_{FB}}$, as shown in Figure 5-5 [29]. The feedback curvature can then be found by

$$\kappa_{FB} = -\frac{2e_{la}}{e_{la}^2 + (x_{la} + b)^2} \approx -\frac{2e_{la}}{(x_{la} + b)^2}, \quad (5-7)$$

where the look-ahead distance in the denominator can be neglected since it is small compared to the radius of the circle. Note that the denominator of the fraction consists of the look-ahead distance plus the distance from the rear axle to the centre of gravity, b . This is because in typical cornering conditions it can be assumed that the driven curvature of the vehicle starts

at the rear wheels, by neglecting the rear wheel slip[29]. The resulting feedback steering angle is defined by

$$\delta_{FB} = \left(\ell + \frac{K_{us} v_x^2}{g} \right) \kappa_{FB} = - \left(\ell + \frac{K_{us} v_x^2}{g} \right) \frac{2(e_y + x_{la} \sin(\psi_e + \beta_{ss}))}{(x_{la} + b)^2}. \quad (5-8)$$

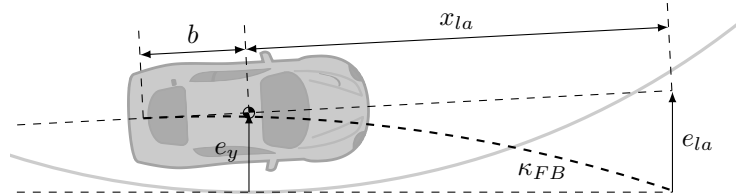


Figure 5-5: The feedback-curvature based on the look-ahead error

A human driver will look further ahead if driving at a higher velocity. For that reason, the look-ahead distance is also made dependent on velocity

$$x_{la} = vt_{la}, \quad (5-9)$$

where t_{la} is the look-ahead time. The steady-state body sideslip angle is given by

$$\beta_{SS} = \left(\frac{mav_x^2}{\ell C_{\alpha,r}} - b \right) \kappa_p, \quad (5-10)$$

where m is the vehicle mass, a is the distance from the centre of gravity to the front wheels, $C_{\alpha,r}$ is the rear tyre cornering stiffness and ℓ is the wheelbase.

5-3-2 Longitudinal control

During typical cornering, the motor input of the vehicle is controlled by feedback on the longitudinal velocity. The used error is defined by

$$e_{v_x} = v_x^{des} - v_x. \quad (5-11)$$

The desired rear longitudinal wheel slip is then obtained with a PI controller, given by

$$\lambda_{des}(t) = K_v e_{v_x}(t) + K_{v,i} \int_0^t e_{v_x}(t) dt. \quad (5-12)$$

5-4 Drift controller

During high body sideslip manoeuvres, the vehicles lateral and yaw motion are controlled by both the steering and motor input. Hindiyeh showed that it is possible to maintain a drift by controlling either of the control inputs and keeping the other at its equilibrium state[10].

When in danger of exiting the drift, however, pure steering control can not generate the required yaw moment to maintain the drift. With pure throttle control, a drift can be maintained when both in danger of spinning or exiting the drift. This controller, though, sacrifices minimisation of the longitudinal velocity error. A combination of both controllers is proposed, based on the equations of motion of the bicycle model.

5-4-1 Controller definition

In Equation 5-13 the lateral equations of motion of the bicycle model are shown. Both the yaw and sideslip dynamics have a dependency on the front and rear lateral tyre forces.

$$\dot{\beta} = \frac{F_{y,f} + F_{y,r}}{mv_x} - r \quad (5-13a)$$

$$\dot{r} = \frac{aF_{y,f} - bF_{y,r}}{I_z} \quad (5-13b)$$

The magnitude and sign of a lateral tyre force, depend on the wheel slip angle. With the steering angle, the wheel slip angle of the front wheels can directly be controlled. Providing the ability to change both the magnitude and the sign of the lateral tyre forces. The wheel slip angle of the rear wheels depends on the motion of the vehicle. With the throttle input, only the longitudinal wheel slip can be controlled and, therefore, via the tyre dynamics, the magnitude of the lateral tyre force. The direction of the force, though, can only be adjusted by changing the sign of the wheel slip angle. Inspection of the yaw and sideslip dynamics in Equation 5-13 shows that the sideslip dynamics contains a sum of the lateral forces and the yaw dynamics a weighted difference of the lateral forces. The fact that a control input does not easily change the direction of the rear lateral tyre force, makes it difficult to change the sign of the rate of body sideslip angle. The sideslip dynamics, however, also depend on yaw rate. Since the sign of the yaw dynamics is changed more easily, the sideslip angle can be controlled via the yaw dynamics.

Analysis of the equilibria shows another characteristic in favour of controlling the sideslip dynamics via the yaw dynamics. As can be observed in Figure 4-6, a higher equilibrium yaw rate corresponds to a smaller (less negative) equilibrium body sideslip angle. To get to this equilibrium sideslip angle, however, the yaw rate first has to decrease. This results from the negative yaw rate term in the sideslip dynamics in Equation 5-13b. Hindiyeh proposes a nested loop structure[10], to control the body sideslip angle via the yaw rate. The outer loop of the controller is defined by

$$r_{des} = r^{eq} + K_\beta e_\beta, \quad (5-14)$$

where r^{eq} is the yaw rate of a certain drift equilibrium, K_β is the sideslip error feedback gain and e_β is the sideslip error:

$$e_\beta = \beta - \beta^{eq}. \quad (5-15)$$

The inner loop is found by feedback linearization of the yaw rate error

$$\dot{e}_r = \dot{r} - \dot{r}_{des} = -K_r e_r \quad (5-16)$$

Substituting this with the lateral equations of motion from Equation 5-13 and the outer loop equations results in

$$\dot{e}_r = \dot{r} - K_\beta \dot{\beta} = \frac{aF_{y,f} - bF_{y,r}}{I_z} - K_\beta \left(\frac{F_{y,f} + F_{y,r}}{mv_x} - r \right) = -K_r e_r. \quad (5-17)$$

Collection of the lateral tyre forces results in

$$\left(\frac{a}{I_z} - \frac{K_\beta}{mv_x} \right) F_{y,f} - \left(\frac{b}{I_z} + \frac{K_\beta}{mv_x} \right) F_{y,r} = -(K_\beta + K_r)r + K_r r^{eq} + K_\beta K_r(\beta - \beta^{eq}). \quad (5-18)$$

This equation represents the required combination of the front and rear lateral tyre forces to minimise the yaw rate and sideslip error and maintain in the drift equilibrium. To add path tracking capabilities, some adjustments are made to the above controller equation.

The desired yaw rate in Equation 5-14 is based on a constant equilibrium yaw rate and the sideslip error. To include for path-tracking capabilities, the equilibrium yaw rate, r^{eq} , is exchanged by a yaw rate based on path curvature and path-tracking errors, $r_{des,pt}$. In subsection 5-3-1 the path-tracking errors are converted to a feedback curvature, which, together with the path curvature, forms the desired curvature. This curvature is used to find the desired steering angle, but can also be used to find the desired yaw rate for the drift controller, by multiplication with the desired velocity:

$$r_{des,pt} = \kappa_{des} v_{des}, \quad (5-19)$$

The definition of the desired curvature for this application, however, is slightly different to the one used in subsection 5-3-1. The first adjustment is the definition of the feedback curvature, which is given by

$$\kappa_{FB} = -\frac{2e_{la}}{e_{la}^2 + x_{la}^2} \approx -\frac{2e_{la}}{x_{la}^2}. \quad (5-20)$$

In this definition, the curvature does not start at the rear axle, but at the centre of gravity of the vehicle. In typical cornering conditions, the feedback curvature is based on the assumption that no wheel slip is present. Via the Ackerman geometry, it can then be assumed that the rear wheels always follow the curvature, since they do not move sideways[29]. During high sideslip manoeuvres, the rear wheels do move sideways and, therefore, it cannot be assumed that the rear wheels follow the driven curvature. For this reason the curvature crosses the vehicle at the centre of gravity in the direction of motion of the vehicle, as shown in Figure 5-6.

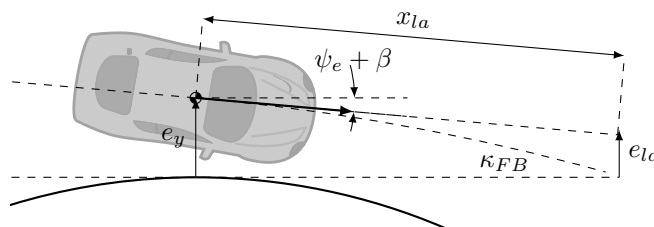


Figure 5-6: The feedback-curvature based on the look-ahead error

While tuning the final drift controller in chapter 6, it is observed that the required look-ahead distance is much larger than in typical cornering conditions (a look-ahead time of around 1.5 seconds instead of 0.5 seconds). At a look-ahead distance of this magnitude, the usage of the desired curvature as used for typical cornering conditions turns out to be problematic. If the corner radius is small compared to the look-ahead distance, this curvature definition will cross the path before the look-ahead distance. In Figure 5-7 a comparison of different

curvatures starting at the centre of gravity is shown. As can be observed, driving at the same curvature as the path (curve 1), results in a decreasing lateral error. If then feedback is added (curve 2), the resulting curve will cross the path before the look-ahead distance. An adjustment to the desired curvature definition is, therefore, made. Instead of the path curvature, the feedback curvature is added to the curvature of the circle in which the vehicle is driving. In other words, the radius of this curve is defined by the radius of the path curvature minus the lateral error. This results in curve 3 in the figure. The definition of the modified desired curvature is given by

$$\begin{aligned}\kappa_{des} &= (\kappa_p^{-1} - e_y)^{-1} + \kappa_{FB}, \\ &= (\kappa_p^{-1} - e_y)^{-1} - \frac{2e_{la}}{x_{la}^2},\end{aligned}\quad (5-21)$$

By subtracting the lateral error from the path radius, the lateral error will remain the same along the curve, if no feedback is applied. This is in accordance with the look-ahead error, which is equal to the lateral error if the heading error is equal to zero. Using this desired feedback will eventually result in fewer oscillations around the path and faster convergence to the path. In Appendix B a comparison between both curvature definitions for various lateral and heading errors is shown.

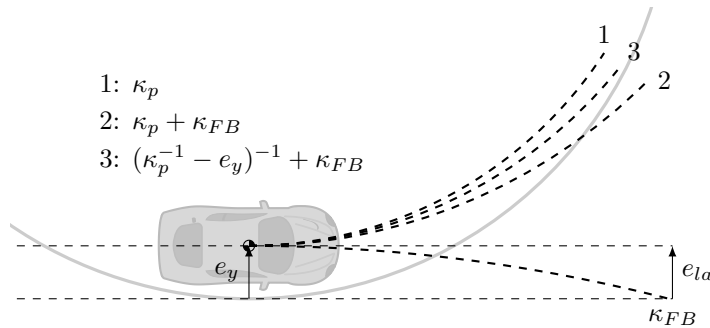


Figure 5-7: Comparison between two definitions of the desired curvature, with (1) the path curvature, (2) the desired curvature, as used in the typical cornering conditions, and (3) the desired curvature used in drift conditions

Replacing the equilibrium yaw rate in Equation 5-14 with the desired yaw rate for path tracking results in

$$\begin{aligned}r_{des} &= \kappa_{des} v_{des} + K_\beta e_\beta, \\ &= \left(\frac{1}{\kappa_p^{-1} - e_y} - \frac{2e_{la}}{x_{la}^2} \right) v_{des} + K_\beta (\beta - \beta^{eq}).\end{aligned}\quad (5-22)$$

In the original controller, the equilibrium sideslip angle follows from the selection of an equilibrium point. From Figure 4-6 it can be observed that the relationship between the equilibrium yaw rate and equilibrium sideslip angle is approximately linear. By fitting a curve to the data points, the equilibrium body sideslip angle can be defined as a function of the yaw rate. The relationship between the equilibrium body sideslip angle and the equilibrium yaw rate is defined by

$$\beta^{eq} = f_{\beta^{eq}}(r^{eq}).\quad (5-23)$$

With path-tracking added to the controller, an equilibrium sideslip angle that corresponds to the path curvature should be chosen. The equilibrium yaw rate in the equation is exchanged with the desired yaw rate for path-tracking. Using this yaw rate to select the reference body sideslip angle, however, will result in undesired behaviour. As explained earlier in this section, corresponds a higher equilibrium yaw rate to a smaller (less negative) equilibrium sideslip angle, but is a lower equilibrium yaw rate required to bring the sideslip angle to the lower value and the other way around. Using the desired yaw rate for path-tracking to select a reference body sideslip angle, will via the outer loop of the controller influence the reference yaw rate for the inner loop. This influence, however, is opposite to the direct influence of the path-tracking errors on the yaw rate. Since this indirect influence is undesired, the reference body sideslip angle is selected only from the curvature of the path:

$$\beta_{des} = f_{\beta^{eq}}(\kappa_p v_{des}). \quad (5-24)$$

With the new yaw rate and body sideslip reference, a new controller equation can be derived. The derivatives of the path-tracking errors are given by

$$\dot{e}_y = v \sin(\psi_e + \beta), \quad (5-25)$$

$$\dot{\psi}_e = r - \kappa_p \dot{s} = r - \kappa_p v \cos(\psi_e + \beta), \quad (5-26)$$

where \dot{s} is the velocity along the tangent of the path. Subsequently, the derivative of the look-ahead error can be defined as

$$\begin{aligned} \dot{e}_{la} &= v \sin(\psi_e + \beta) + x_{la} \cos(\psi_e + \beta)(\dot{\psi}_e + \dot{\beta}), \\ &= v \sin(\psi_e + \beta) + x_{la} \cos(\psi_e + \beta)(r - \kappa_p v \cos(\psi_e + \beta) + \dot{\beta}), \\ &= v \sin(\psi_e + \beta) + x_{la} \kappa_p v \cos^2(\psi_e + \beta) + x_{la} \cos(\psi_e + \beta) \left(\frac{F_{y,f} + F_{y,r}}{mv_x} \right). \end{aligned} \quad (5-27)$$

The derivative of the desired curvature is given by

$$\begin{aligned} \dot{\kappa}_{des} &= \frac{\frac{\dot{\kappa}_p}{\kappa_p^2} + \dot{e}_y}{(\kappa_p^{-1} - e_y)^2} - \frac{2\dot{e}_{la}}{x_{la}^2}, \\ &= \frac{\dot{\kappa}_p + v \sin(\psi_e + \beta) \kappa_p^2}{(1 - e_y \kappa_p)^2} - \frac{2}{x_{la}^2} \dot{e}_{la}. \end{aligned} \quad (5-28)$$

The derivative of the desired body sideslip angle is given by

$$\dot{\beta}_{des} = f'_{\beta^{eq}}(\kappa_p v_{des}) \dot{\kappa}_p v_{des}. \quad (5-29)$$

Note that the desired velocity is constant and therefore its derivative, \dot{v}_{des} , is equal to zero. Substituting the above in Equation 5-16 results in

$$\dot{e}_r = \dot{r} - \dot{r}_{des} = \dot{r} - \dot{\kappa}_{des} v_{des} - K_\beta (\dot{\beta} - \dot{\beta}_{des}) = -K_r(r - r_{des}) \quad (5-30)$$

Substitution of the derivatives and collection of the terms results in

$$\frac{aF_{y,f} - bF_{y,r}}{I_z} - K_\beta \left(\frac{F_{y,f} + F_{y,r}}{mv_x} \right) = \dot{\kappa}_{des} v_{des} - (K_\beta + K_r)r - K_r r_{des} - K_\beta \dot{\beta}_{des} \quad (5-31)$$

$$\begin{aligned} \frac{aF_{y,f} - bF_{y,r}}{I_z} - \left(K_\beta - \frac{2v_{des}}{x_{la}} \cos(\psi_e + \beta) \right) \left(\frac{F_{y,f} + F_{y,r}}{mv_x} \right) = \\ \left(\frac{\kappa_p^2 v}{(1 - e_y \kappa_p)^2} - \frac{2v}{x_{la}^2} + K_r \frac{2}{x_{la}} \right) v_{des} \sin(\psi_e + \beta) - K_r \left(\frac{\kappa_p}{1 - e_y \kappa_p} - \frac{2e_y}{x_{la}^2} \right) v_{des} \\ - (K_\beta + K_r)r - \frac{2\kappa_p v \cos^2(\psi_e + \beta)}{x_{la}^2} v_{des} + \left(\frac{1}{(1 - e_y \kappa_p)^2} - K_\beta f'_{\beta^{eq}} \right) \dot{\kappa}_p v_{des} \quad (5-32) \end{aligned}$$

Collecting the lateral tyre forces results in

$$\begin{aligned} K_{F_{y,f}} F_{y,f} - K_{F_{y,r}} F_{y,r} = \\ \left(\frac{\kappa_p^2 v}{(1 - e_y \kappa_p)^2} - \frac{2v}{x_{la}^2} + K_r \frac{2}{x_{la}} \right) v_{des} \sin(\psi_e + \beta) - K_r \left(\frac{\kappa_p}{1 - e_y \kappa_p} - \frac{2e_y}{x_{la}^2} \right) v_{des} \\ - (K_\beta + K_r)r - \frac{2\kappa_p v \cos^2(\psi_e + \beta)}{x_{la}^2} v_{des} + \left(\frac{1}{(1 - e_y \kappa_p)^2} - K_\beta f'_{\beta^{eq}} \right) \dot{\kappa}_p v_{des} \quad (5-33) \end{aligned}$$

with

$$K_{F_{y,f}} = \frac{a}{I_z} - \frac{K_\beta}{mv_x} + \frac{2v_{des}}{mv_x x_{la}} \cos(\psi_e + \beta) \quad (5-34)$$

and

$$K_{F_{y,r}} = \frac{b}{I_z} + \frac{K_\beta}{mv_x} - \frac{2v_{des}}{mv_x x_{la}} \cos(\psi_e + \beta). \quad (5-35)$$

5-4-2 Control input coordination

The resulting controller equation (Equation 5-33) determines a combination of the front and rear lateral tyre forces, required to minimise the yaw rate, body sideslip angle and path-tracking errors. To calculate the separate tyre forces, however, the value of one of the tyre forces is required. Hindiyeh uses two controller modes to find the separate tyre forces; a steering mode and a throttle mode[10].

Steering mode The steering mode is the initial mode of the controller. In this mode, the steering angle is used to control the drift and the throttle input to control the longitudinal velocity of the vehicle. The following steps are taken to find the lateral tyre forces:

1. A desired longitudinal wheel slip is calculated by feedforward from the equilibria and feedback on the velocity by

$$\lambda_{des} = \lambda^{eq} + K_v(v_{des} - v). \quad (5-36)$$

2. Via the tyre model the rear lateral tyre force is calculated from the desired longitudinal wheel slip, wheel slip angle and wheel load,

$$F_{y,r} = f_{t,r}(\lambda_{des}, \alpha_r, F_{z,r}). \quad (5-37)$$

3. With the controller equation, the required front lateral tyre force is obtained.

4. The front lateral tyre force is converted to a front wheel slip angle via an inverse tyre model and an estimate of the front longitudinal wheel slip and load

$$\alpha_f = f_{t,f}^{-1}(F_{y,f}, \lambda_f, F_{z,f}), \quad (5-38)$$

and subsequently transformed to a steering angle by

$$\delta = \alpha_f + \arctan\left(\beta + \frac{ar}{v_x}\right). \quad (5-39)$$

Throttle mode In the final step of the steering mode the front wheel slip angle is calculated. It could, however, occur that the desired front lateral tyre force is unreachable due to tyre force or actuator limits. In this case, the controller switches to the throttle mode. The following steps are taken to find a new combination of lateral tyre forces:

1. The limited value of the front lateral tyre force is used as input for the controller equation, resulting in a new rear lateral tyre force.
2. An inverse tyre model of the rear wheels is used to find the appropriate longitudinal wheel slip from the lateral tyre force:

$$\lambda_{des} = f_{t,r}^{-1}(F_{y,r}, \alpha_r, F_{z,r}). \quad (5-40)$$

By switching between the two controller modes, the controller can stabilise the vehicle in a large range of equilibrium states and for fairly significant friction variations[10]. Since the controller most of the time operates in steering mode, the velocity remains fairly constant. When in danger of exiting the drift, however, the velocity error is temporarily sacrificed to maintain the drift.

Because of the addition of the path-tracking capabilities to the drift controller, the controller modes need to be adjusted. A situation can occur where the actions required to minimise the path tracking errors are the direct opposite of the actions required to sustain the drift. Take, for example, a vehicle that is in danger of spinning and has path-tracking errors. To prevent the vehicle from spinning, the yaw rate has to decrease. But, at the same time, the path-tracking errors dictate the yaw rate to increase, to bring the vehicle back to the path. Both errors require the opposite steering action and the taken action will, therefore, not resolve any of the errors. If the rear lateral tyre force, however, increases, less steering action is required to prevent the vehicle from spinning. Equation 5-33 finds a relationship between the front and rear lateral tyre force to solve both the path tracking and drift errors. If a rear lateral tyre force is found that (partly) solves the drift errors, the difference between the desired steering actions, for drift control and path-tracking, becomes smaller. Furthermore, since drifting is an unstable cornering condition, maintaining the drift is of higher importance than following the path. For this reason, a new definition of the desired longitudinal wheel slip in step 1 of the steering mode, is defined. The new longitudinal wheel slip is calculated based on the velocity and the yaw and body sideslip dynamics as follows:

$$\lambda_{des} = \lambda^{eq} + K_{v,t}(v_{des} - v) + K_{r,t}e_{r,t}, \quad (5-41)$$

where the subscript t denotes the gains and errors are part of the throttle controller. Via the same nested loop structure, the sideslip dynamics are controlled via the yaw dynamics. The desired yaw rate is given by

$$\begin{aligned} r_{des,t} &= r^{eq} + K_{\beta,t} e_{\beta}, \\ &= \kappa_p v_{des} + K_{\beta,t} (\beta - f_{\beta^{eq}}(\kappa_p v_{des})). \end{aligned} \quad (5-42)$$

Note that the reference yaw rate and body sideslip angle both depend on the path curvature, not the desired curvature used for path-tracking. This is because otherwise the same opposition in yaw rate as mentioned in the example would occur in this controller. The path-tracking errors will be resolved via the controller equation (Equation 5-33). The yaw error is defined by

$$e_r = \begin{cases} r_{des,t} - r & \text{if } r_{des,t} \geq 0 \\ r - r_{des,t} & \text{if } r_{des,t} < 0 \end{cases}. \quad (5-43)$$

The sign of the yaw error is changed because the direction of the rear lateral force is not changeable by the longitudinal wheel slip. This error definition makes sure that if the magnitude of the yaw rate has to increase, the desired longitudinal wheel slip increases.

Chapter 6

Simulation

This chapter will elaborate on the implementation of the controller in a simulation environment. First, the appropriate controller gains are determined for both the typical cornering controller and the drift controller. Subsequently, the performance of the controller is judged based on a sensitivity analysis. Finally, the required steps to transfer the vehicle from typical cornering conditions to a drift are discussed and implemented.

6-1 Typical cornering controller

The typical cornering controller, as defined in section 5-3, has five parameters to tune; the look-ahead time for lateral control, two gains for the velocity control and two gains for the wheel slip controller.

The first parameters to be found are the two controller gains of the wheel slip controller from Equation 5-4. Step inputs of various magnitudes are used as reference longitudinal wheel slip. From these inputs, an initial set of controller gains can be found. In typical cornering conditions, the rear longitudinal wheel slips remain at much lower levels than while drifting. In drift conditions, on the other hand, the wheel slips are much higher. For this reason, the final values of the wheel slip controller are obtained during the tuning process of the drift controller. The found values for the controller gains of the wheel slip controller are 25 for the proportional gain, K_λ , and 200 for the integral gain, $K_{\lambda,i}$.

Next, the controller gains for the velocity controller from Equation 5-12 are obtained. The reference velocity is varied between 1 m/s and 2.5 m/s by a combination of ramp, step and sine inputs. The best performing controller gains are found to be 0.3 for the proportional gain, K_v^{tc} , and 0.1 for the integral gain, $K_{v,i}^{tc}$. The superscript tc indicates that the controller gain belongs to the typical cornering controller.

The lateral controller from subsection 5-3-1 has only one parameter to tune; the look-ahead time. By comparing the path-tracking capabilities for various look-ahead times and velocities, the most appropriate parameter value is found. The path the vehicle has to follow consists

of a combination of straights and corners. From the equilibrium analysis, the maximum yaw rate for each velocity in typical cornering conditions is obtained. From the maximum yaw rate, a maximum driven curvature is deduced. The curvature used to test the path-tracking capabilities are set at 80% and 95% of this curvature. The transitions from the straight parts to the corners and the other way around are varied in length from 1 to 2 meters. The optimal look-ahead time is found to be 0.45 seconds.

The resulting controller gains for the typical cornering controller are summarised in Table 6-1.

Table 6-1: Controller gains for the typical cornering controller

| Controller gain | Value |
|-----------------|--------|
| t_{la}^{tc} | 0.45 s |
| K_v^{tc} | 0.3 |
| $K_{v,i}^{tc}$ | 0.1 |
| K_λ | 25 |
| $K_{\lambda,i}$ | 200 |

6-2 Drift controller

The main objective of the drift controller is to minimise the path-tracking errors. While doing so, it has to stabilise the drifting vehicle around the desired drift equilibrium. The drift equilibrium used to determine the controller gains is summarised in Table 6-2. In the remainder of this chapter, this equilibrium point will be referenced as the 'reference equilibrium'.

In typical cornering conditions, lateral and longitudinal control are addressed by a separate controller. The drift controller, as defined in section 5-4, takes care of both. The six parameters of this controller, however, are difficult to determine all at once. For that reason, first, a subset of the controller gains is determined, without taking path-tracking into account. The latter is achieved by using a very large look-ahead time. With this simplification, the values for three of the six parameters can be determined; K_β^d , K_r^d and $K_{v,t}^d$. The superscript d indicates that the controller gains belong to the drift controller. The initial states of the vehicle model correspond to the reference equilibrium, and the objective of the controller is to stabilise the vehicle around the corresponding states. When the controller achieves to stabilise the vehicle, the look-ahead time is gradually decreased, and the values for the remaining three parameters, t_{la}^d , $K_{\beta,t}^d$ and $K_{r,t}^d$ are determined. A summary of the final controller gains is given in Table 6-3.

Table 6-2: Equilibrium point to which the controller is tuned

| State | Value |
|------------|------------|
| v | 1.8 m/s |
| β | -0.295 rad |
| r | 1.38 rad/s |
| δ | -0.1 rad |
| ω_r | 62.6 rad/s |

Table 6-3: Controller gains of the drift controller

| Controller gain | Value |
|-----------------|-------|
| t_{la}^d | 1.4 |
| K_β^d | 7.8 |
| K_r^d | 4.2 |
| $K_{v,t}^d$ | 0.6 |
| $K_{\beta,t}^d$ | 6.0 |
| $K_{r,t}^d$ | 0.3 |

6-2-1 Sensitivity analysis

The controller gains are found to keep the vehicle at the reference equilibrium. But, the controller should be able to stabilise the vehicle when the states are not exactly at their equilibrium value. A sensitivity analysis is performed to test the performance of the controller around the reference equilibrium. In this analysis, the sensitivity of the controller to changes in initial conditions, reference values or model parameters is analysed.

Initial path-tracking errors

First, the ability of the controller to return the vehicle to the path, if initialised with a lateral or course offset, is analysed. Multiple simulations are performed with the lateral error varied between ± 0.3 m and the course error between ± 0.15 rad. Other vehicle states are unchanged and correspond to the reference equilibrium point. In Figure 6-1 the responses from the various initial path-tracking errors are shown. The figure shows that the controller achieves to stabilise the vehicle at the reference equilibrium within approximately 4 to 7 seconds, depending on the magnitude of the initial errors. From the phase portrait in Figure 6-2 it becomes apparent that the path-tracking errors are resolved in a spiral motion. A vehicle can, in general, only move in lateral direction, if it moves in the longitudinal direction because only the front wheels are steered. To minimise a lateral error, the vehicle has to move towards the path. This, however, means that the direction of motion will not align with the path tangent. The initial positive lateral error of the purple line, for example, is decreased by first decreasing the course error to a negative value. This results in the spiral-shaped phase portrait.

The red and purple lines in the figures represent the responses with the largest initial errors. The lines both start at the same absolute lateral and course offset, but with opposite signs. Even though the errors have the same magnitude, the difference in settling time is significant. The purple line corresponds to the vehicle starting on the inside of the curve. Since the path has a circular shape, the vehicle will move towards the path without any action taken. A short increase in yaw rate is, therefore, enough to bring the vehicle back to the path. The red line, on the other hand, corresponds to the vehicle starting on the outside of the curve, with its course directed away from the path. The initial actions that are taken to decrease the path-tracking errors, result in a significant velocity increase. With a larger velocity, the controller has to act faster to solve the path-tracking errors. In the phase diagram, the red line makes a full circle, before the path-tracking errors go to zero. This is because the first

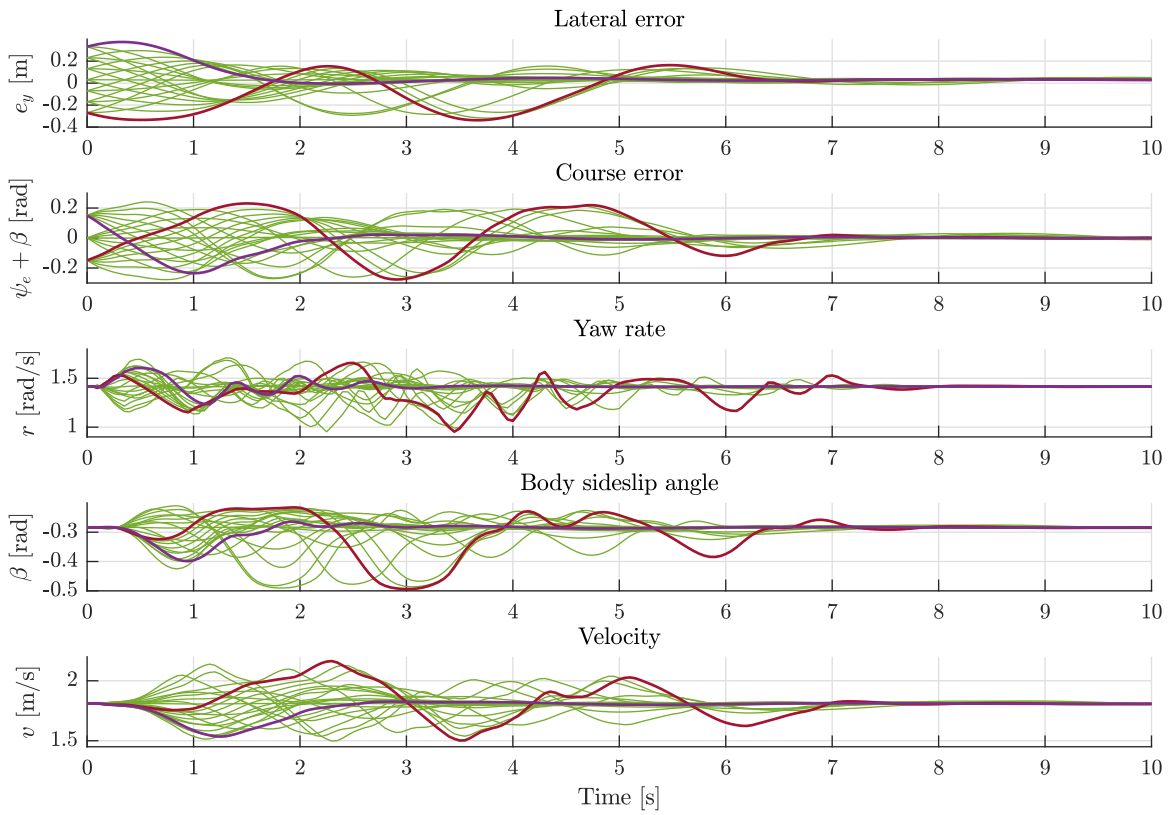


Figure 6-1: Response of the vehicle to initial offsets in lateral position and orientation

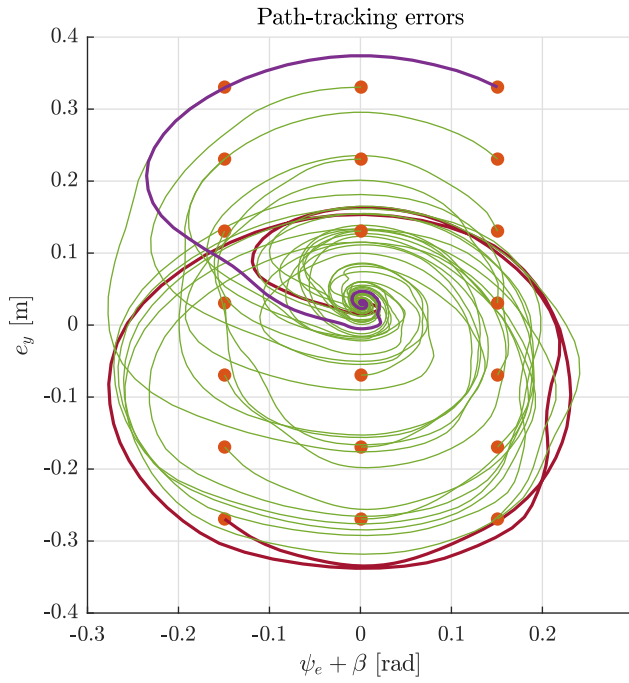


Figure 6-2: Phase plot of the response of the vehicle to initial offsets in lateral position and orientation

time the vehicle reaches the path (at $t = 1.5\text{s}$) the velocity is too high. After the vehicle cuts the corner, the controller is unable to keep it within the curve. The second time the vehicle moves towards the path (at $t = 4.5\text{s}$) at a lower velocity and the controller is able to keep the vehicle within the curve.

Initial body sideslip angle and yaw rate errors

In Figure 6-3 the responses for perturbations in body sideslip angle and yaw rate are shown. The initial conditions correspond to the left-hand drift equilibria from Figure 4-6. The controller is able to stabilise the vehicle for all initial errors. However, a significant difference in settling time between the red and purple response can be observed, especially regarding the path-tracking errors. The phase portrait of the body sideslip angle and the yaw rate for the same responses is shown in Figure 6-4. The phase trajectories show a somewhat spiral motion around the steady-state values. Striking is, that the phase trajectories that start on the right top of the plot end up at the starting points of the phase trajectories on the bottom left of the plot. To increase the body sideslip angle of the purple response, the throttle is increased. This, however, also results in increased velocity and the course of the vehicle moving away from the path. To resolve the course error, the yaw rate has to remain large. As a result, a large overshoot in body sideslip angle can be observed. The red response already starts at a large body sideslip angle. By decreasing the throttle input, the yaw rate decreases and, subsequently, the body sideslip angle decreases. This, however, results in a much smaller velocity error, which makes it easier for the controller to resolve.

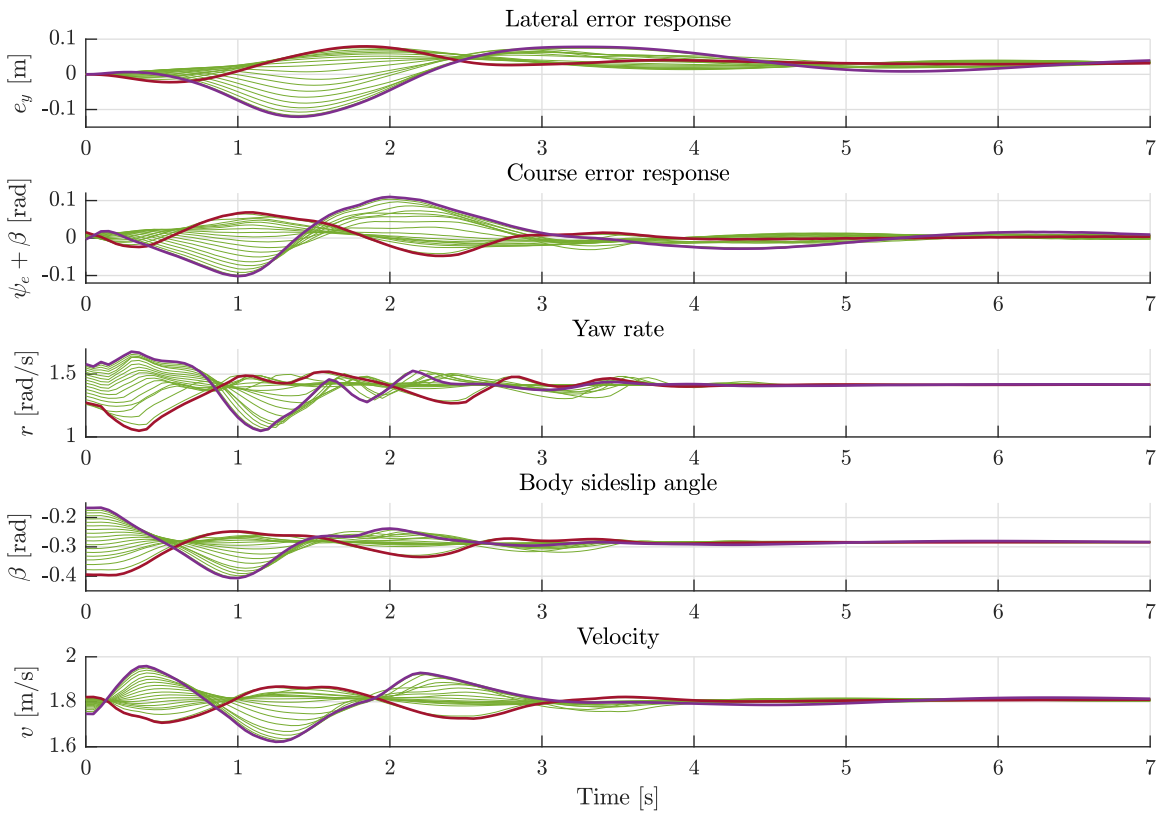


Figure 6-3: Response of the vehicle to perturbations in body sideslip angle and yaw rate

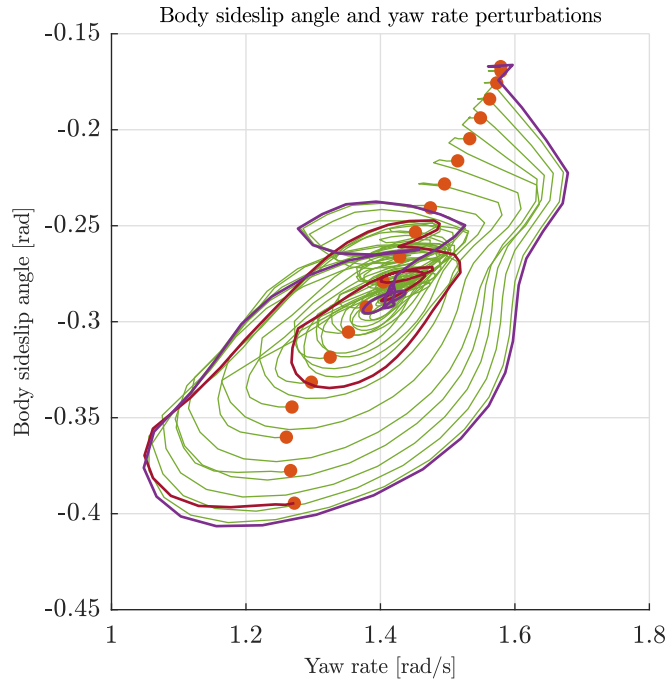


Figure 6-4: Phase plot of response of the vehicle to perturbations in body sideslip angle and yaw rate

Performance around other equilibria

Next, the controller performance is evaluated around other equilibria. From the equilibrium analysis in section 4-3, a range of left-hand drift equilibria is selected for velocities from 1.6 to 2 m/s, starting at the lowest equilibrium yaw rate. Figure 6-5 shows for which equilibria the controller is able to stabilise the vehicle when tuned for the reference equilibrium (indicated by the solid blue dot in the figure).

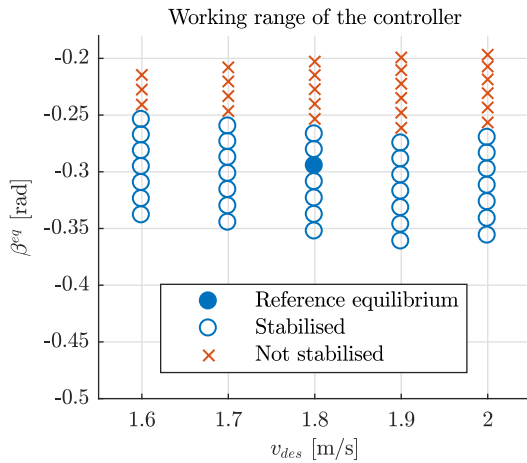


Figure 6-5: Range of equilibria, around the tuned equilibrium, where the controller succeeds in stabilising the vehicle

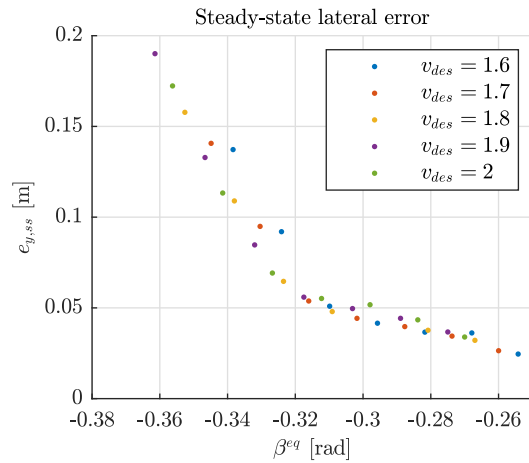


Figure 6-6: Steady-state lateral error for various drift equilibria

The figure implies that the controller performs particularly well for large sideslip angles. Regarding stabilisation, this is indeed the case. The path-tracking performance, on the other hand, decreases for a larger body sideslip angle. In Figure 6-6 the steady-state lateral error versus the equilibrium body sideslip angle is shown. For a body sideslip angle above -0.32 rad, a steady-state lateral error of below 5 cm is observed, which is acceptable. Below this sideslip angle, however, a significant increase in steady-state lateral error can be observed. For some reason, the controller is unable to bring the vehicle to the desired equilibrium. It does, however, stabilises the vehicle at another equilibrium, with a lower velocity and higher yaw rate. In Figure 6-7 the range of equilibrium body sideslip angle and yaw rate are shown for different velocities. From the figure, it can be observed that at a lower velocity a higher equilibrium yaw rate can be found for the same body sideslip angle.

The desired longitudinal wheel slip (Equation 5-41) is based on a combination of the velocity error, yaw rate error and body sideslip error. The combined error can, therefore, be equal to zero, when the separate errors have a non-zero value. In the same sense, the desired yaw rate in Equation 5-22, depends on the body sideslip error and the path-tracking errors. The controller finds an equilibrium that minimises both combined errors, and in this situation, this results in a lower velocity, yaw rate and slightly smaller body sideslip angle. The reason why the controller does not settle at the desired equilibrium probably originates from the definition of the equilibria. These are found for the five degrees-of-freedom bicycle model, so only two wheels and, thus, no lateral load transfer are taken into account. At a large body sideslip angle, the behaviour of the rear tyres enters the highly nonlinear region beyond

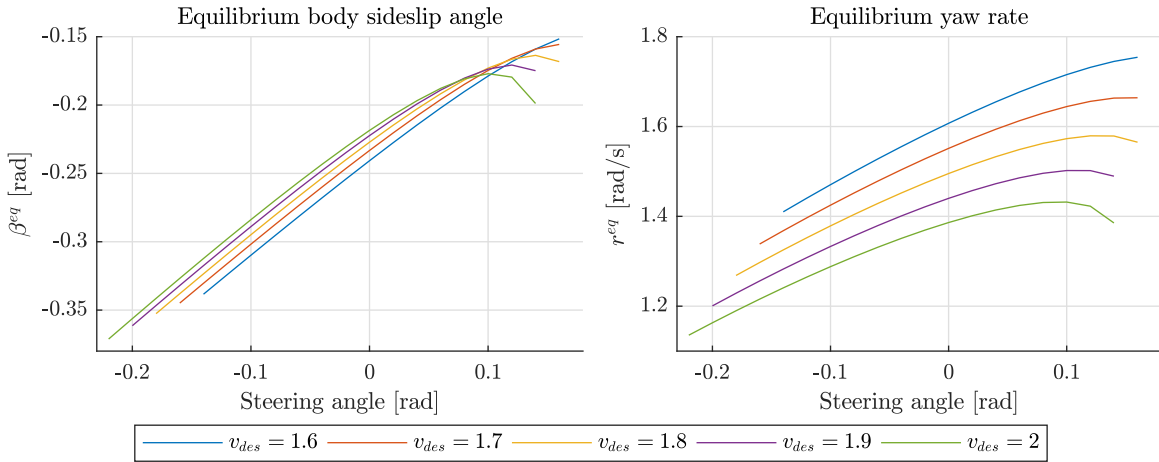


Figure 6-7: Equilibrium body sideslip angle and yaw rate for different velocities

the tyre force peak. Neglecting the lateral load transfer and the characteristics of two rear wheels, therefore, results in a slightly different equilibrium that would be found for the vehicle model with these dynamics taken into account. The controller, therefore, settles at another equilibrium that balances the combined errors.

At body sideslip angles above approximately -0.25 rad, the controller is unable to stabilise the vehicle at the desired equilibria. In the equilibrium analysis in section 4-3, it is shown that the smaller the equilibrium body sideslip angle gets, the closer the front tyres are to saturation. Near the limit of the tyre force, the curve of the tyre force versus the wheel slip angle becomes less steep. In other words, in this region, a small change in desired lateral force requires a significant change in steering angle. This results in abrupt changes in the steering angle, which in its turn results in oscillations in the yaw rate. For equilibria with a smaller body sideslip angle, the oscillations eventually reach become too large for the controller to stabilise the vehicle. In Figure 6-8 the response of the controller trying to stabilise the vehicle at an equilibrium point with $v_{des} = 1.8$ m/s and $\beta^{eq} = -0.26$ rad is shown. In this response, large variations in body sideslip angle and velocity can be observed. The plot of the rear longitudinal wheel slip shows that the controller switches multiple times between steering and throttle mode. In throttle mode, the controller is able to bring the body sideslip angle close to the reference and at the same time minimise the path-tracking errors. This, however, at the cost of an increasing velocity. As soon as the controller switches back to steering mode, it tries to decrease the velocity error, by decreasing the rear longitudinal wheel slip. While doing this, body sideslip angle becomes larger. The controller tries to prevent this by counter-steering, which in its turn results in the vehicle deviating from the path. Additionally, again a mismatch in equilibrium states is expected to cause problems. Equilibria with a small body sideslip angle correspond to high lateral accelerations (Figure 4-6). The influence of lateral load transfer on the tyre forces, therefore, becomes significant. The found equilibrium states, therefore, do not correspond to an equilibrium for the seven degrees-of-freedom vehicle model.

Note that in this analysis, the controller is optimised for the reference equilibrium and the performance is examined for other equilibria. The performance of the controller at other equilibria can be improved by tuning the controller parameters for this equilibrium specifically. It could, therefore, also be possible to stabilise the vehicle around equilibria where the controller

currently fails. However, close to saturation of the front tyres, stabilising the vehicle remains difficult, since the influence of the steering angle is only limited. The controller mainly has to use the throttle input to control the vehicle, which results in large velocity errors. The improvement of the controller performance for the equilibria with a small body sideslip angle is, therefore, expected to be minimal.

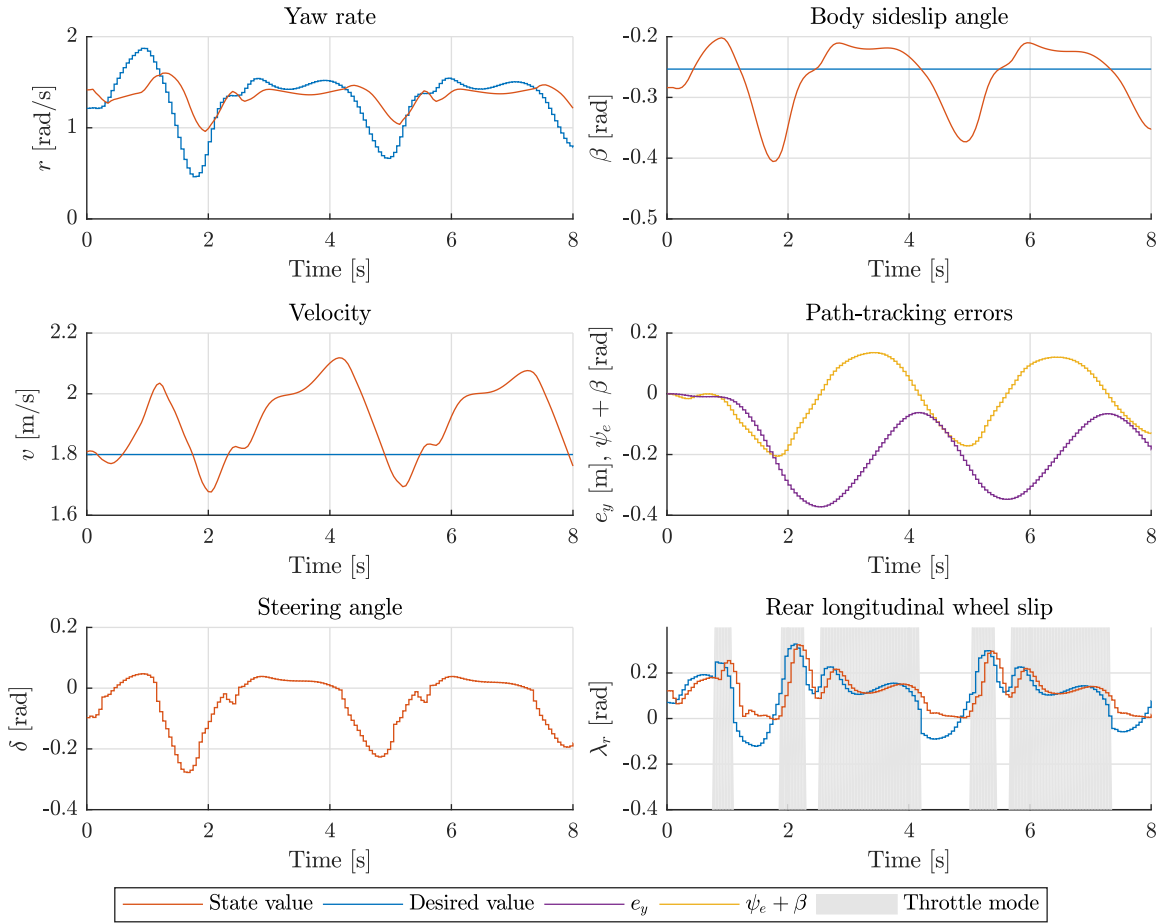


Figure 6-8: Response of the failing stabilisation of the vehicle at an equilibrium point with $v_{des} = 1.8$ m/s and $\beta^{eq} = -0.26$ rad.

Parametric robustness

The vehicle model, found in chapter 7, is based on driving experiments with the Delft Scaled Vehicle (DSV). Since the vehicle model is simplified and the found parameters are an estimation, differences between the actual vehicle and the vehicle model are present. The drift controller is based on the estimated vehicle properties and uses the same parameters as the vehicle model. The tyre models used in the controller, for example, are based on the same tyre parameters. The translation from tyre force to wheel slip angle, therefore, is the same as in the vehicle, albeit with lateral load transfer neglected. Since the vehicle model is an estimate of the behaviour of the DSV, the performance of the controller should be checked for the case that some of the vehicle model characteristics are changed. Because the controller

is highly dependent on the tyre model of the vehicle, especially changes in this area will be tested.

In Figure 6-9 the vehicle response to variations in tyre-road friction is shown. The reference equilibrium is used as initial conditions and reference. The friction is varied by $\pm 10\%$ around the actual friction factor. The controller is able to stabilise the vehicle at lower friction, albeit at a different yaw rate and body sideslip angle. The decrease in friction results in lower tyre force limits. This means that the lateral tyre force of the saturated rear tyre is lower. Initially, this results in an increasing yaw rate. However, to prevent the vehicle from spinning, the controller decreases the front lateral force by counter-steering. The yaw rate decreases and the vehicle settles at a larger body sideslip angle and smaller yaw rate than the reference.

For an increased friction factor, the response is the other way around. The rear lateral tyre force is larger, meaning the vehicle is in danger of exiting the drift. The rear longitudinal wheel slip has to increase, to decrease the lateral tyre force. But, since the controller 'expects' the tyre forces to be smaller, the action it takes is insufficient. Sufficient throttle input is, therefore, not reached, until the errors are much larger, resulting in large oscillations and an increasing deviation from the path. The controller is able to prevent the vehicle from spinning or exiting the drift, but the path-tracking capabilities are sacrificed to reach this goal and a significant deviation in lateral error is observed.

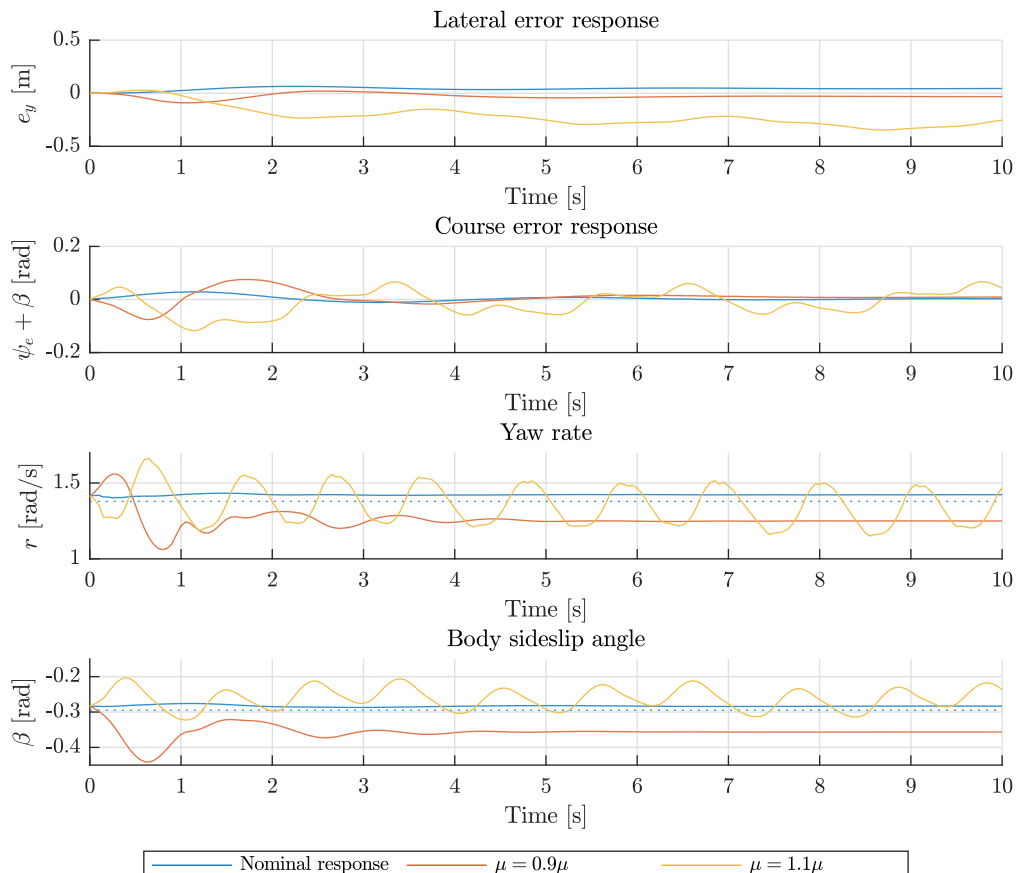


Figure 6-9: Response for changes in tyre-road friction

In Figure 6-10 the vehicle response to variations in cornering stiffness is shown. The cornering stiffness influences the slope of the lateral tyre force curve. An increased cornering stiffness results in an increased slope, and vice versa. In other words, a change in wheel slip angle results in a larger increase in tyre force. The decreased cornering stiffness has a small influence on the vehicle response; the path-tracking errors slightly increase. The effect of increasing the cornering stiffness is much larger. Because of the increased slope of the tyre force curve, a change in steering angle results in a larger increase or decrease in lateral tyre force than expected. This results in yaw rate and body sideslip oscillations. The controller is, however, still able to stabilise the vehicle around the path.

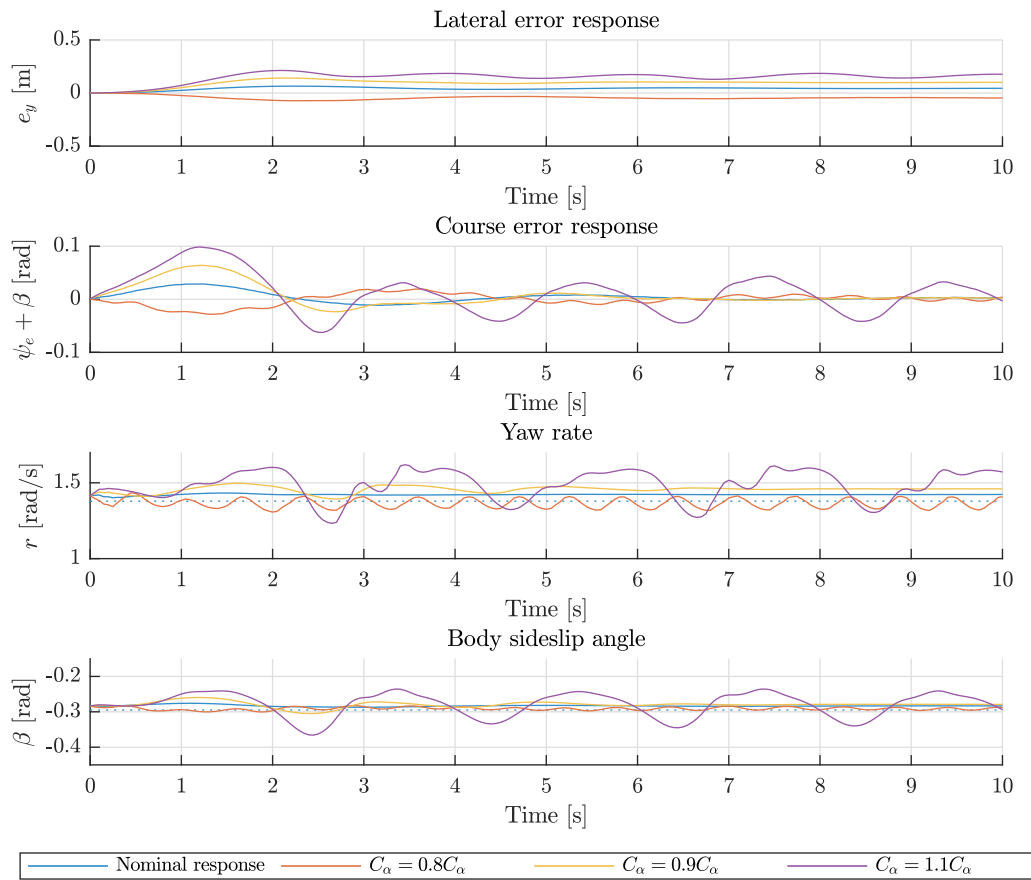


Figure 6-10: Response for changes in cornering stiffness

6-3 Entering the drift

In simulation, the vehicle model can be initialised at a drift equilibrium. In an actual vehicle, however, this is not possible. The controller should, therefore, be able to transfer the vehicle from typical cornering conditions to drifting.

Different methods can be used to induce a drift[30]. All methods, however, boil down to the same principle; first, a yaw motion is induced by steering into the corner. When the vehicle is rotating, the rear tyres are saturated to decrease the lateral tyre force. This is done by

braking or a large throttle input. Because the rear lateral tyre force decreases, the rear-end of the vehicle starts sliding out of the curve. When nearing the desired body sideslip angle, the yaw rate is decreased by counter-steering and decreasing the throttle input.

The controller defined in chapter 5, follows the same steps to induce a drift. During typical cornering, the reference body sideslip angle is switched from a typical cornering equilibrium to a drift equilibrium that corresponds to the path curvature. Simultaneously the controller is switched from typical cornering to drift mode. The drift controller increases the desired wheel slip to minimise the large body sideslip error. When the body sideslip angle becomes larger, the controller starts counter-steering and decreases the throttle.

Without any adaptations, simply switching between the controllers brings the vehicle into a drift. During the transition, however, significant path-tracking errors are observed. The increasing throttle input results in a velocity increment. Furthermore, after saturation of the rear tyres, the rear-end of the vehicle starts sliding out of the curve. The combination of both factors, result in the vehicle moving away from the path. By intentionally steering to the inside of the curve, before increasing the throttle, the final deviation from the path can be decreased. Because the yaw rate increases, as a result of the increased steering angle, the vehicle will rotate faster and deviate less from the path. The delay to the throttle input is added to the controller by performing the switch to the drift controller in two steps. First, the authority over the steering angle is switched to the drift controller, which will increase the steering angle. After a certain amount of time, the authority over the throttle input is also switched to the drift controller. From manual tuning, the best performance is found for a delay of 0.5s between switching the steering and throttle input.

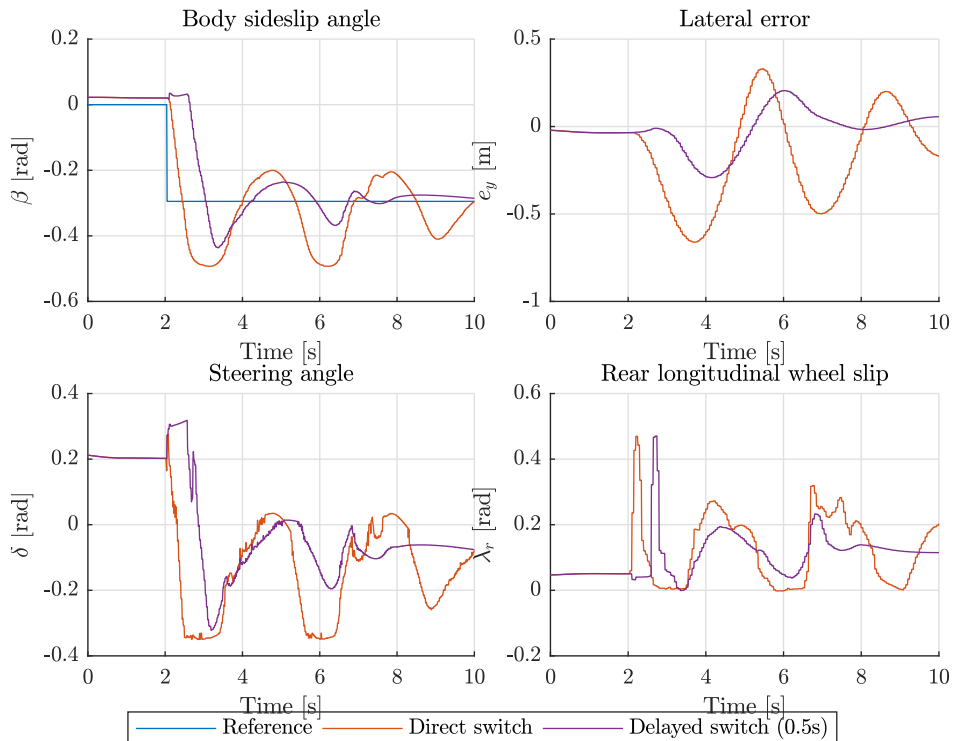


Figure 6-11: Comparison between direct switching and delayed switching to transfer the vehicle from typical cornering conditions to the reference drift equilibrium.

In Figure 6-11 a comparison between the two switching methods is shown. First, the controller steers into the curve, by increasing the steering angle. As soon as the throttle input is increased, the controller starts counter-steering. By waiting for 0.5s before increasing the throttle, the maximum lateral deviation is decreased from 0.6 m to 0.3 m. The body sideslip angle, however, still shows a large overshoot. Additional counter-steering is, therefore, required, to prevent the vehicle from spinning. This results in the vehicle deviating from the path. Another way of preventing spinning is to decrease the rear longitudinal wheel slip. The longitudinal wheel slip, however, is controlled by the drift controller. Adjustments to its behaviour will also influence the controller performance while maintaining the drift. For that reason an additional controller is added, to determine the desired longitudinal wheel slip during the transition. This controller is based on the yaw rate and body sideslip error and the equilibrium wheel slip. The desired longitudinal wheel slip, during the transition, is defined by

$$\lambda_{des}^t = K_\beta^t e_\beta + K_r^t e_r + \lambda^{eq}, \quad (6-1)$$

where the superscript t indicates that the gains belong to the transition mode of the controller. The controller parameters, used to induce the drift are summarised in Table 6-4

Table 6-4: Controller gains for the transition from typical cornering to drifting

| Controller gain | Value |
|-----------------|-------|
| t_{switch} | 0.5 s |
| K_β^t | 1.4 |
| K_r^t | 0.15 |

The resulting switching scheme is summarised by the following steps:

1. The vehicle drives in typical cornering conditions
2. The reference body sideslip angle switches to a drift equilibrium sideslip angle
3. The drift controller takes over control of the steering angle
4. After t_{switch} the desired longitudinal wheel slip is controlled via Equation 6-1
5. The drift controller takes over throttle control if the body sideslip angle approaches its desired value

With this addition, the controller achieves to bring the vehicle to the majority of the drift equilibria that are used in the sensitivity analysis. For equilibria with a yaw rate close to the maximum achievable yaw rate in typical cornering conditions, however, the additional steering action does not have the desired effect. The curvatures corresponding to these equilibria are of such a magnitude that the front tyres are already close to saturation in typical cornering conditions. In that case, increasing the steering angle will not result in sharper cornering. The controller should, in this situation, switch to drift mode before it enters the sharp curvature. For this reason, the controller switches to drift mode if the yaw rate, corresponding to the path curvature, is larger than 85% of the maximum drivable yaw rate at that velocity. This

value is chosen, since it corresponds to an equilibrium yaw rate approximately half-way the stabilizable equilibria.

In Figure 6-12 the vehicle response is shown for the transition from straight-ahead driving to drifting in a circle. The driven trajectory is shown in Figure 6-13. Before the vehicle reaches the final curvature, the controller switches to transition mode (indicated by the red dot in the trajectory plot). The vehicle starts steering into the corner, and after 0.5s the throttle is increased. The drop in velocity is a result of the quickly increasing steering angle and the decreasing longitudinal velocity reference, that is coupled with the body sideslip angle. The same manoeuvre is tested for the velocities and equilibria as used in the sensitivity analysis. For the majority of the equilibria, the lateral error remains between ± 0.1 m and reaches steady-state within a few seconds.

In summary, both the typical cornering and drift controller are evaluated in simulation. A sensitivity analysis is performed and shows that the drift controller can cope with various state perturbations and changes in driving conditions. Moreover, the controller can induce and subsequently sustain a drift while remaining close to the desired path. To evaluate the performance of the controller in more realistic conditions, the controller is implemented in the DSV in the next chapter.

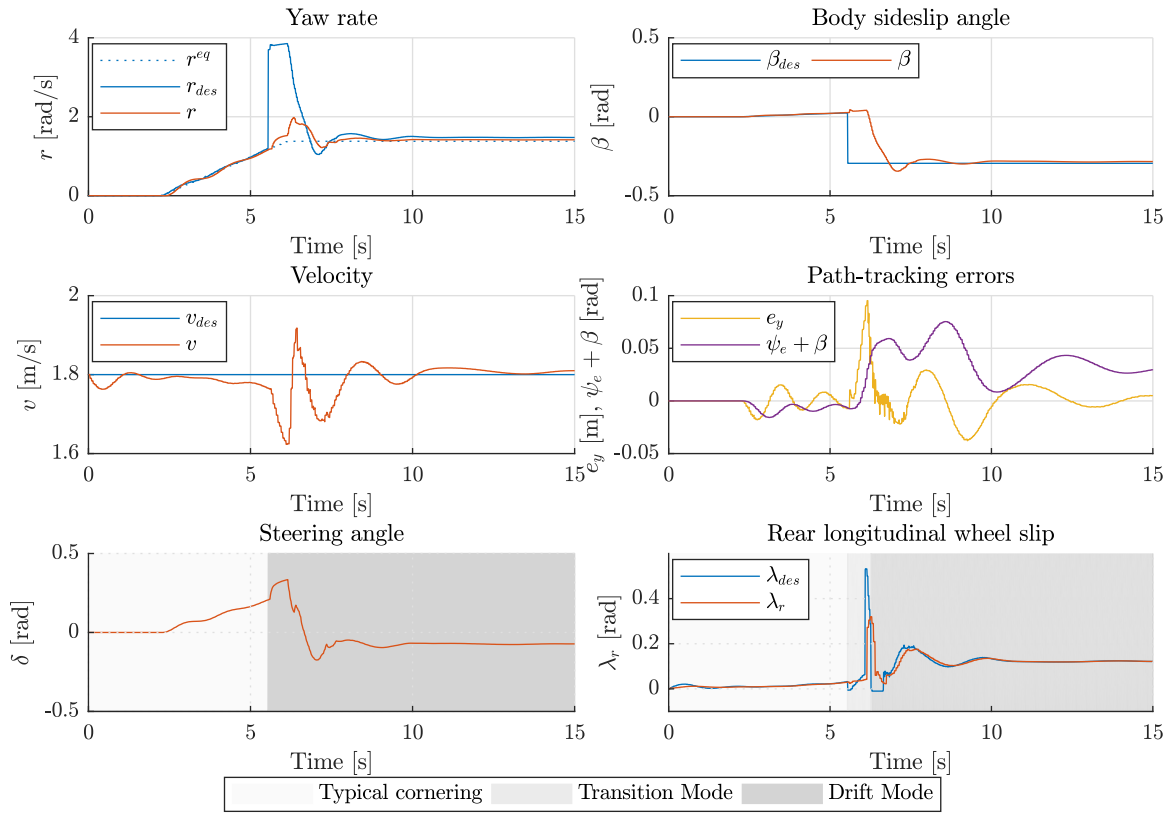


Figure 6-12: The transition from straight-ahead driving to drifting in a circle.

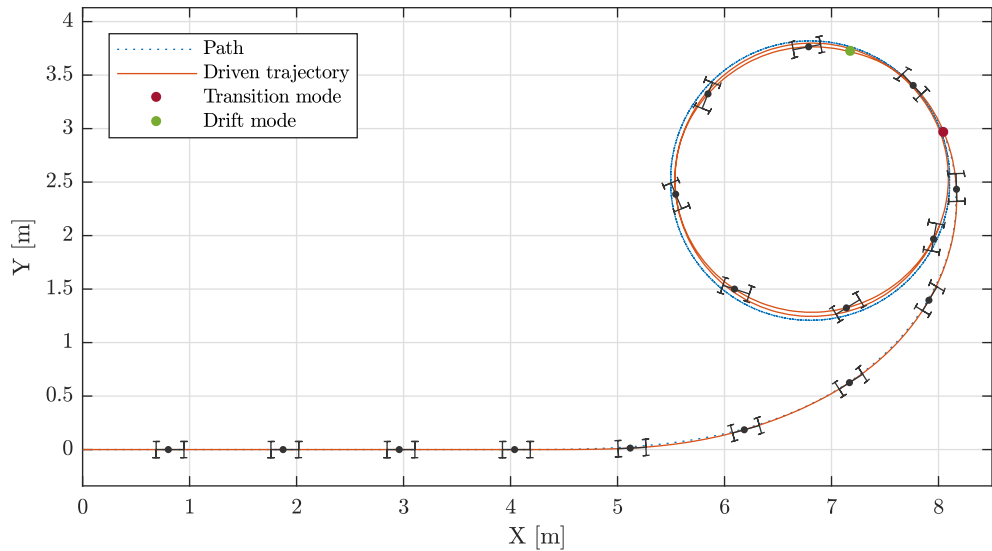


Figure 6-13: Trajectory of the transition from straight-ahead driving to drifting in a circle

Chapter 7

Implementation

This chapter describes the steps taken to implement the controller in the Delft Scaled Vehicle (DSV). First, a description of the sensors used on the DSV is given. The next part elaborates on the estimation of the required states from the sensor output. Finally, the controller is implemented in the DSV and tested in both typical cornering conditions and for drifting.

7-1 Actuator control and sensor reading

The DSV is equipped with multiple sensors: four encoders for wheel speed measurement, an Inertial Measurement Unit (IMU) for accelerations and yaw rate and a Lidar for positioning. The sensors and actuators are connected to an onboard computer, which runs the Robotic Operating System (ROS). This operating system enables communication between the actuators, sensors and the controller. Via a wireless network, an external computer is connected that runs the software to process the Lidar measurements and runs the controller. In Figure 7-1 the DSV is shown, with the various sensors and systems indicated.

In Table 7-1 the frequencies and latencies corresponding to the actuators and sensors are summarised. The latencies of the actuators are determined from an input signal in ROS to motion of the actuator. The latencies of the sensors are determined from motion to a usable, but unfiltered, state value. The large latency and low frequency of the Lidar measurements directly stand out. Especially for drifting, the size of the delay becomes problematic, as will be explained in subsection 7-2-5. For that reason, a Motion capture (Mo-cap) system is used for the implementation of the drift controller. The Mo-cap system uses multiple fixed cameras to determine the position and heading of the vehicle with high accuracy and at a high rate.

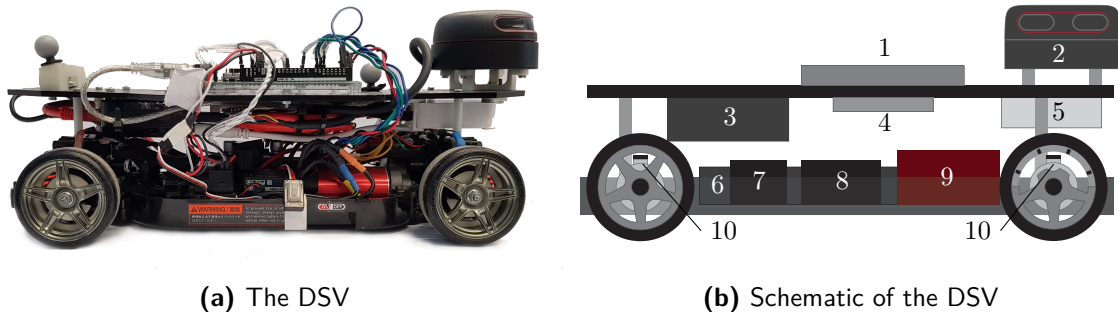


Figure 7-1: The DSV. With 1: Arduino, 2: Lidar, 3: Onboard computer, 4: IMU, 5: Router, 6: Battery, 7: Servo, 8: Motor controller, 9: Motor, 10: Encoders.

Table 7-1: Overview of sensor output frequencies and actuator input frequencies

| Device | Frequency | Latency |
|----------------|--------------|---------|
| Steering input | 30 Hz | <0.05s |
| Throttle input | 30 Hz | <0.05s |
| Encoders | 30 Hz | 0.05s |
| IMU | 100 Hz | <0.05s |
| Lidar | 10 Hz | 0.15s |
| Mo-cap | 120 – 240 Hz | <0.05s |

Table 7-2: Overview of the sensors used to estimate the vehicle states

| State | Used sensor |
|------------|---------------------------|
| X, Y | Lidar |
| ψ | IMU and Lidar |
| v_x | Encoders and Lidar/Mo-cap |
| v_y | Lidar/Mo-cap |
| r | IMU |
| a_x | IMU |
| a_y | IMU |
| ω_j | Encoders |

7-2 State estimation

The measurements from the sensors are used to estimate the required vehicle states. In Table 7-2 an overview is given of the sensors used to estimate the vehicle states. This section elaborates on the state estimation from the raw outputs of the sensors.

7-2-1 Accelerations and yaw rate

The accelerations and yaw rate can directly be obtained from the IMU output. The noise level on the acceleration measurements, though, is very high. But, since these are only used for estimation of the wheel loads, a lag resulting from excessive filtering is acceptable. The equation of the discrete low pass filter for both accelerations is given by

$$H(z) = \frac{0.0609}{z - 0.9391}. \quad (7-1)$$

The noise level on the yaw rate measurement, on the other hand, is very low. A moving average with a sliding window of three samples is therefore sufficient to smoothen the measurement.

The moving average of the yaw rate calculated by

$$r_{filt}(n) = \frac{1}{N} \sum_{i=0}^{N-1} r(n-i), \quad (7-2)$$

where N is the number of samples in the sliding window of the moving average.

7-2-2 Wheel speeds

The wheel speeds of the DSV are measured with encoders based on magnetism. In the rim of the wheels, eight magnets are placed. Every time one of the magnets passes the sensor, a pulse is determined by the Arduino, which communicates the measurements to the onboard computer at a frequency of 30 Hz. Two methods can be used to translate these pulses into a wheel speed. The first method uses the time between two pulses to calculate the angular velocity by

$$\omega = \frac{2\pi}{n_{mag}\Delta t_{pulse}}, \quad (7-3)$$

where n_{mag} is the number of magnets corresponding to one rotation and Δt_{pulse} is the time between two pulses. Alternatively the wheel speed can be calculated by counting the number of pulses in a fixed amount of time, by

$$\omega = \frac{2\pi}{n_{mag}} \Delta t \ n_{pulse}, \quad (7-4)$$

where n_{pulse} is the number of pulses counted in time Δt , which is set to 1/30s to match the rate of the Arduino. Both methods have their upsides and downsides. The first method is accurate at low speeds, but becomes less accurate at high speeds. For the second method this is the other way around. Within the velocity range of where the vehicle is used, the first method is preferred. Furthermore, the used sensors are very sensitive to the placement of the magnets. During driving this often results in a missed magnet or a double magnet count. The first method, showed to be the least affected by these measurement errors. The remaining outliers resulting from the measurement errors, are removed by a median filter. A median filter calculates the moving median over time, for a certain amount of samples. The filter equation is given by

$$\omega_{filt}(n) = \text{median}([\omega(n) \ \omega(n-1) \ \dots \ \omega(n-(N-1))]), \quad (7-5)$$

where N is the number of samples in the sliding window. A window length of three samples is used to remove the outliers in the signal.

7-2-3 Position

The position of the vehicle is estimated with measurements from the Lidar. A Lidar uses a rotating laser to measure the distance to surrounding objects. Ten times a second a scan of the surroundings with a resolution of 1° is sent to the onboard computer. These scans can be translated into a pose (location and heading) with various methods, two of them are Simultaneous Localization And Mapping (SLAM) and scan matching. SLAM uses the scans

to create a map of the surroundings and simultaneously determine the location of the vehicle within this map. The scan matching approach compares the latest scan with one or more previous scans to find its position relative to the previous point. Because of noise in the sensor measurements, the found positions have a small deviation from the actual position. In the scan matching approach, this results in a drifting position estimate. Because the SLAM approach determines the vehicle's position relative to a map, the position remains accurate over time. For path-tracking purposes, the SLAM method is, therefore, preferred.

The software used to perform SLAM is the ROS package `hector_slam`[31], which translates the scan data to a pose with a time stamp. Due to the sensor noise, the obtained positions do not form a smooth line. These small jumps are undesired in the calculation of the path-tracking errors. Therefore a polynomial is fitted to a range of previous position estimates, as shown in Figure 7-2. The polynomial not only results in a smoother position estimation, it is also used to estimate the vehicle's position between the scans of de Lidar. The latter is done by extending the polynomial with the driven distance since the last estimation position. In the figure this is indicated with the dashed line. The driven distance since the last received position is defined by

$$s(t) = \int_{t_{np}}^t v(t) dt, \quad (7-6)$$

where s is the driven distance since the last received position, t is the current time, t_{np} is the time instant corresponding to the last position and $v(t)$ is the velocity. Additionally, the polynomial can be extended even further, to account for the latency of the position estimation. The distance added to the polynomial is then given by

$$s(t) = \int_{(t_{np}-\Delta t_{pred})}^t v(t) dt, \quad (7-7)$$

where Δt_{pred} is the prediction time. Note that the prediction distance of this method is limited, since it predicts the motion of the vehicle based on previous positions. The predicted position is, therefore, only accurate if the vehicle motion remains approximately the same over the prediction distance.

The Mo-cap system provides the same output as the SLAM software does, albeit at higher accuracy (< 1 mm) and a higher rate. Because of this high accuracy and rate, fitting a polynomial is not required.

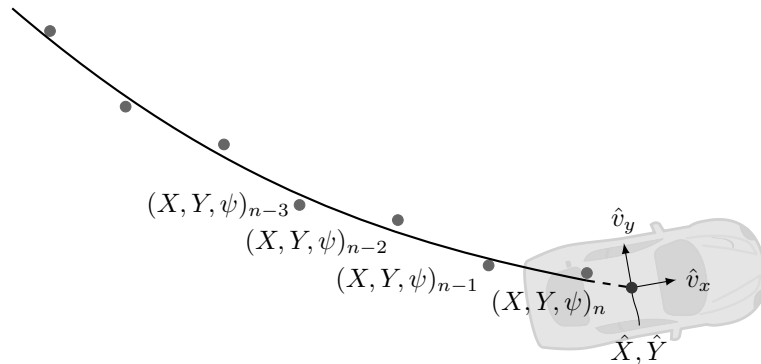


Figure 7-2: Position estimation from a polynomial fit to current and previous poses

7-2-4 Heading

The heading of the vehicle, ψ , is determined by both the SLAM software and the IMU. Based on the output rates of the sensors, the heading output from the IMU is preferred. Furthermore, at high yaw rates, the heading estimation of the IMU is much more accurate. Both measurements, however, have a different reference frame. SLAM uses the initial pose as a reference, the IMU, on the other hand, is based on the magnetic north pole. Since the vehicle is used indoors, the magnetic field is slightly disturbed and, therefore, the accuracy of the orientation depends on the position of the vehicle in the room. By subtracting the slowly varying bias from the IMU measurement, an accurate heading estimate can be obtained at a high frequency. The bias is determined by calculation of the moving average of the difference between the two measurements:

$$\tilde{\psi}(n) = \psi^{IMU}(n) - \frac{1}{N} \sum_{i=0}^{N-1} (\psi^{IMU}(n - c_f i) - \psi^{SLAM}(n - i)), \quad (7-8)$$

with

$$c_f = \frac{f^{IMU}}{f^{SLAM}}, \quad (7-9)$$

where $\tilde{\psi}$ is the heading estimate, ψ^{IMU} and ψ^{SLAM} are the headings obtained by the IMU and SLAM, respectively, N is the number of samples used to calculate the average and f^{IMU} and f^{SLAM} are the output frequencies of the IMU and SLAM, respectively. The factor c_f is added to the equation to account for the difference in sensor frequencies.

7-2-5 Velocities

By differentiation of the vehicle positions found by the SLAM software, the vehicle's longitudinal and lateral velocities, and thus the body sideslip angle, can be estimated. During drifting, though, it is important to react quickly to changes in body sideslip angle. Simulation analysis shows that with an output rate of 10 Hz, the controller often acts too late, resulting in oscillations in body sideslip angle and path-tracking errors. Adding to that the latency of the Lidar measurement and the additional delay resulting from the differentiation, the controller is unable to sustain a drift.

Alternatively, the longitudinal velocity of the vehicle can be estimated by using the wheel speeds of the front wheels. Since the front wheels of the DSV are not powered, they are rolling freely, and the longitudinal wheel slip is very small. By assuming the longitudinal wheel slip is equal to zero, the longitudinal velocity of the vehicle can be estimated by

$$\tilde{v}_x = R_e \frac{\omega_{fl} + \omega_{fr}}{2}. \quad (7-10)$$

The lateral velocity is not easily estimated via an alternative sensor. With a state observer, it should be possible to estimate the lateral velocity based on the lateral equations of motion, the longitudinal velocity estimate and the measured accelerations and yaw rate. However, because of the latency of the filtered acceleration measurements, the latency of the lateral velocity estimate could not be resolved. The combination of the low frequency and large latency of the Lidar measurements has led to the decision to use the faster Mo-cap system. This makes the use of a state observer for the lateral velocity unnecessary.

7-3 Implementation in the DSV

The final step in this research is to implement the controller in the DSV. First, the typical cornering controller is tested with both the Lidar and the Mo-cap system. Subsequently, the drift controller is implemented in the DSV and the results are discussed.

7-3-1 Typical cornering with Lidar

The controller is tested to follow the path as shown in Figure 7-3. The look-ahead time of 0.45s, that is used in simulation, resulted in significant oscillations around the path. For that reason, the look-ahead time is increased to 0.6s. Furthermore, in subsection 7-2-3 it was stated that the polynomial could be extended to account for the latency in the position estimation. Implementation quickly showed that this prediction resulted in oscillations, caused by the inaccuracy of the position estimate.

The driven trajectory is shown in Figure 7-3 and Figure 7-4 and will be discussed in five segments, indicated by the different colours. The path-tracking errors and steering angle, for all segments, are shown in Figure 7-5. A video of the experiment can be found by scanning the QR-code or following the url¹.



In Figure 7-3, the first two segments of the driven trajectory are shown. The controller is able to track the path accurately, with a lateral error between -0.05 m and 0.08 m. Some deviations, however, can be observed. After every corner, the DSV ends up on the inside of the curve. At the end of the straight parts at the top of the two ovals, again a deviation from the path can be observed. In both situations, the feedforward steering angle is increasing, as result of the increasing curvature. Due to model mismatches, however, the feedforward steering angle is not entirely accurate (in this situation it is too big). The feedback controller resolves the resulting path-tracking errors, but because of the latency of the position estimate, it is too late. Furthermore, significant oscillations can be observed in the course error and steering angle. These oscillations, however, occur due to the play in the steering system and the accuracy of the steering servo. These two factors make it difficult to drive in a straight line, even if the DSV is operated manually with the remote. The latency of the Lidar, though, increases the size of the oscillations.

In Figure 7-4 the next three segments of the driven trajectory are shown. In all three segments, significant path-tracking errors can be observed. These, however, are not caused by the controller. The large deviation in segment three (purple) is caused by an estimation error of the SLAM software, resulting in a large jump in position. This is also clearly visible in the lateral error at $t = 28$ s. In segment four (green) significant corner-cutting can be observed. This is caused by a faulty orientation estimation. The black lines in the plot indicate the estimated orientation of the vehicle centreline. As can be seen, the centrelines first are approximately aligned with the driven trajectory. After some time, however, the centrelines remain pointed towards the path, but the DSV is not moving in that direction. The controller, therefore, thinks the DSV is moving towards the path and changes the steering angle accordingly. But, since the vehicle is not moving towards the path, this results in corner-cutting. Analysis of the orientation measurement of the Lidar and IMU shows the IMU is to

¹The video of the typical cornering experiment with Lidar can be found at: https://youtu.be/a0ouZ__qBTE

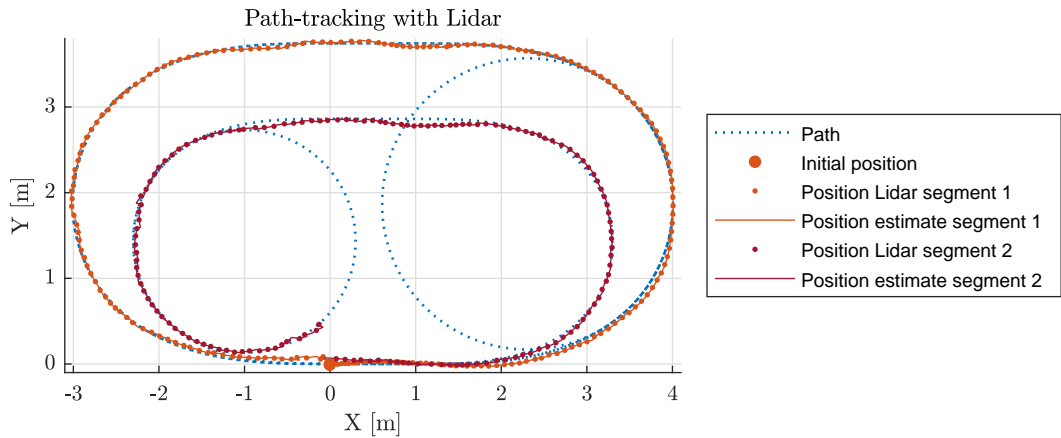


Figure 7-3: Trajectory of the implemented typical cornering controller, segment 1 and 2

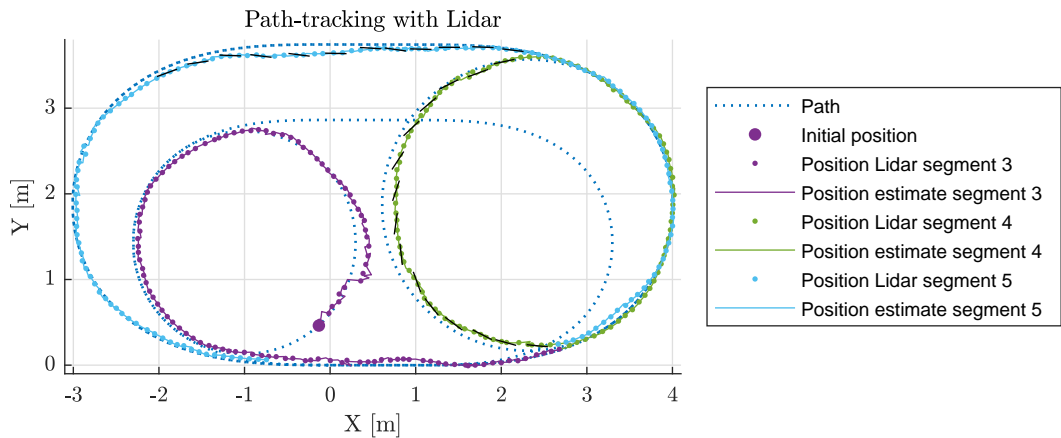


Figure 7-4: Trajectory of the implemented typical cornering controller, segment 3, 4 and 5

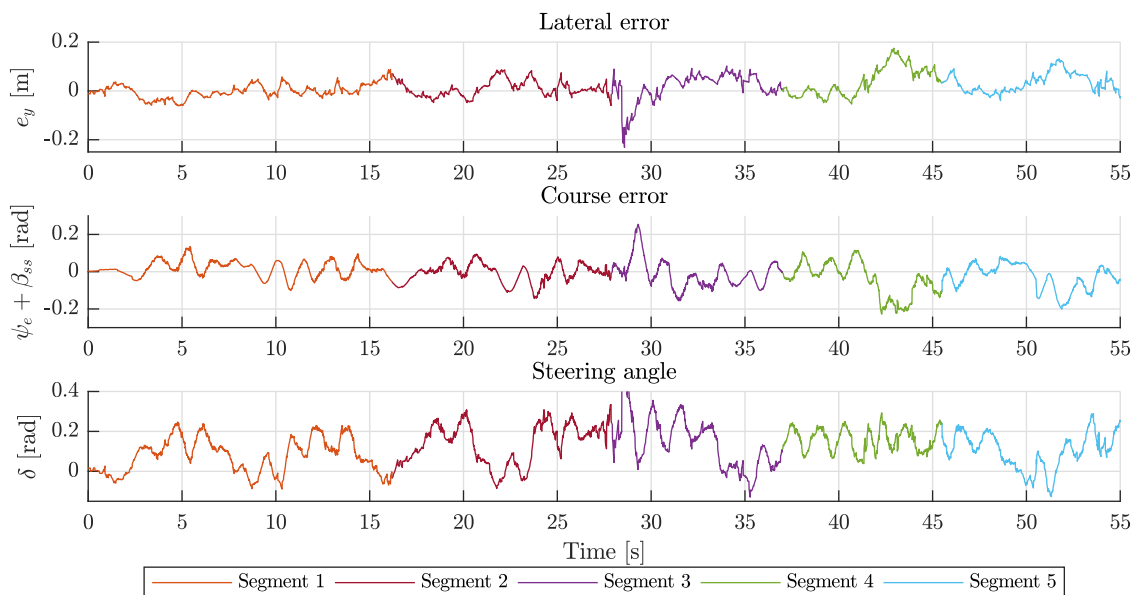


Figure 7-5: Path-tracking errors of the implemented typical cornering controller with Lidar

blame for the faulty measurement. A comparable measurement error causes the deviation in segment five.

In segment three, a large jump in position estimate by the SLAM software is shown. At other regions of the path, however, more inaccuracies can be observed. Around the origin of the two plots, small jumps in the estimated positions can be observed. Furthermore, the distance between the estimated positions varies significantly. The same can be observed for the two corners on the left side of the plots. These measurement inaccuracies are probably caused by the objects placed around the testing area. Around the testing area, multiple pieces of white cardboard are placed for the Lidar to detect. These pieces of cardboard, however, do not form an enclosed area. The Lidar is disturbed by other objects, which have a dark or shiny surface.

7-3-2 Typical cornering with Motion capture system

Using the position estimation based on the Lidar measurements showed mediocre path-tracking performance, mostly caused by the measurement errors. As an alternative for the Lidar, therefore, a motion capture system is used. This system provides an accurate position and orientation estimate at 120 Hz at very high accuracy ($< 1 \text{ mm}$). The shape of the path is equal to the one used in the previous section, except for the size of the outer oval. Since the floor area where the motion capture system can measure the pose accurately is limited, the outer oval is decreased in height from 3.8 m to 3.5 m.

The driven trajectory is shown in Figure 7-6, and the path-tracking errors are shown in Figure 7-7. The same segments are used as in the previous section. However, segment five is not shown in the plots, since in this case, it is equal to the first segment. A video of the experiment can be found by scanning the QR-code or following the url².



The path-tracking performance with the motion capture system is significantly better, compared to the results in the previous section. In general, the lateral error remains between 0.02 m and -0.04 m . However, at multiple time instants, measurement errors in the course error can be observed. These measurement errors occur at the left hand of the trajectory plot. In this region, the vehicle drives on the limit of the detectable range of the motion capture system, resulting in a faulty orientation measurement. Moreover, the same yaw oscillations as in the previous section can be observed. The size of the oscillations, though, is much smaller, resulting from the smaller latency in the position estimation.

²A video of the typical cornering experiment with Mo-cap can be found at: <https://youtu.be/aU6xPavFe4Q>

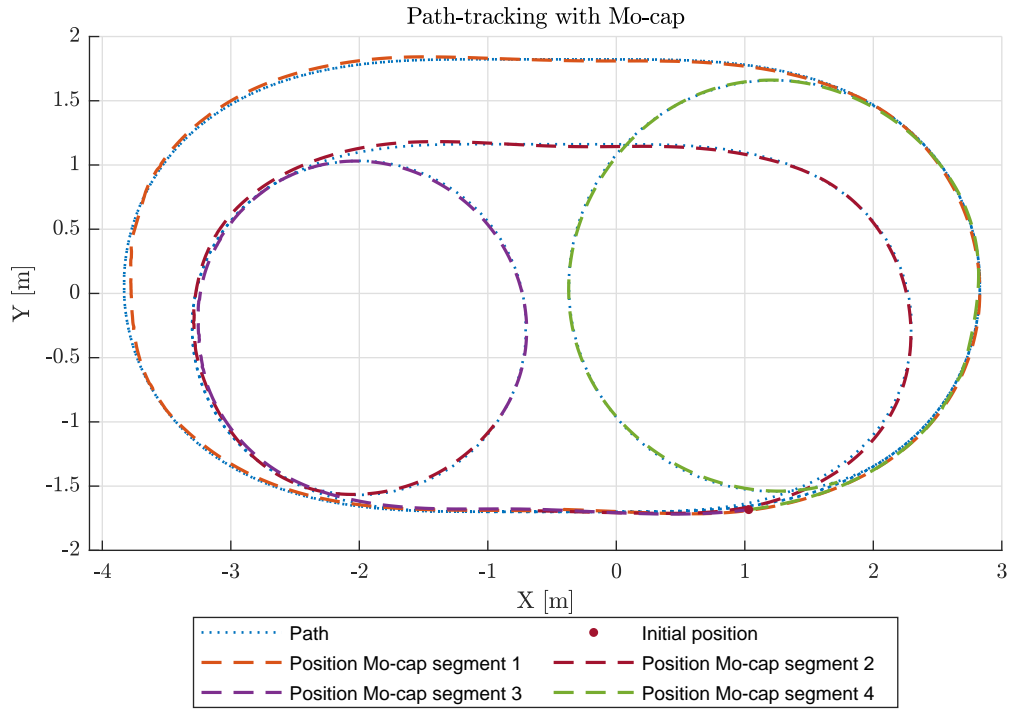


Figure 7-6: Trajectory of the implemented typical cornering controller with Motion capture system

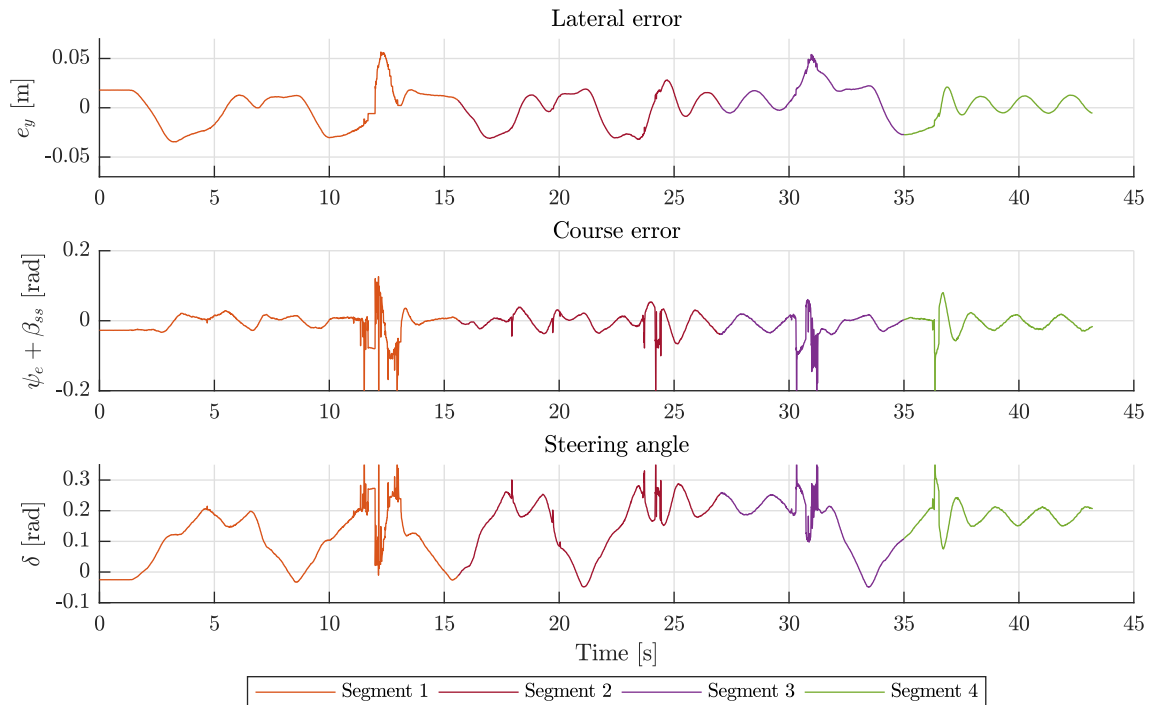


Figure 7-7: Path-tracking errors of the implemented typical cornering controller with Motion capture system

7-3-3 Drifting

The final step of this research is the implementation of the drift controller in the DSV. First, the transition from typical cornering conditions to drifting is tested. To simplify tuning, a static longitudinal wheel slip is used instead of the feedback longitudinal wheel slip from Equation 6-1. A pulse on the desired longitudinal wheel slip, with magnitude $\lambda_{des,t}$ and duration t_t , is used to saturate the rear tyres and induce the drift. Next, the full drift controller is implemented. After saturation of the rear tyres, the controller switches to drift mode. Since the vehicle is driven indoors in an area surrounded by walls, a low velocity is desired, and the size of the path is limited. The chosen path is circular with a radius of 1.40 m. Initially, the reference velocity is chosen to be 1.5 m/s. During testing, however, a slightly higher velocity showed better results. The final reference states are shown in Table 7-3. The yaw rate is based on the velocity and curvature, and the body sideslip angle is obtained from the corresponding drift equilibrium. Finally, some adjustments to the controller gains are made, to improve the performance in this application. The used controller gains are shown in Table 7-4.

Table 7-3: Reference states for implementation of the drift controller

| State | Value |
|---------|------------|
| v | 1.7 m/s |
| r | 1.21 rad/s |
| β | -0.4 rad |

Table 7-4: Controller gains of the implemented drift controller

| Controller gain | Value |
|-------------------|-------|
| t_{la}^d | 1.2 |
| K_β^d | 5.8 |
| K_r^d | 2.8 |
| $K_{v,t}^d$ | 0.4 |
| $K_{\beta,t}^d$ | 3.3 |
| $K_{r,t}^d$ | 0.6 |
| t_t | 0.2s |
| $\lambda_{des,t}$ | 0.35 |

The states, path-tracking errors and control inputs during a drifting manoeuvre with the DSV are shown in Figure 7-8. The driven trajectory of the vehicle for the same time range is shown in Figure 7-9. A video of the experiment can be found by scanning the QR-code on the right or following the url³.



Initially, the vehicle drives in typical cornering conditions. After a few seconds, the controller saturates the rear tyres and induces the drift. The controller is able to maintain the drift for at least 30 seconds, with the body sideslip angle close to its reference value. The lateral and course error show large oscillations with a period of approximately 5 seconds. An explanation for these oscillations can be found in the trajectory plot. Initially, the vehicle drives in typical cornering conditions towards the path. When the drift is induced, the vehicle first moves away from the path. It then crosses the path to, eventually, settle at a somewhat constant circular motion. The radius of this circle, however, is slightly larger than the radius of the path and it is translated a few centimetres in the positive Y direction. The latter results in the oscillations in the lateral and course error and the period of approximately 5 seconds originates from the time it takes for the vehicle to make one circumference. So even though

³A video of the implemented drift controller in the DSV can be found at: <https://youtu.be/VWgdd5jgyuk>

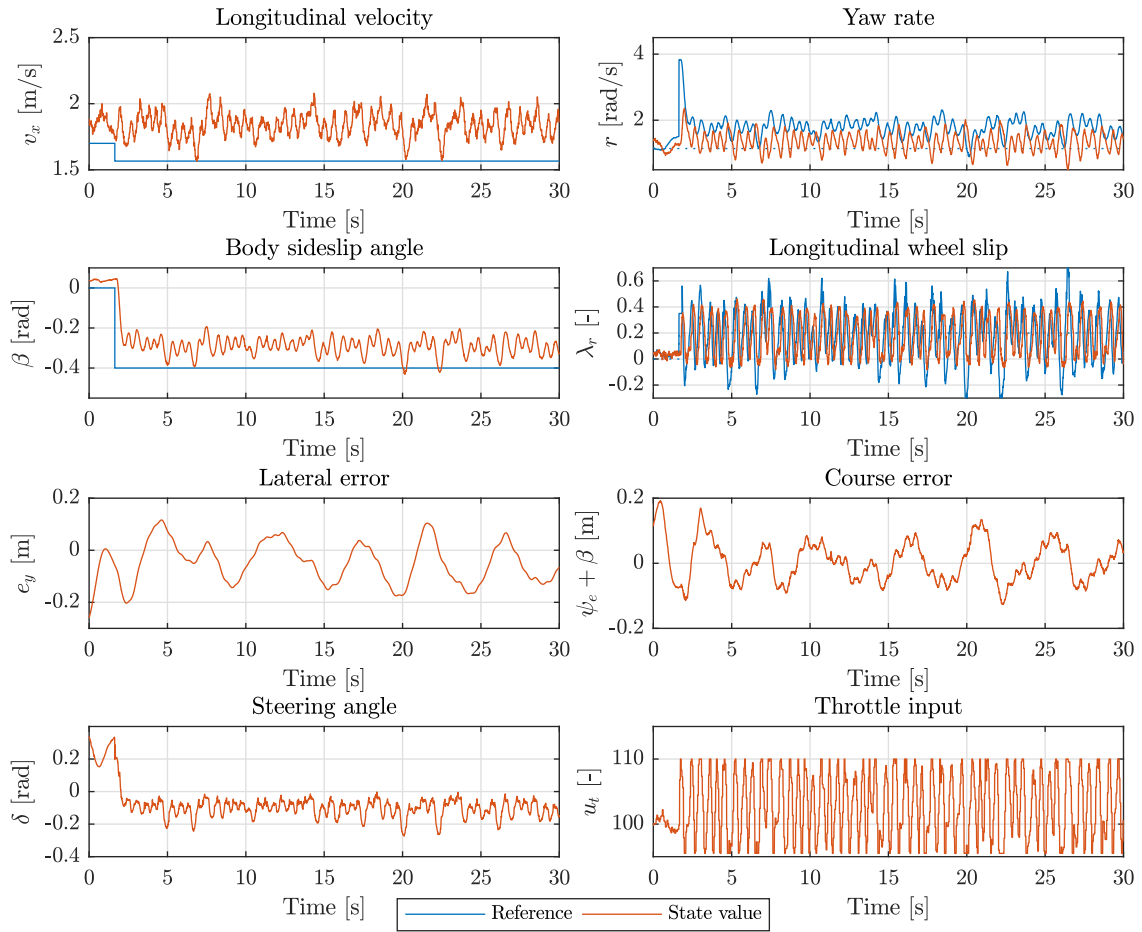


Figure 7-8: States, path-tracking errors and control inputs during a drifting manoeuvre with the DSV

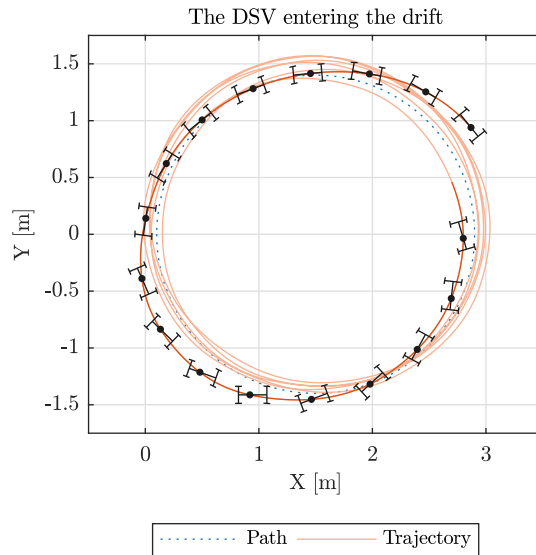


Figure 7-9: Driven trajectory during a drifting manoeuvre with the DSV

the course and lateral error show large variations, a somewhat constant circular motion can be observed.

Additionally, higher frequency oscillations in the states can be observed. These oscillations result from the various lags in the system. Oscillations in longitudinal wheel slip result in oscillations in yaw rate, velocity and body sideslip angle. The desired longitudinal wheel slip is based on all three and will, therefore, inherit the oscillations. Between the desired longitudinal wheel slip and the measured longitudinal wheel slip, a lag of approximately 0.1 seconds can be observed. Because of this lag, the throttle input changes too late, resulting in further oscillations.

To summarise, both the typical cornering and drift controller are successfully implemented in the DSV. In typical cornering conditions the DSV can track the desired path accurately, and, on command, the vehicle can enter and sustain a drift, while remaining close to the path. However, further tuning is required to increase the performance of the drift controller and to reduce the oscillations in rear longitudinal wheel slip.

Chapter 8

Conclusions and recommendations

In this chapter, first, conclusions are drawn based on the performed research. Subsequently, recommendations are given for future research.

8-1 Conclusions

Current vehicles have many safety systems installed. Systems like Electronic Stability Control are aimed to improve the safety of the driver by preventing the vehicle from entering unstable behaviour. However, controlling the vehicle in the unstable region could potentially improve safety even more. The main objective of this research is to design a lateral controller that can follow a feasible path in both typical cornering and unstable high body sideslip conditions.

Performing tests with an actual vehicle can run into high costs since it requires a test track, vehicle and driver. To reduce the costs, an experimental platform in the form of a 1/10 scale Radio Controlled (RC) car is used in this research; the Delft Scaled Vehicle (DSV). This vehicle has onboard sensors to obtain the required measurements. Based on the measurements of various driving scenarios, a nonlinear vehicle model is identified. This model is used to develop and test the controller.

As a basis for the controller, an existing drift controller based on the equations of motion of a two degrees of freedom vehicle model is used. The controller determines a combination of front and rear lateral tyre forces to keep the vehicle at an equilibrium body sideslip angle and yaw rate. The main contribution of this research is the addition of path-tracking capabilities to the controller. This is achieved by replacing the static yaw rate reference by a yaw rate based on feedforward and feedback of the path curvature and path-tracking errors. The reference body sideslip angle is obtained from the drift equilibrium corresponding to the current path curvature.

A sensitivity analysis shows that the controller can stabilise the drifting vehicle around the path for various curvatures and velocities. Additionally, it showed the controller can stabilise the vehicle from significant state perturbations. Furthermore, the controller is able to enter a

drift from typical cornering conditions. By steering into the corner, before saturating the rear tyres, the deviation from the path during the transition can be minimised. Implementation of the typical cornering controller in the DSV showed the controller is able to track a desired trajectory accurately. Furthermore, the drift controller achieved to bring the DSV into a drift and sustain it, while remaining close to the path.

As a result, the main objective of this master thesis has been accomplished. A lateral controller is developed that is able to follow a feasible path in both typical cornering and unstable high body sideslip conditions.

8-2 Recommendations for future work

The controller approach proposed in this thesis is shown to be a simple and insightful method of path-tracking beyond the limits of stable handling. However, to improve the controller performance and to make the controller applicable in a larger range of conditions, additional research is required. This section elaborates on that by giving recommendations for future work.

The controller minimises the body sideslip error and the path-tracking errors via the yaw rate. Since it is important that the vehicle maintains the drift, the body sideslip angle has a much larger influence on the desired yaw rate than the path-tracking errors do. This, however, also means that selection of the right reference body sideslip angle is of high importance. In this controller, the reference body sideslip angle is determined by finding the drift equilibrium corresponding to the current path curvature. Due to model mismatches, this equilibrium body sideslip angle does not necessarily correspond to the same curvature for the actual vehicle (model). It is, therefore, recommended to find an alternative reference body sideslip angle or add additional feedback to resolve the model mismatches.

Moreover, the controller uses static feedback gains to determine the required control inputs. This means that the controller is optimised for a specific equilibrium. This is mainly the case for the desired wheel slip input of the drift controller (Equation 5-41). The equation is based on errors and feedback gains only and does not take vehicle dynamics into account. To optimise the performance around other equilibria, the controller has to be re-tuned. By selecting the appropriate controller gains during operation (e.g. gain scheduling), the performance of the controller in a larger range of conditions can be improved.

The drift controller consists of two controller modes to find the separate tyre forces from the controller equation (Equation 5-18); the steering mode and the throttle mode. Initially, the steering mode is used, but when the front tyre is saturated, the controller switches to throttle mode. This coordination scheme, however, only takes the yaw and sideslip dynamics into account, not path-tracking objective. Decreasing a yaw rate, for example, can be achieved by counter-steering or decreasing the rear longitudinal wheel slip. These actions, though, affect the course of the vehicle differently. Taking these effects into account in the determination of the separate tyre forces, could probably increase the path-tracking capabilities.

To induce a drift, the rear tyres need to be saturated while cornering. This can be done by increasing the throttle input or braking the rear wheels. In this research, the tyres are saturated by increasing the rear longitudinal wheel slip. This, however, also results in a

significant increase in longitudinal velocity. It is, therefore, recommended to research the effect of using a braking action to induce the drift.

The vehicle model of the DSV is identified from measurement data of various manoeuvres. Since the friction between the surface and the tyres is very low, a small increase in throttle makes the vehicle spin. This made it difficult to capture the nonlinear vehicle behaviour. Increasing the tyre-road friction will make it easier to capture the nonlinear dynamics and improve the vehicle model in that area.

To model the nonlinear tyre behaviour, the modified Dugoff tyre model is used. The modification of this model is based on measurement data of actual tyres. This, however, does not mean the shape of the curves is also applicable to scaled tyres. Since the tyre model has such an important role in the drift controller, a more thorough analysis of the tyre behaviour is recommended.

Appendix A

System identification

In this appendix all manoeuvres used for the system identification are shown.

A-1 Actuator dynamics

A-1-1 Steering dynamics

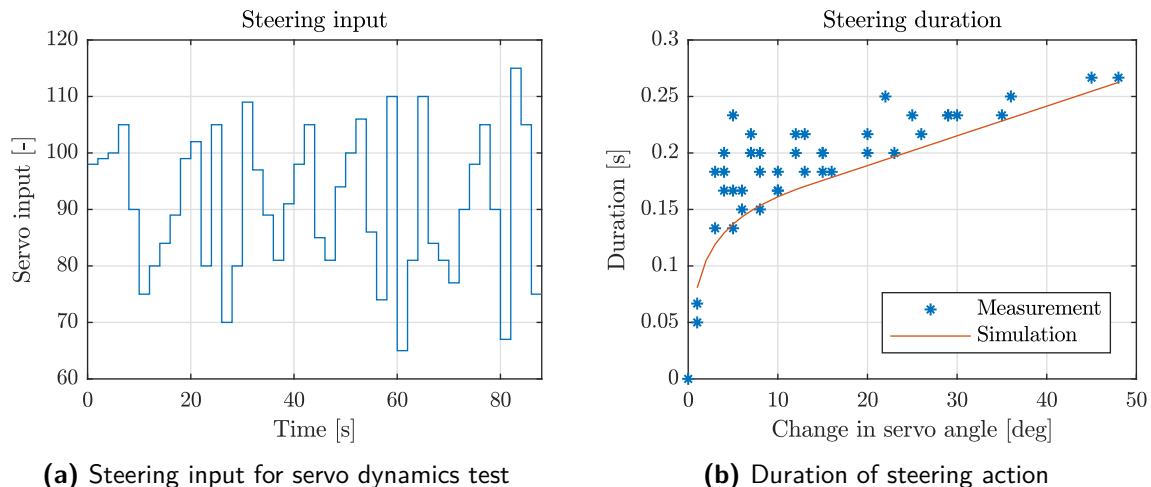


Figure A-1: Steering input and duration of steering action of servo dynamics test

A-1-2 Motor dynamics

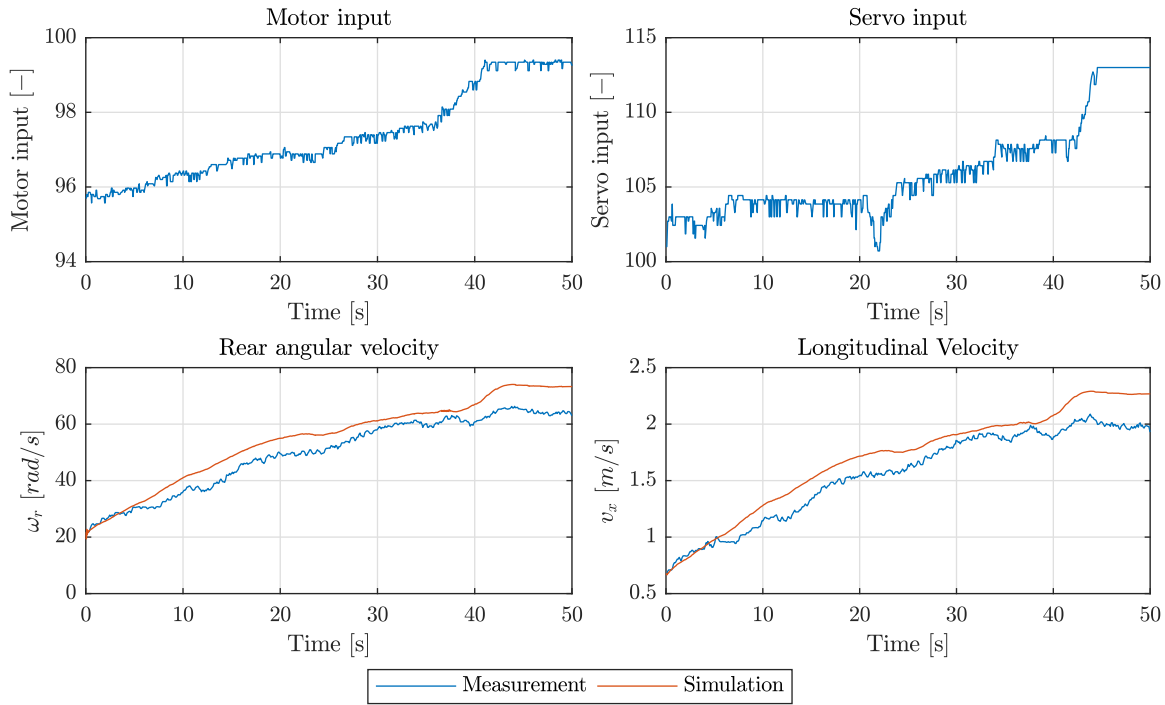


Figure A-2: Manoeuvre for motor parameters estimation: Circular driving with increasing motor input.

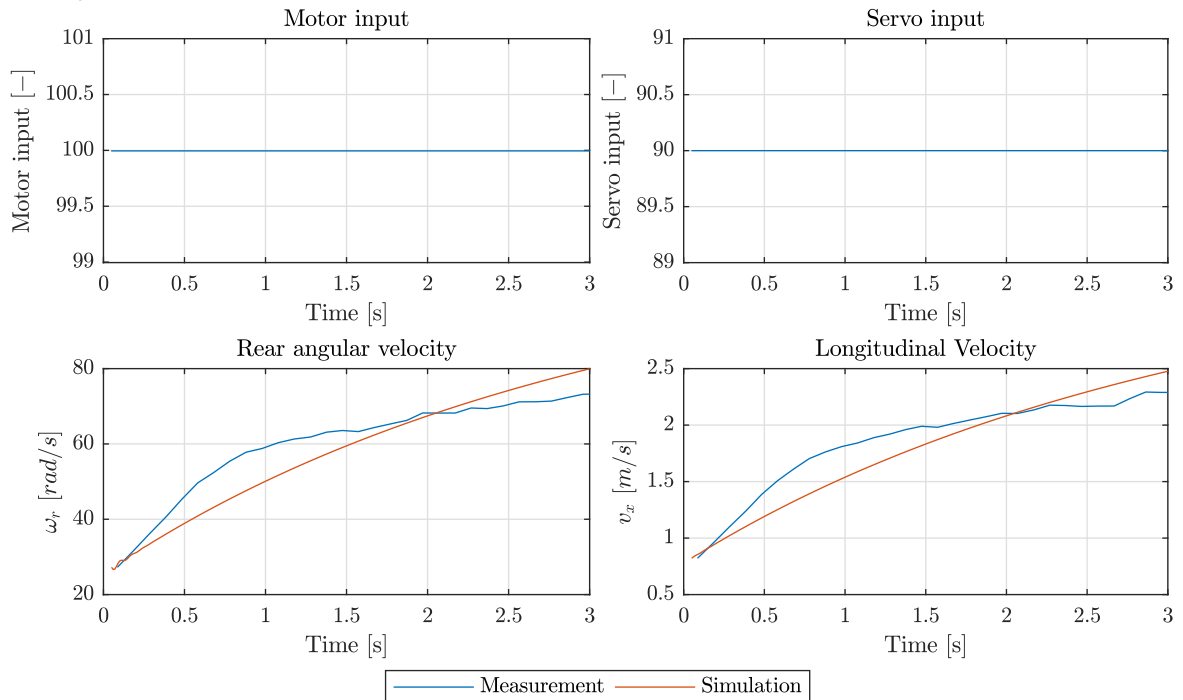


Figure A-3: Manoeuvre for motor parameters estimation: Fixed motor input of 100 from rest.

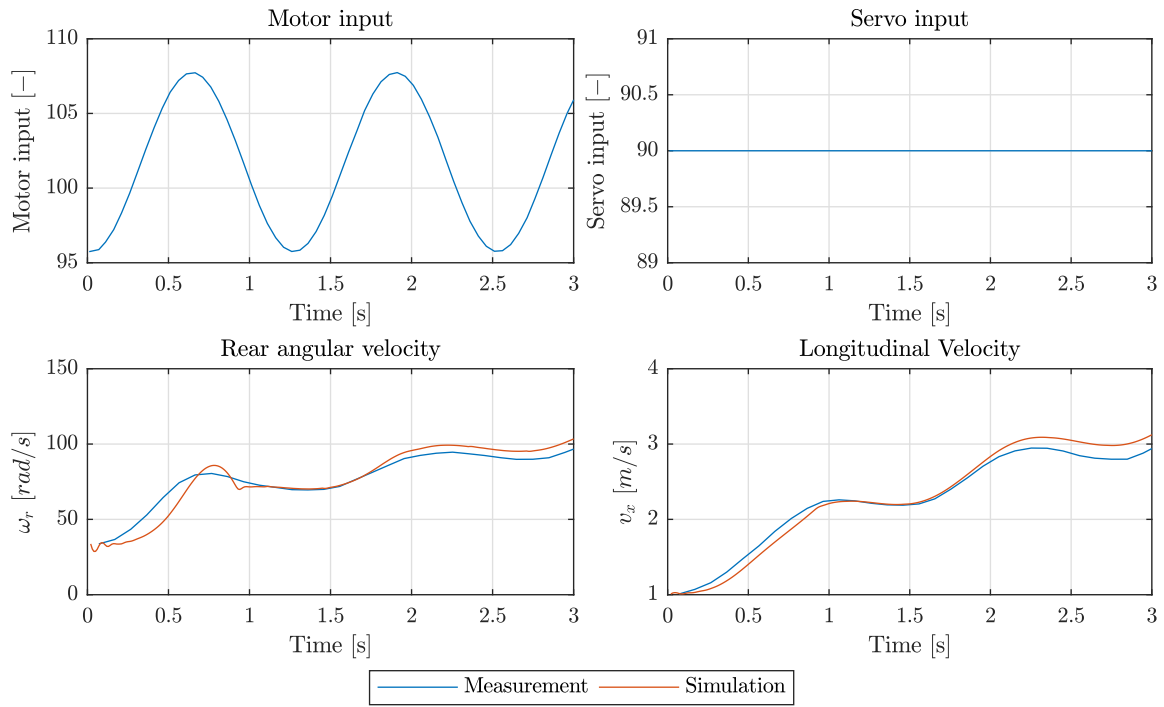


Figure A-4: Manoeuvre for motor parameters estimation: Sine motor input. Frequency: 0.8 Hz, Amplitude: 6, Lowest value: 95.5

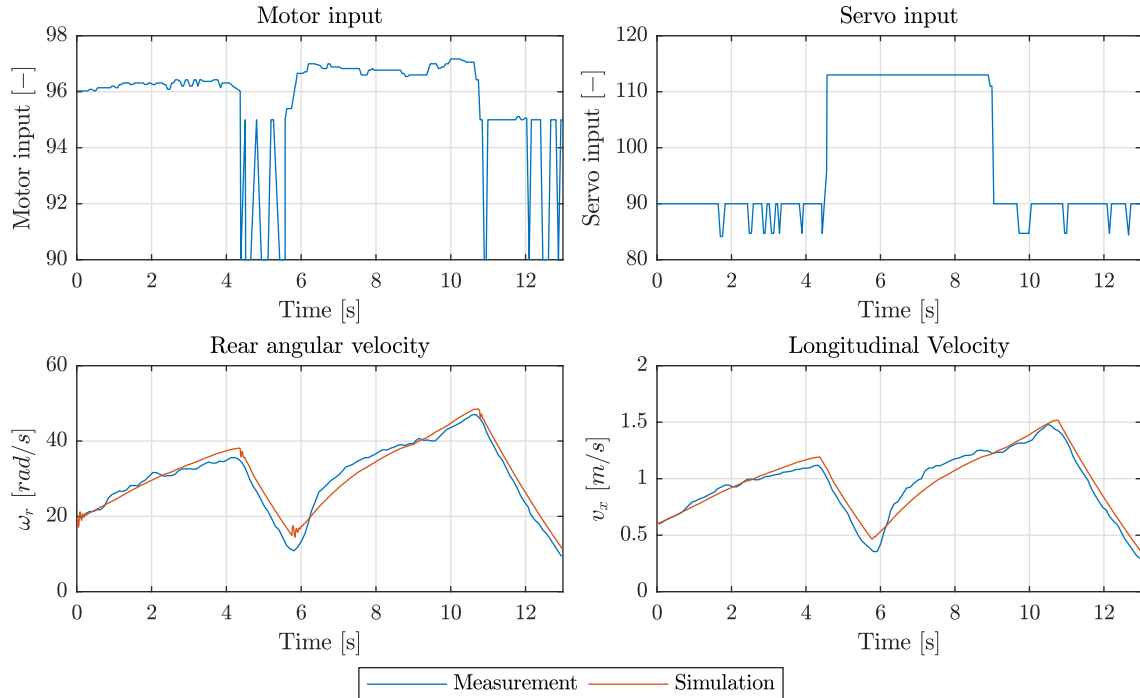


Figure A-5: Manoeuvre for motor parameters estimation: Oval driving with throttle release.

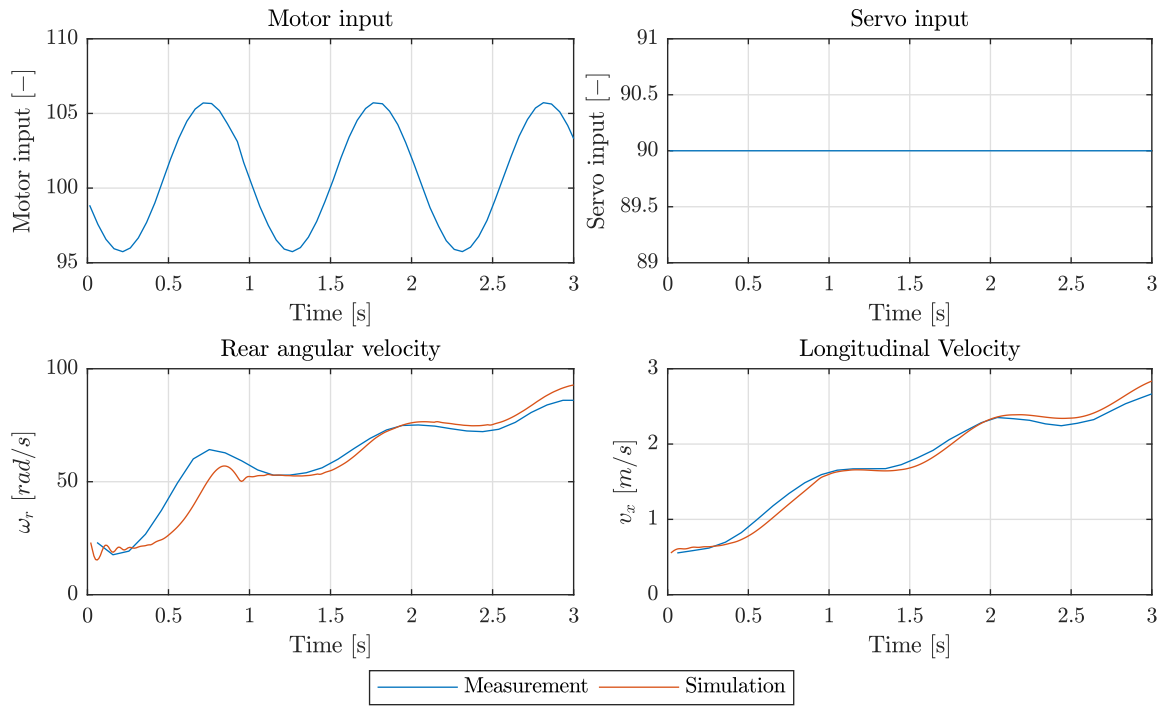


Figure A-6: Manoeuvre for motor parameters estimation: Sine motor input. Frequency: 0.8 Hz, Amplitude: 5, Lowest value: 95.5

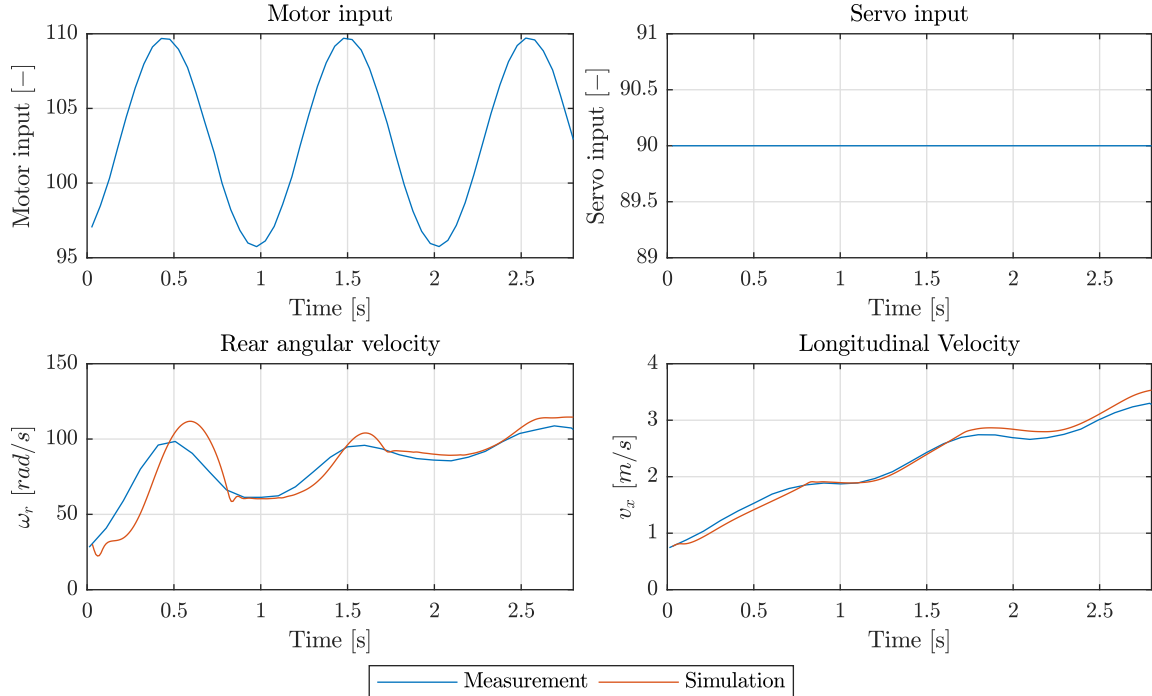


Figure A-7: Manoeuvre for motor parameters estimation: Sine motor input. Frequency: 1 Hz, Amplitude: 7, Lowest value: 95.5

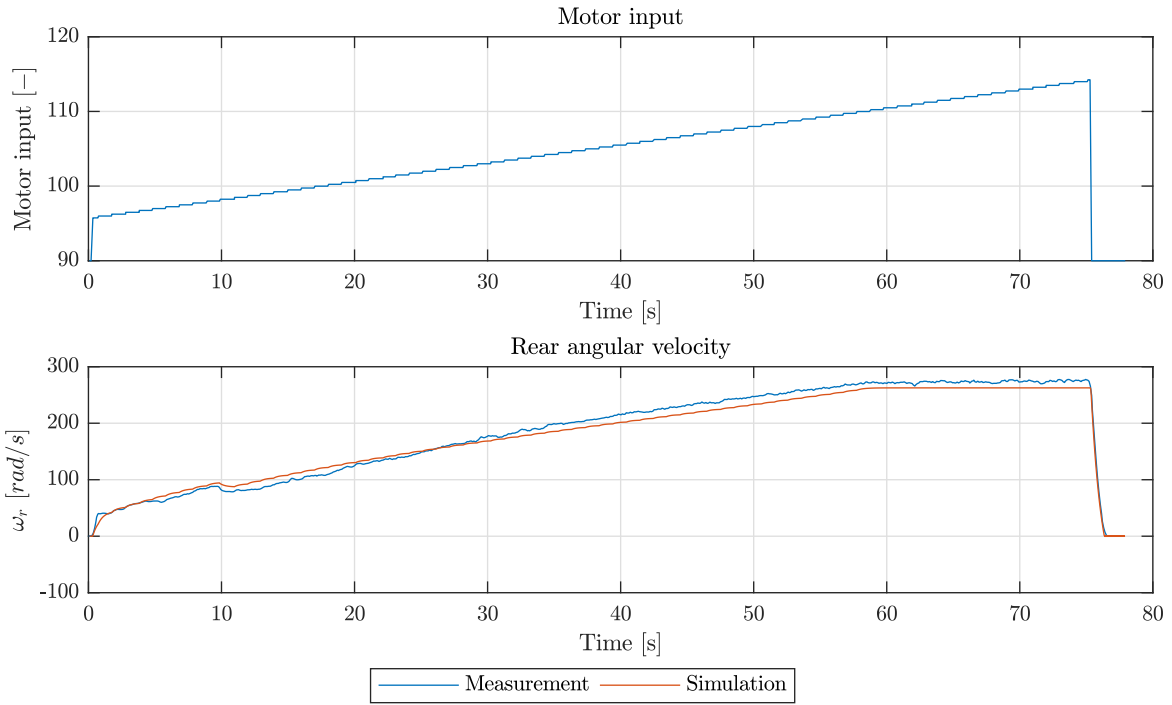


Figure A-8: Manoeuvre for motor parameters estimation: Slowly increasing motor input for free rotating rear wheels.

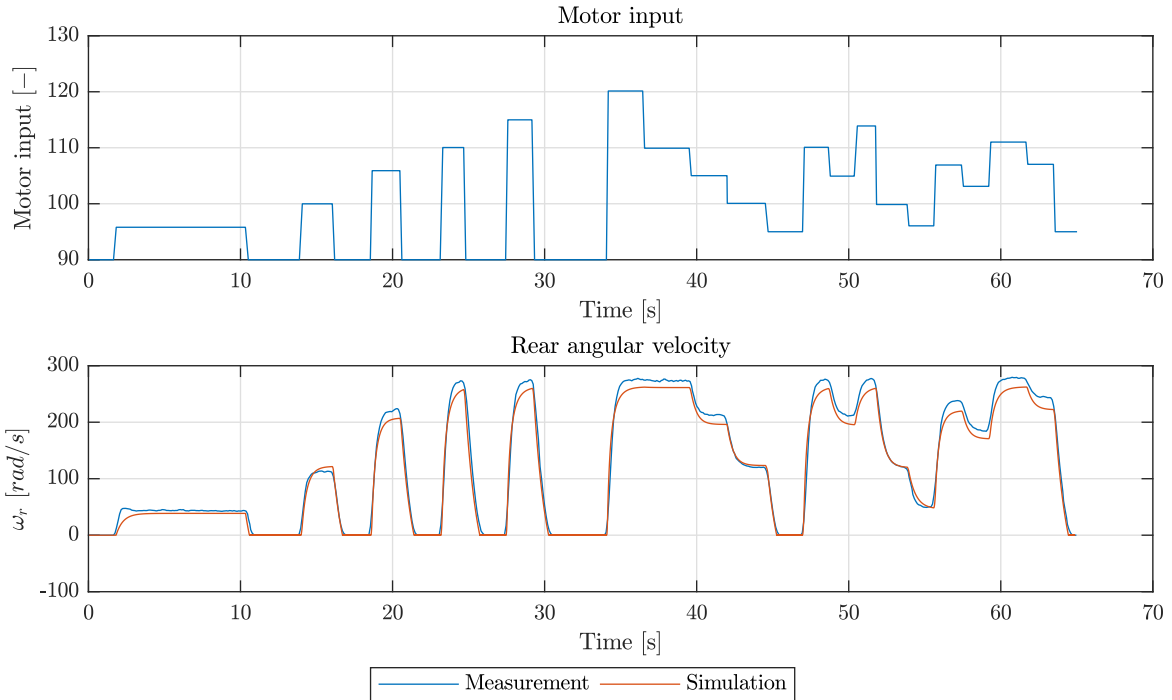


Figure A-9: Manoeuvre for motor parameters estimation: Various step inputs for free rotating wheels.

A-2 Axe and tyre modelling

A-2-1 Axe friction

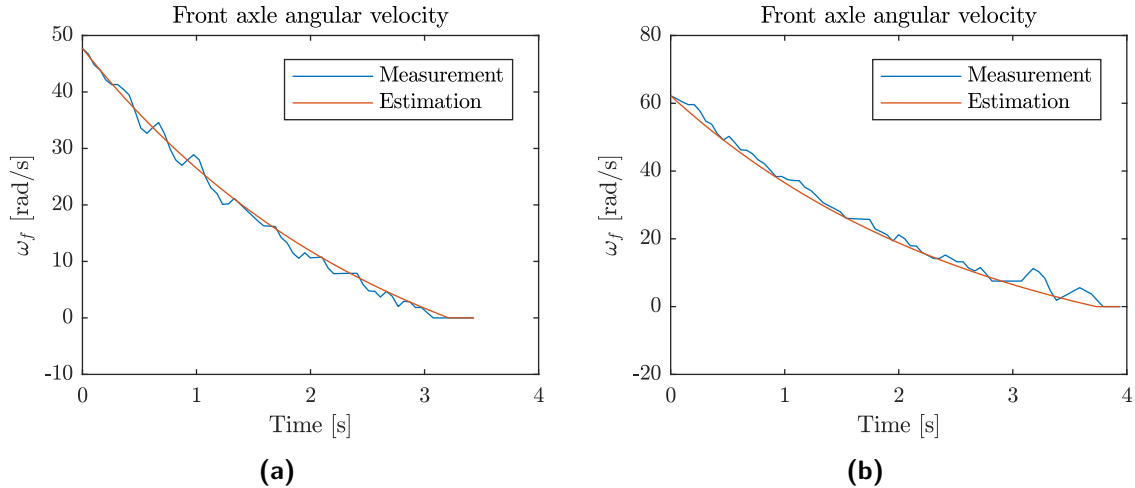


Figure A-10: Measurement data used for axle friction estimation: Decreasing angular velocity of free rotating front axle.

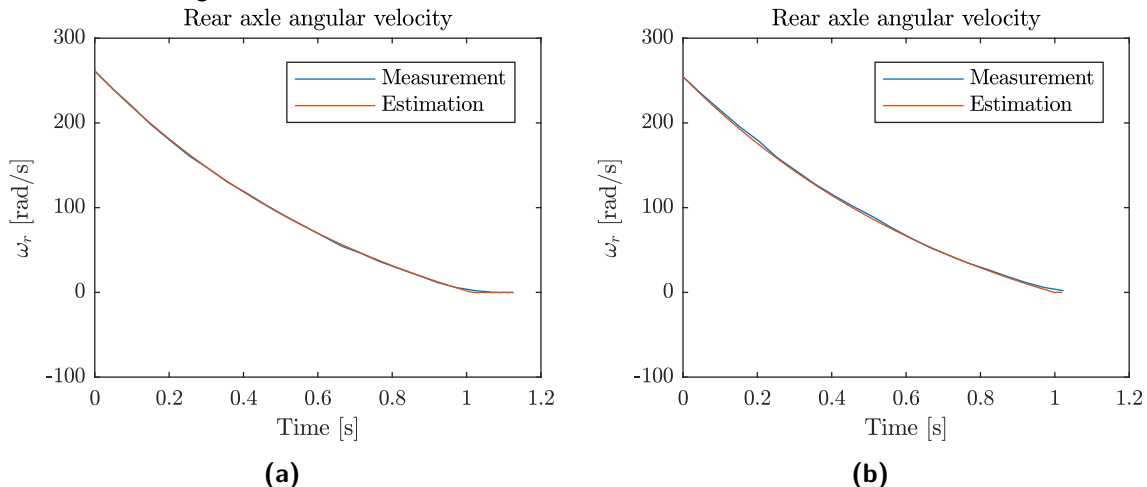


Figure A-11: Measurement data used for axle friction estimation: Decreasing angular velocity of free rotating rear axle.

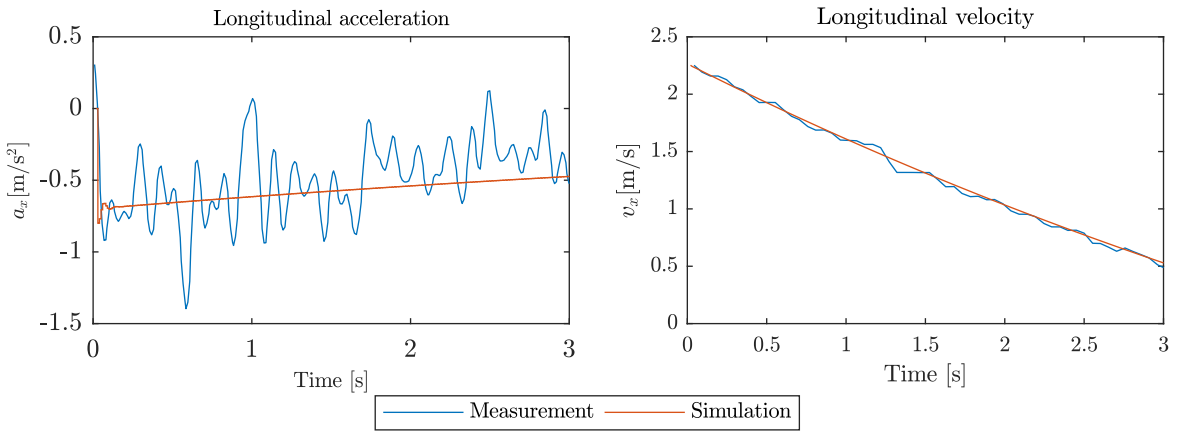


Figure A-12: Measurement data used for axle friction estimation: Decreasing velocity of free rolling vehicle.

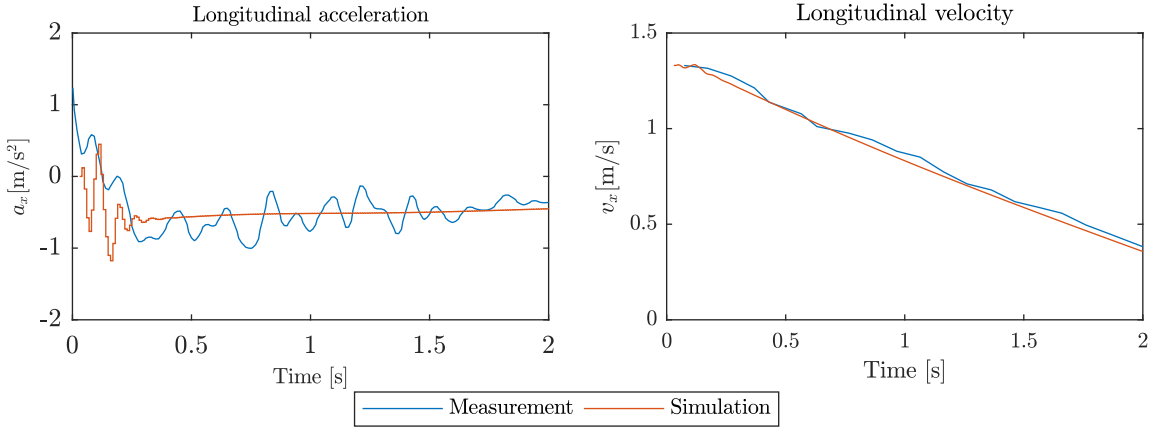


Figure A-13: Measurement data used for axle friction estimation: Decreasing velocity of free rolling vehicle.

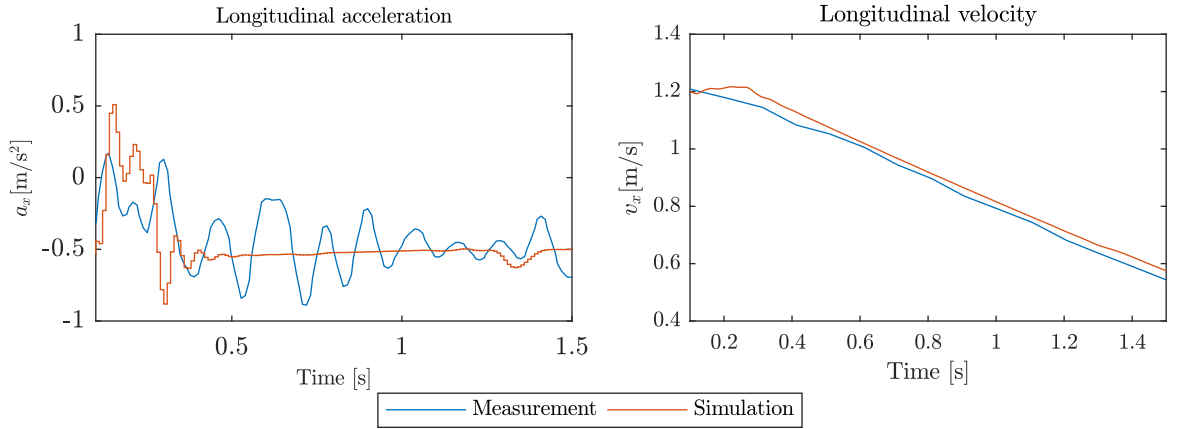


Figure A-14: Measurement data used for axle friction estimation: Decreasing velocity of free rolling vehicle.

A-2-2 Cornering stiffness and yaw moment of inertia

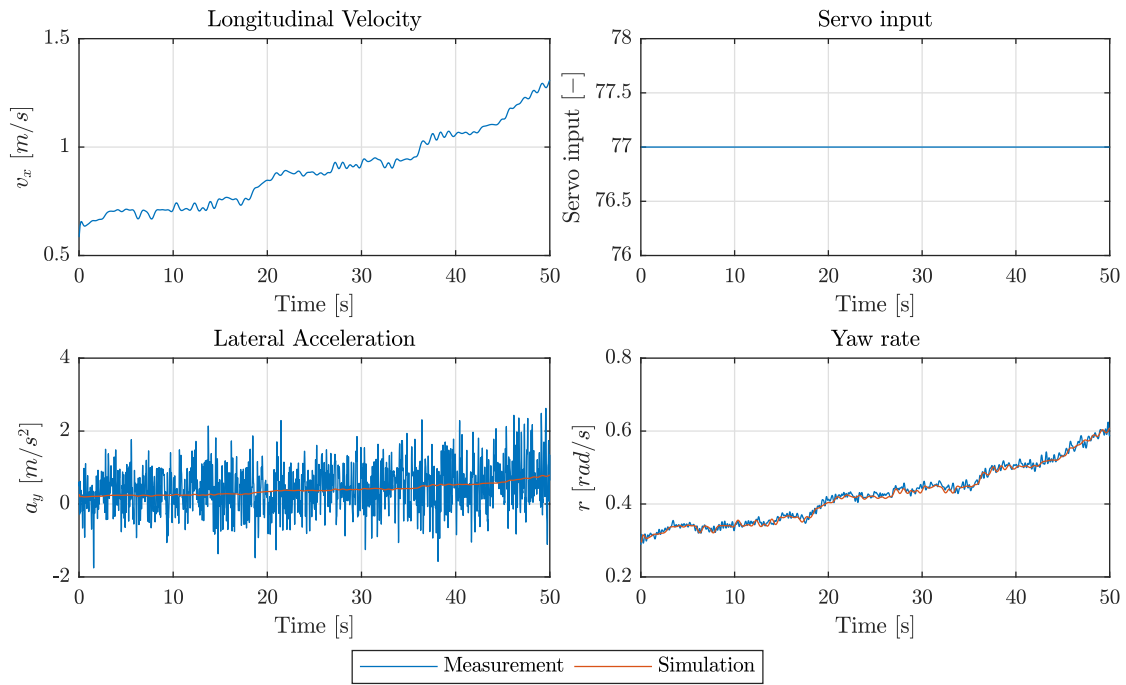


Figure A-15: Manoeuvre used for linear cornering stiffness estimation: Driving with a fixed steering input of 77 and a slowly increasing longitudinal velocity.

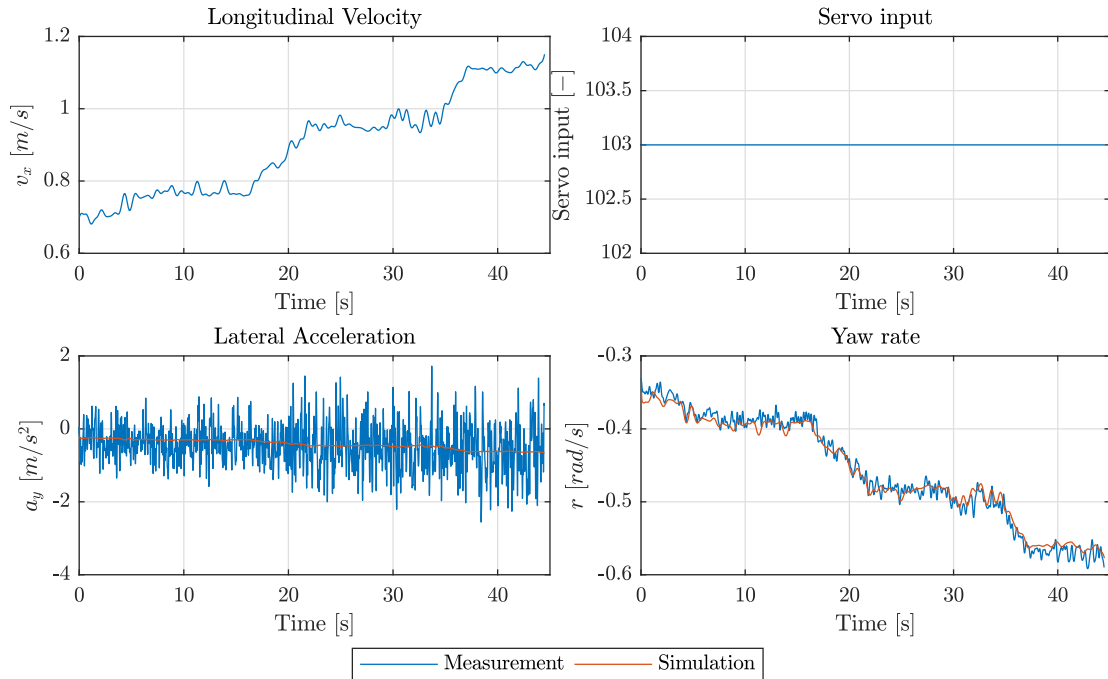


Figure A-16: Manoeuvre used for linear cornering stiffness estimation: Driving with a fixed steering input of 103 and a slowly increasing longitudinal velocity.

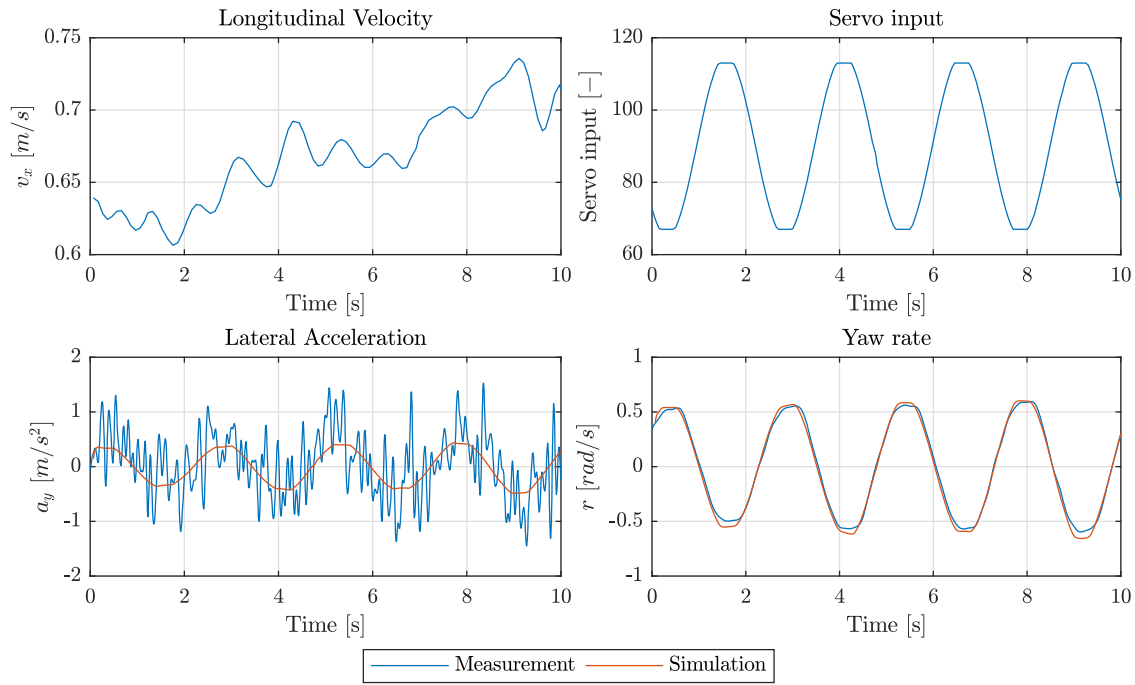


Figure A-17: Manoeuvre used for linear cornering stiffness estimation: Driving at a fixed motor input and a sine steering input. Frequency: 0.4 Hz, Steering input range: 67 – 113

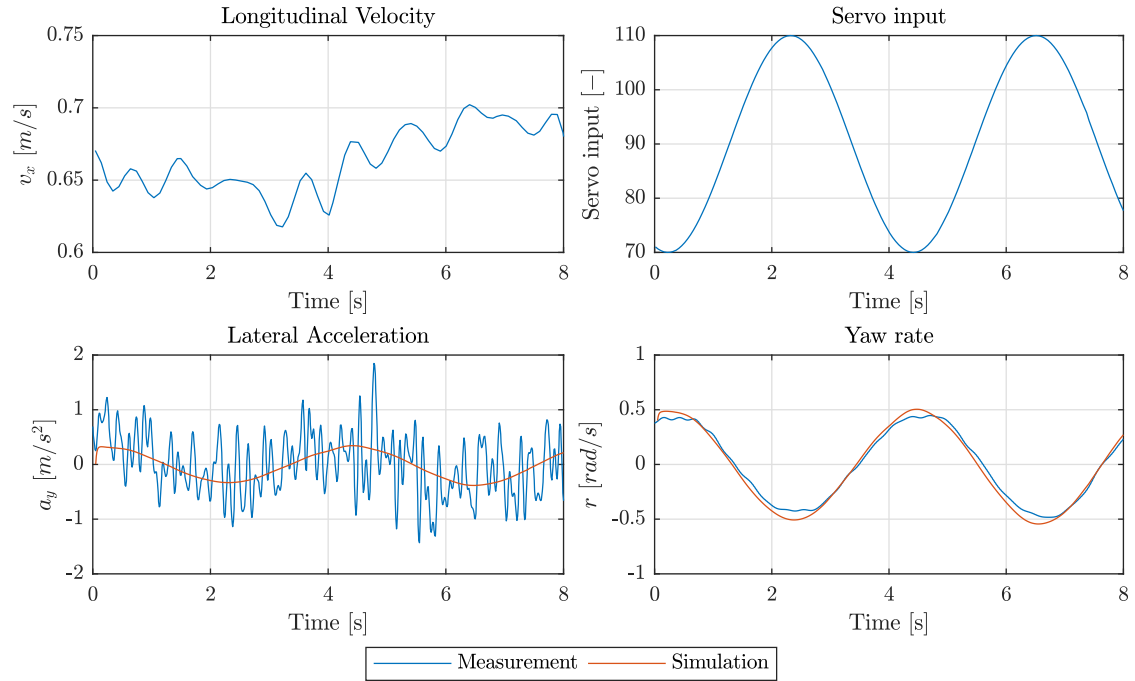


Figure A-18: Manoeuvre used for linear cornering stiffness estimation: Driving at a fixed motor input and a sine steering input. Frequency: 0.24 Hz, Steering input range: 70 – 110

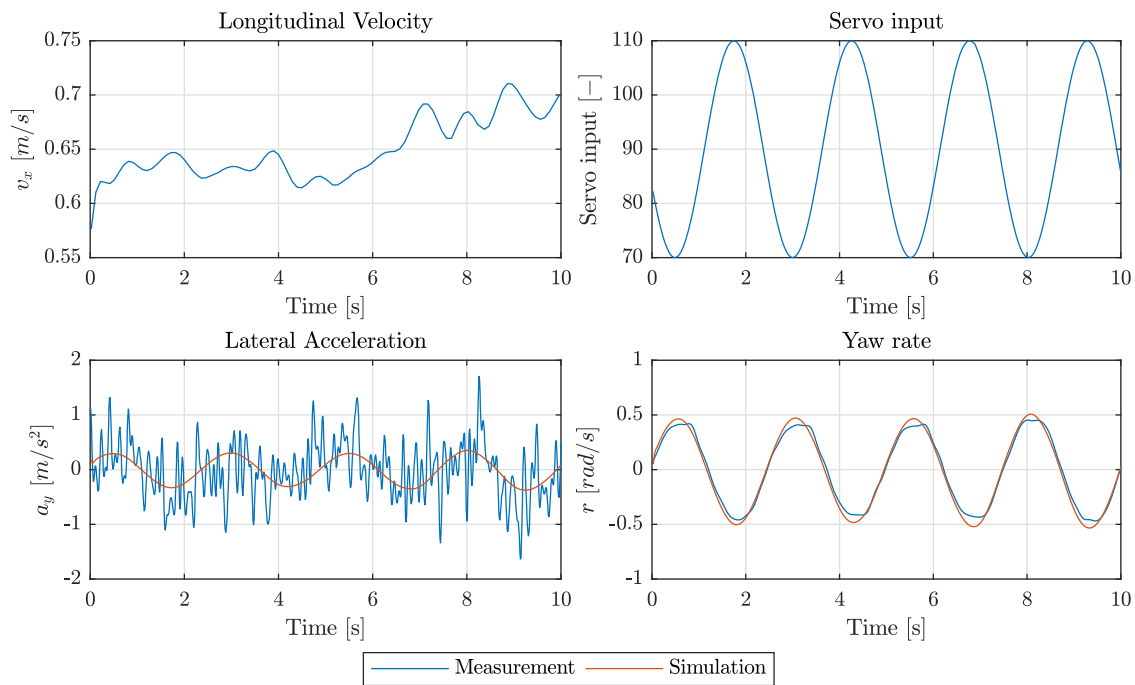


Figure A-19: Manoeuvre used for linear cornering stiffness estimation: Driving at a fixed motor input and a sine steering input. Frequency: 0.4 Hz, Steering input range: 70 – 110

A-2-3 Longitudinal tyre dynamics

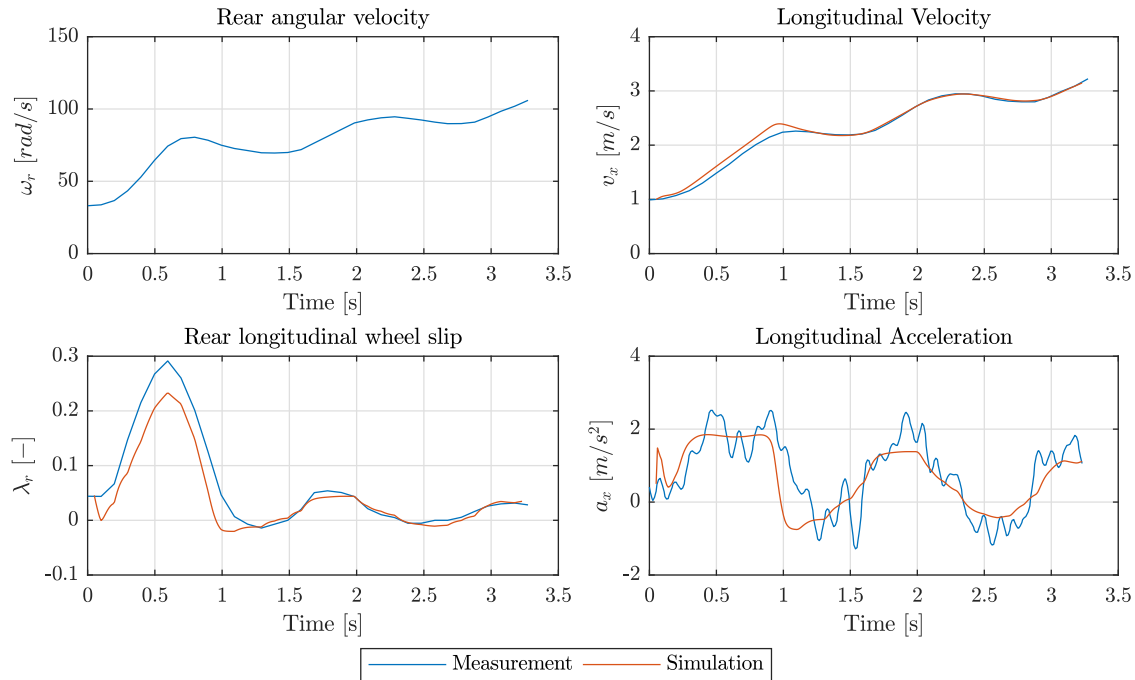


Figure A-20: Manoeuvre used for longitudinal tyre stiffness estimation: Sine motor input. Frequency: 0.8 Hz, Amplitude: 6, Lowest value: 95.5

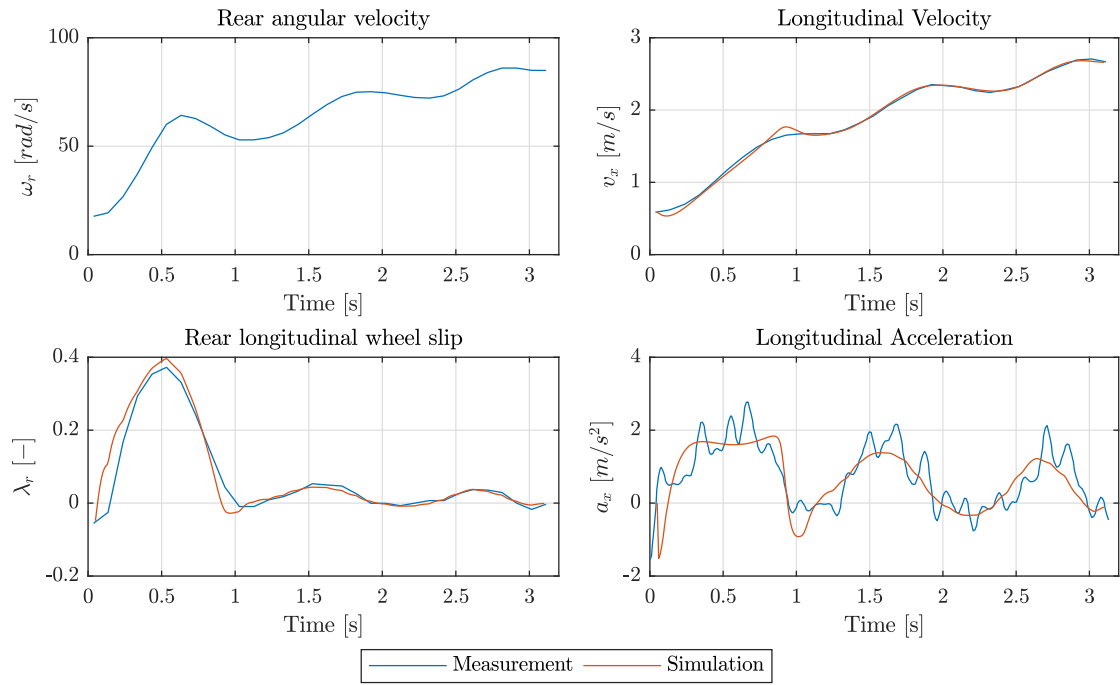


Figure A-21: Manoeuvre used for longitudinal tyre stiffness estimation: Sine motor input. Frequency: 0.95 Hz, Amplitude: 5, Lowest value: 95.5

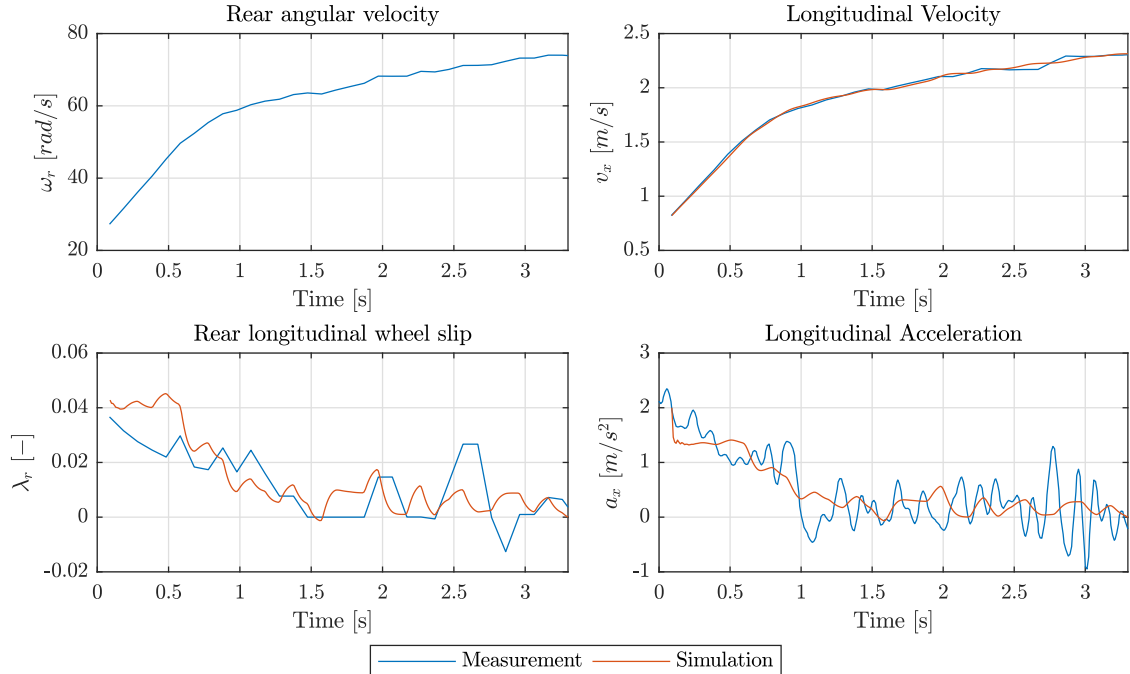


Figure A-22: Manoeuvre used for longitudinal tyre stiffness estimation: Fixed motor input of 100

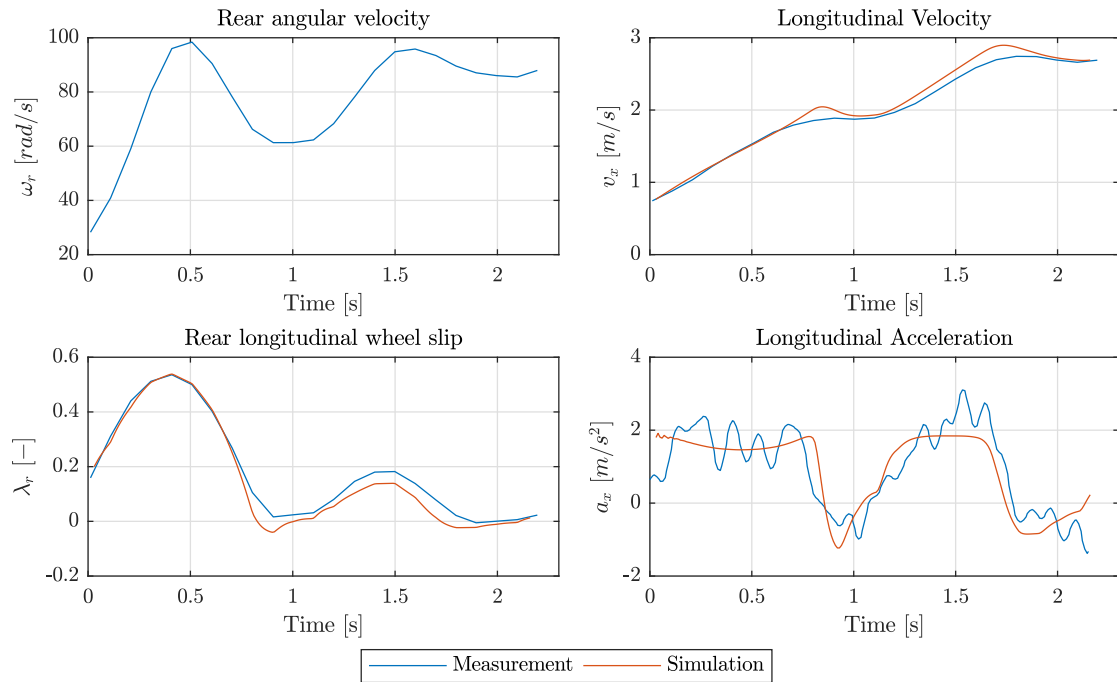


Figure A-23: Manoeuvre used for longitudinal tyre stiffness estimation: Sine motor input. Frequency: 0.95 Hz, Amplitude: 7, Lowest value: 95.5

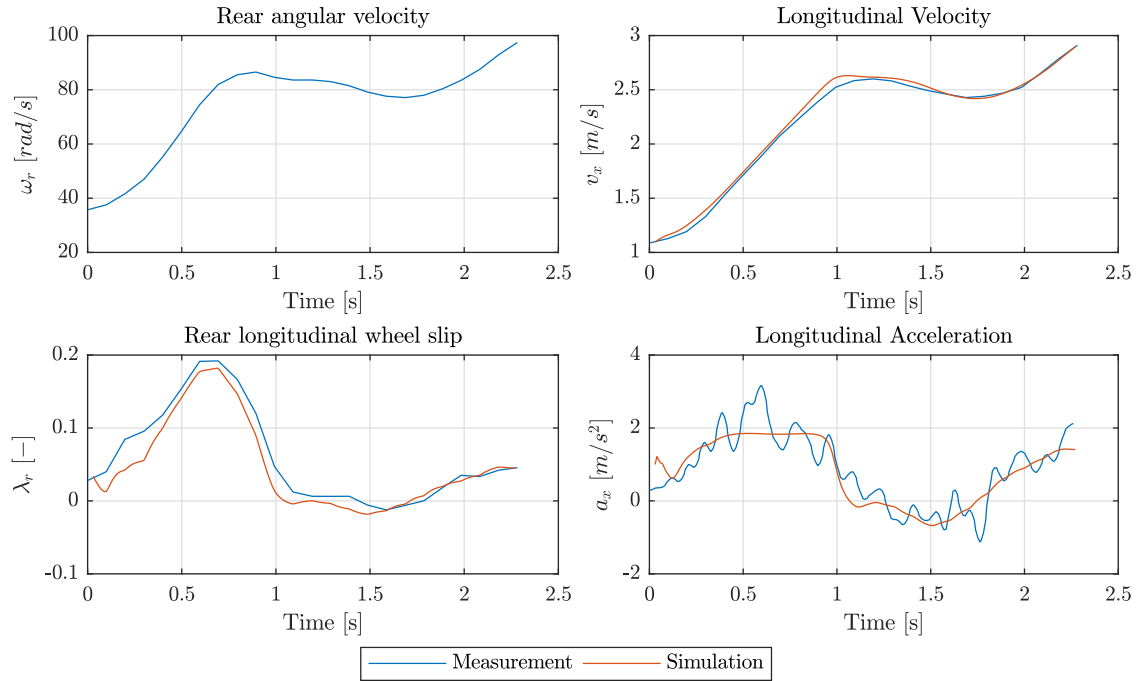


Figure A-24: Manoeuvre used for longitudinal tyre stiffness estimation: Sine motor input. Frequency: 0.6 Hz, Amplitude: 7, Lowest value: 95.5

A-2-4 Combined tyre dynamics

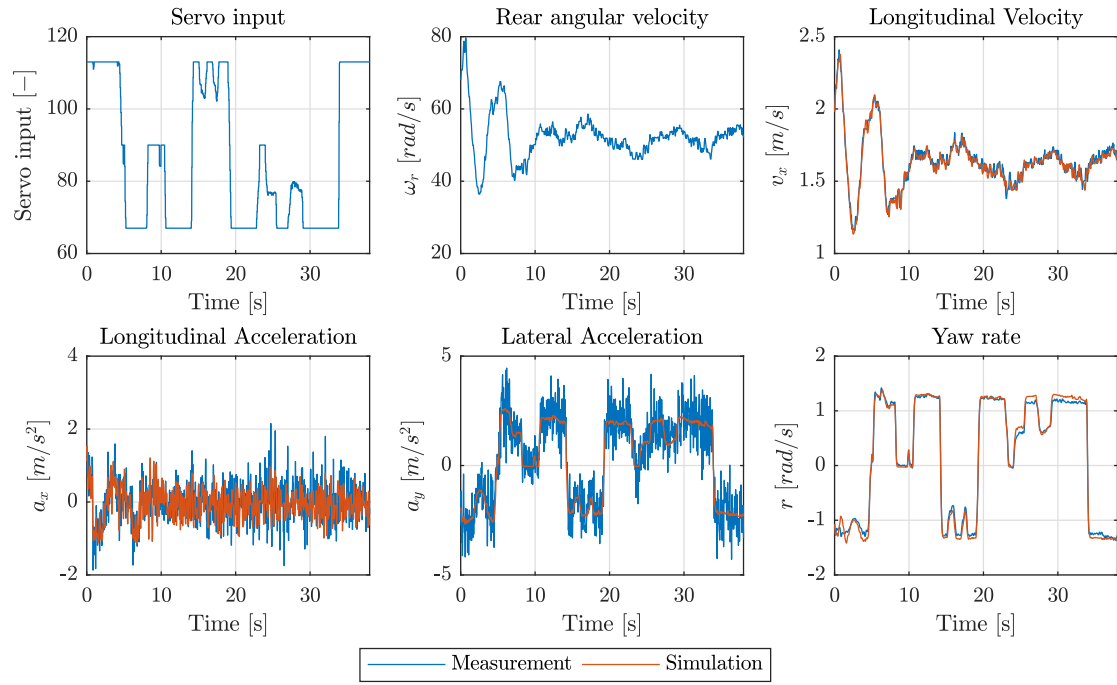


Figure A-25: Manoeuvre used for combined tyre dynamics estimation: Varying motor and steering inputs

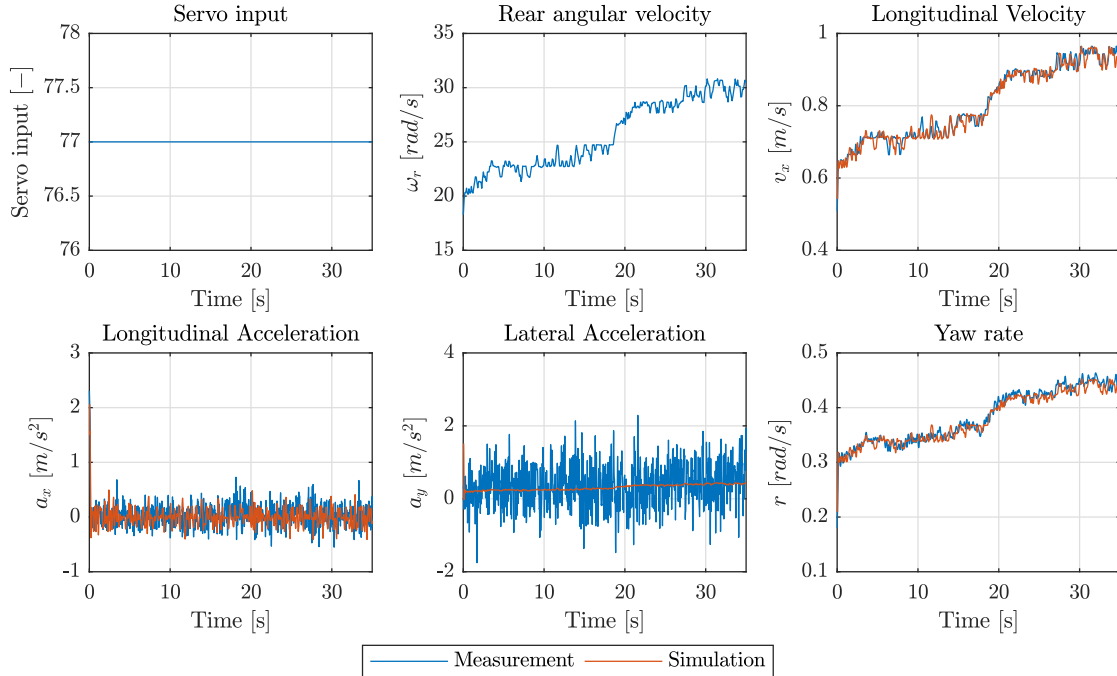


Figure A-26: Manoeuvre used for combined tyre dynamics estimation: Low lateral acceleration, constant steering angle, slowly increasing velocity.

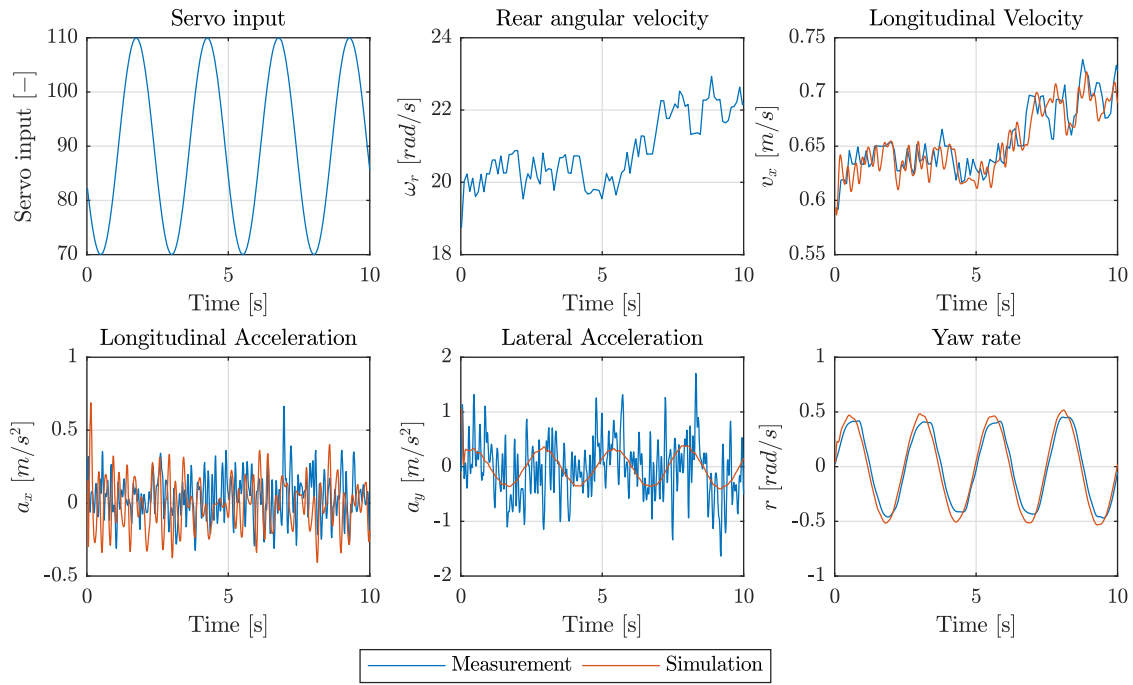


Figure A-27: Manoeuvre used for combined tyre dynamics estimation: Sine steering input. Frequency: 0.4 Hz, Steering input range: 70 – 110

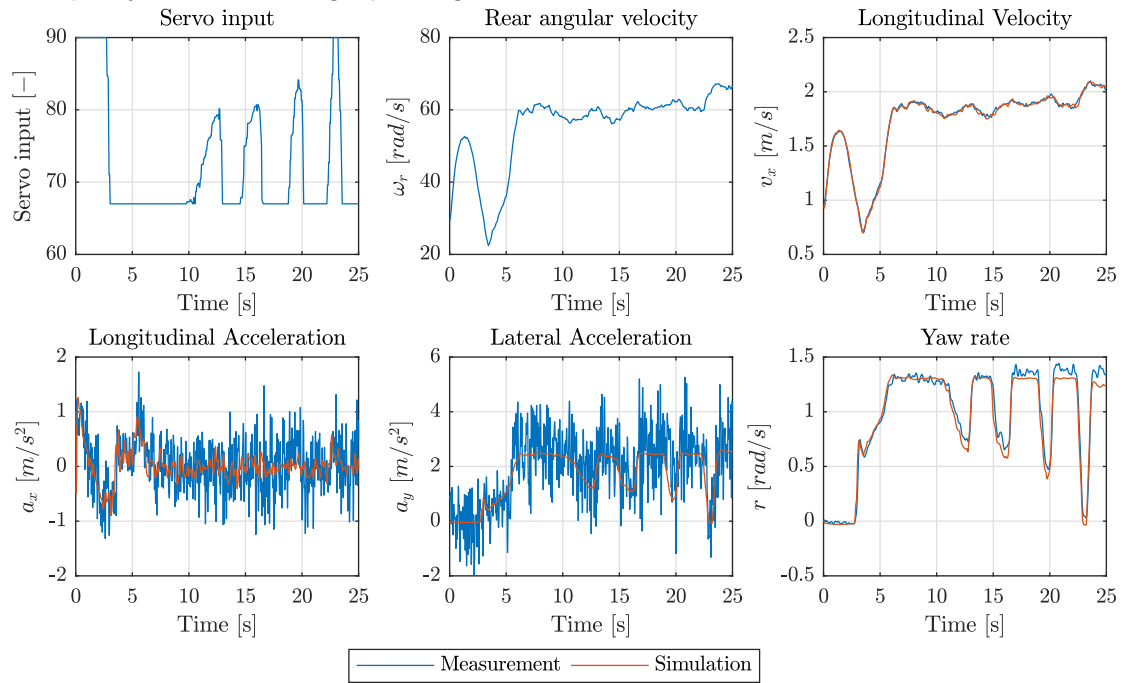


Figure A-28: Manoeuvre used for combined tyre dynamics estimation: Varying motor and steering inputs.

A-2-5 Full vehicle model validation

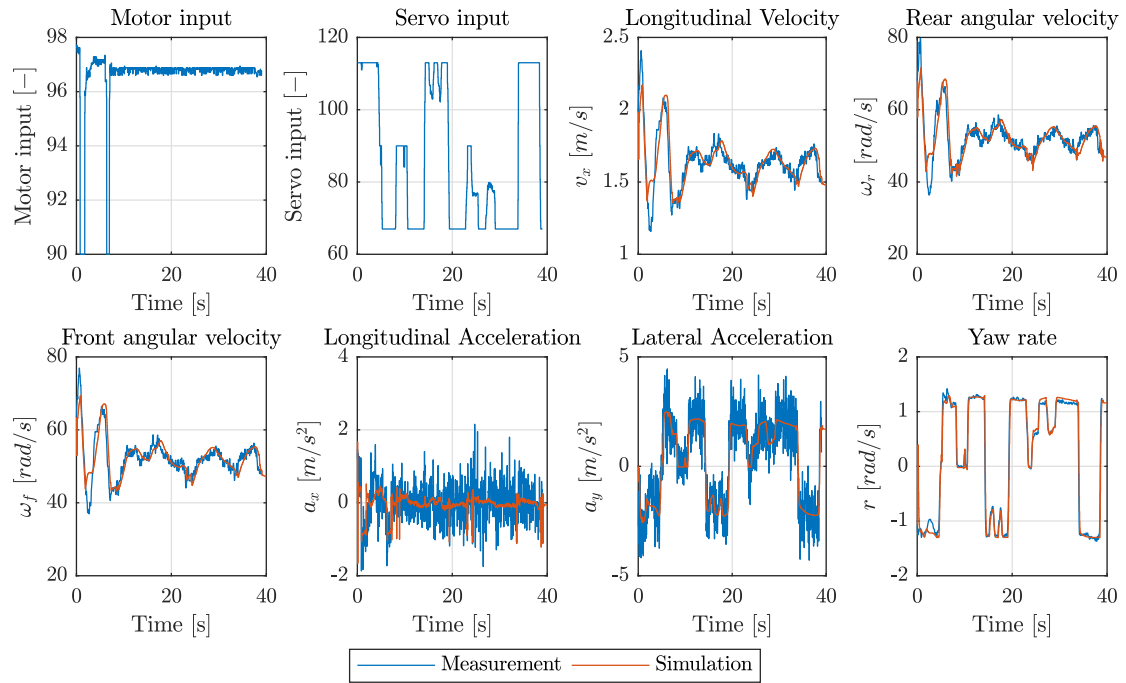


Figure A-29: Manoeuvre for motor parameters estimation: Varying steering inputs for a near constant motor input.

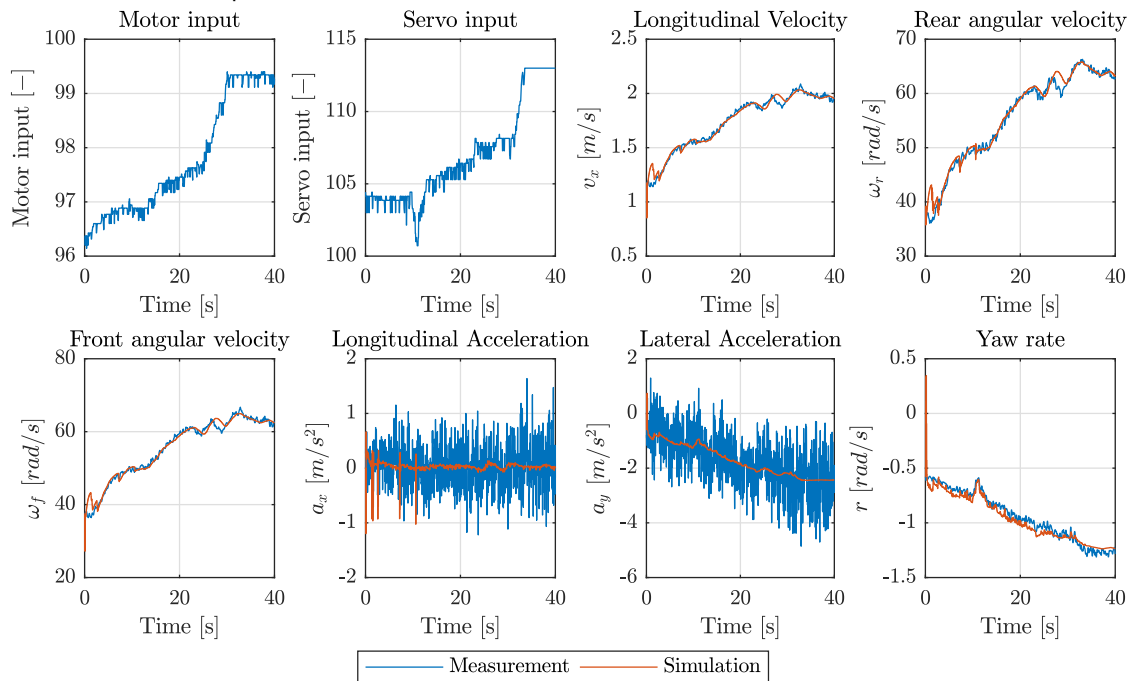


Figure A-30: Manoeuvre for motor parameters estimation: Circular driving with increasing motor input.

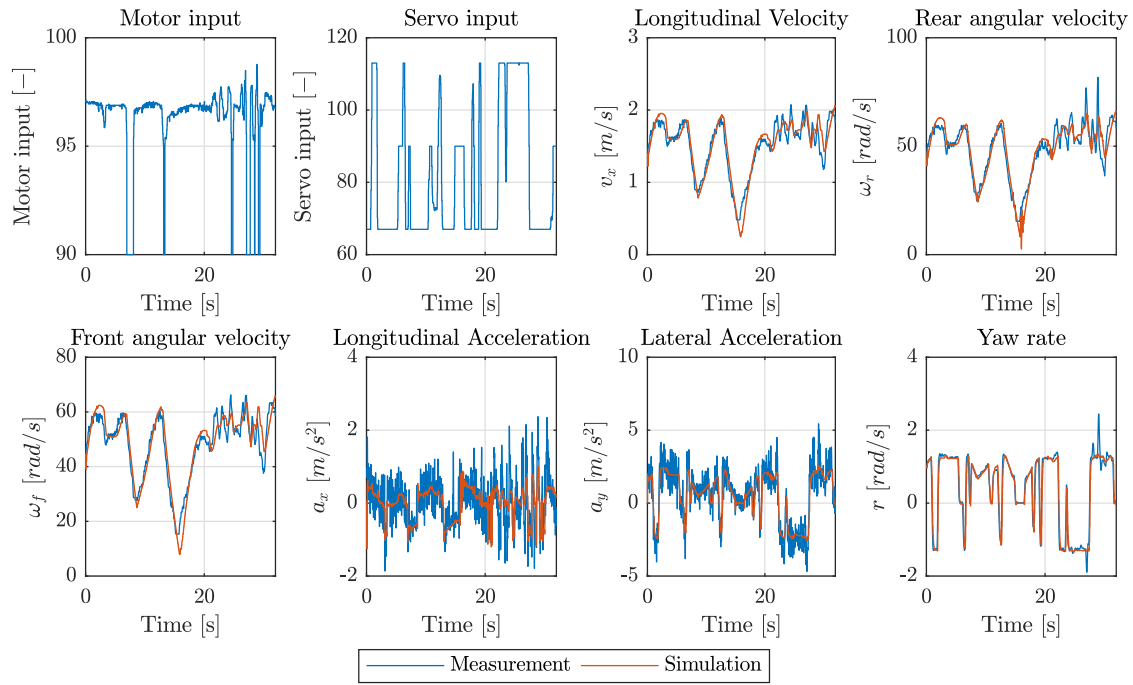


Figure A-31: Manoeuvre for motor parameters estimation: Varying motor and steering inputs.

Appendix B

Comparison between desired curvature definitions

In the figure below a comparison between the desired curvature used for the typical cornering controller and the drift controller are shown for a small corner radius. It can be observed that in most of the cases the curvature for typical cornering crosses the path before the look-ahead distance. The curvature used for the drift controller crosses the path with a smaller difference in angle, making it more 'gentile'. Note that for a positive lateral error and negative heading error, the curvature for the drift controller does not touch the path. Since the vehicle is moving towards the path, however, this is not a problem.

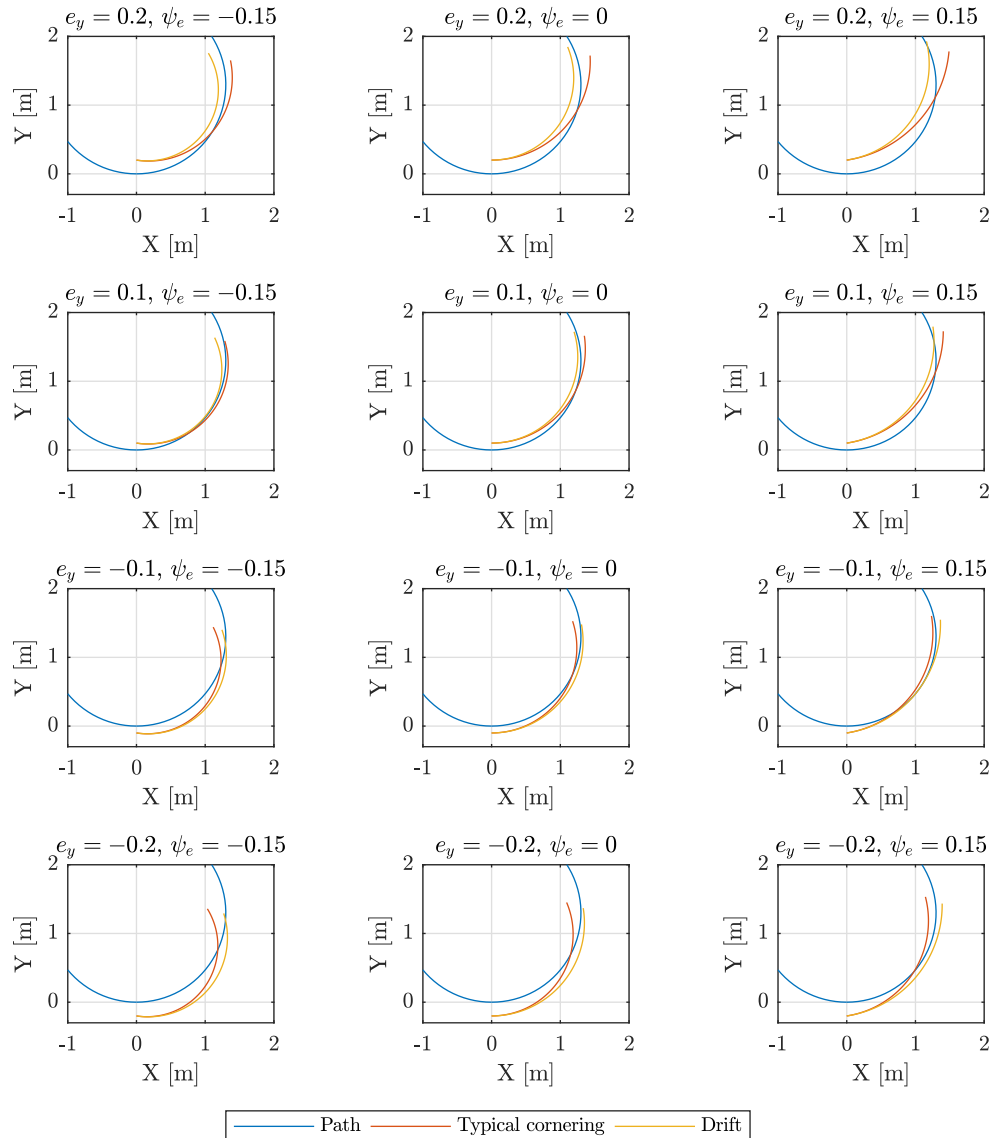


Figure B-1: Comparison between the desired curvature used in the typical cornering and drift controller for a small corner radius.

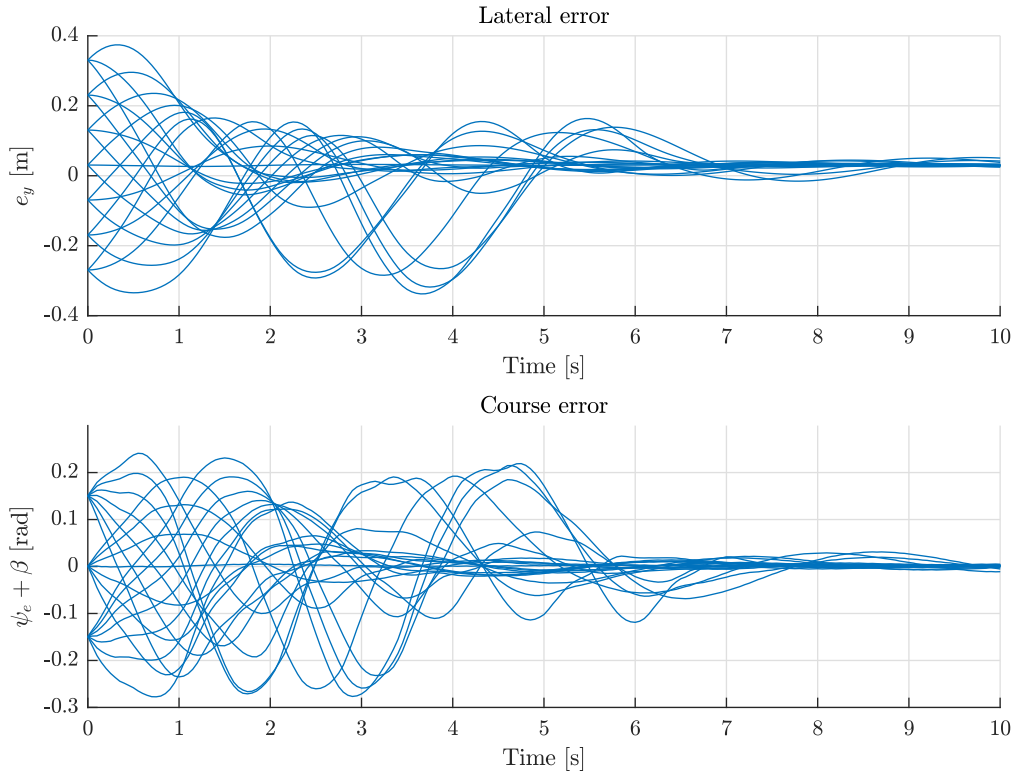


Figure B-2: Response of the path tracking errors for the drift controller with the modified desired curvature definition.

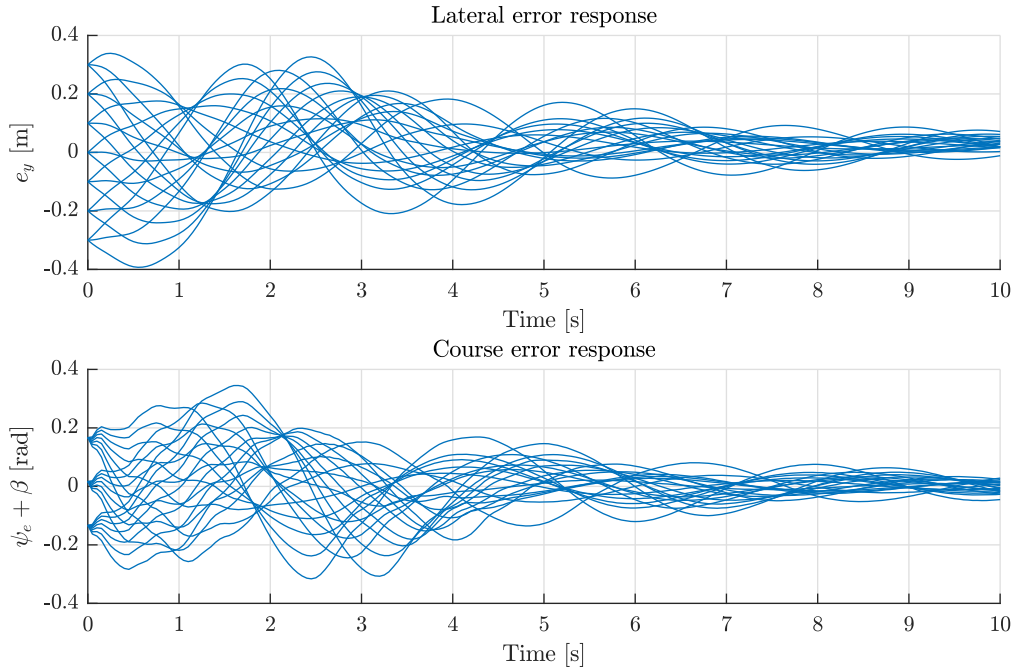


Figure B-3: Response of the path tracking errors for the drift controller with the original desired curvature definition.

Bibliography

- [1] WHO, “Global Status Report On Road Safety,” tech. rep., World Health Organization, 2015.
- [2] NHTSA, “Traffic Safety Facts,” Tech. Rep. February, National Highway Traffic Safety Administration, 2015.
- [3] L. T. Aarts, J. Commandeur, R. Welsh, S. Niesen, M. Lerner, P. Thomas, N. Bos, and R. J. Davidse, “Study on Serious Road Traffic Injuries in the EU,” Tech. Rep. October, European Commission, 2016.
- [4] J. Dang, “Statistical Analysis of the Effectiveness of Electronic Stability Control (ESC) Systems,” Tech. Rep. July, Department of Transportation National Highway Traffic Safety Administration Washington, DC 20590, 2007.
- [5] IRU, “IRU Position on Road Safety related Advanced Driver Assistance Systems (ADAS),” Tech. Rep. October, International Road Transport Union, 2013.
- [6] D. Wee and M. Bertoncello, “Ten ways autonomous driving could redefine the automotive world,” tech. rep., McKinsey&Company, 2015.
- [7] Waymo, “On the road to Fully Self-driving,” *Waymo Safety Report*, p. 43, 2017.
- [8] Y.-H. J. J. Hsu and J. C. Gerdes, “Stabilization of a Steer-by-Wire Vehicle at the Limits of Handling Using Feedback Linearization,” *Dynamic Systems and Control, Parts A and B*, vol. 2005, pp. 483–492, 2005.
- [9] K. M. Kritayakirana, “Autonomous vehicle control at the limits of handling,” no. June, 2012.
- [10] R. Y. Hindiyeh, “Dynamics and Control of Drifting in Automobiles,” no. March 2013, p. 223, 2013.
- [11] H. Dugoff, P. S. Fancher, and L. Segel, “Tire Performance Characteristics Affecting Vehicle Response to Steering and Braking Control Inputs,” vol. 460, 1969.

- [12] J. Edelmann and M. Plöchl, "Handling characteristics and stability of the steady-state powerslide motion of an automobile," *Regular and Chaotic Dynamics*, vol. 14, no. 6, pp. 682–692, 2009.
- [13] C. Voser, R. Hindiyeh, and J. Gerdés, "Analysis and Control of High Sideslip Manoeuvres," *Vehicle System Dynamics*, pp. 317–336, 2010.
- [14] A. Gray, Y. Gao, T. Lin, J. K. Hedrick, H. E. Tseng, and F. Borrelli, "Predictive Control for Agile Semi-Autonomous Ground Vehicles using Motion Primitives," pp. 4239–4244, 2012.
- [15] A. Arab, K. Yu, J. Yi, and Y. Liu, "Motion Control of Autonomous Aggressive Vehicle Maneuvers," vol. 1, pp. 1663–1668, 2016.
- [16] E. Wachter, "Lateral Path Tracking in Limit Handling Condition using SDRE Control," 2016.
- [17] D. E. Smith and J. M. Starkey, "Effects of Model Complexity on the Performance of Automated Vehicle Steering Controllers : Model Development , Validation and Comparison Effects of Model Complexity on the Performance of Automated Vehicle Steering Controllers : Model Development , Validat," vol. 3114, no. June, 1995.
- [18] N. D. Smith, "Understanding parameters influencing tire modeling," *2004 Formula SAE Platform*, p. 22, 2004.
- [19] H. B. Pacejka, *Tyre and vehicle dynamics*. Butterworth-Heinemann, 2006.
- [20] M. Bian, L. Chen, Y. Luo, and K. Li, "A Dynamic Model for Tire / Road Friction Estimation under Combined Longitudinal / Lateral Slip Situation Analysis on Dugoff Tire Model," *SAE Technical Papers*, no. May 2015, p. 6, 2015.
- [21] B. Niessen, S. Jansen, I. Besselink, A. Schmeitz, and H. Nijmeijer, "An enhanced generic single track vehicle model and its parameter identification for 15 different passenger cars," in *Presentation at the 11th inter- national symposium on advanced vehicle control (AVEC '12)*, 2012.
- [22] D. L. Edwards, "Parameter Estimation Techniques for Determining Safe Vehicle Speeds in UGVs," 2008.
- [23] S. Tsugawa, "An overview on control algorithms for automated highway systems," *Proceedings 199 IEEE/IEEJ/JSAI International Conference on Intelligent Transportation Systems (Cat. No.99TH8383)*, pp. 234–239, 1999.
- [24] S. Patwardhan, H.-S. Tan, and J. Guldner, "A General Framework for Automatic Steering Control: System Analysis," *Proceedings of the 1997 American Control Conference (Cat. No.97CH36041)*, vol. 3, pp. 1598–1602, 1997.
- [25] J.-C. Hsu and M. Tomizuka, "Analyses of Vision-based Lateral Control for Automated Highway System," *Vehicle System Dynamics*, vol. 30, no. 5, pp. 345–373, 1998.

- [26] J. Kosecka, R. Blasi, C. Taylor, and J. Malik, “A comparative study of vision-based lateral control strategies for autonomous highway driving,” *Proceedings. 1998 IEEE International Conference on Robotics and Automation (Cat. No.98CH36146)*, vol. 3, no. May, pp. 442–453, 1998.
- [27] P. Hingwe and M. Tomizuka, “A variable look-ahead controller for lateral guidance of four wheeled vehicles,” *Proceedings of the American Control Conference*, vol. 1, no. June, pp. 31–35, 1998.
- [28] N. R. Kapania and J. C. Gerdes, “Design of a feedback-feedforward steering controller for accurate path tracking and stability at the limits of handling,” *Vehicle System Dynamics*, vol. 53, no. 12, pp. 1687–1704, 2015.
- [29] A. Schmeitz, J. Zegers, J. Ploeg, and M. Alirezaei, “Towards a generic lateral control concept for cooperative automated driving,” in *5th IEEE International Conference on Models and Technologies for Intelligent Transportation Systems, At Naples*, 2017.
- [30] “How to drift - Drivingfast.net.”. Retrieved from <http://www.drivingfast.net/drifting/> (Accessed at 2018-04-27)
- [31] “hector_slam - ROS Wiki.”. Retrieved from http://wiki.ros.org/hector_slam (Accessed at 2018-03-10)

Glossary

List of Acronyms

| | |
|---------------|---------------------------------------|
| DCSC | Delft Center for Systems and Control |
| DSV | Delft Scaled Vehicle |
| DOF | degrees of freedom |
| IMU | Inertial Measurement Unit |
| ESC | Electric Speed Controller |
| PWM | Pulse Width Modulation |
| RC | Radio Controlled |
| SLAM | Simultaneous Localization And Mapping |
| Lidar | Light Detection And Ranging |
| ROS | Robotic Operating System |
| COG | Centre of Gravity |
| NMPC | Nonlinear Model Predictive Control |
| SDRE | State-Dependent Riccati Equation |
| Mo-cap | Motion capture |

List of Symbols

Greek Symbols

| | |
|------------|--------------------------------|
| α_j | Wheel slip angle for wheel j |
| β | Body sideslip angle |

| | |
|-----------------|---|
| β_{ss} | Steady-state body sideslip angle |
| δ | Steering angle |
| κ_p | Path curvature |
| λ_j | Longitudinal slip coefficient for wheel j |
| ψ_e | Heading error |
| $\sigma_{rl,i}$ | Relaxation length for direction i |

Roman Symbols

| | |
|-------------|--|
| δ_s | Servo angle |
| ℓ | Wheel base |
| μ_{max} | Maximum tyre-road friction coefficient |
| a | Distance from centre of gravity to front axle |
| a_i | Acceleration in direction i |
| b | Distance from Centre of Gravity (COG) to rear axle |
| C_α | Lateral tyre stiffness |
| C_σ | Longitudinal tyre stiffness |
| e_y | Lateral path-tracking error |
| e_{la} | Look-ahead error |
| $F_{i,j}$ | Tyre force in direction i of wheel j |
| h | Height of the COG |
| I_w | Wheel angular moment of inertia |
| I_z | Yaw moment of inertia |
| $I_{w,f}$ | Front axle moment of inertia per wheel |
| $I_{w,r}$ | Rear axle moment of inertia per wheel |
| m | Vehicle mass |
| r | Yaw rate |
| t | Axle track |
| $T_{f,dyn}$ | Torque resulting from dynamic wheel friction |
| $T_{f,st}$ | Torque resulting from static friction |
| T_f | Torque acting on a wheel, resulting from friction |
| t_{la} | Look-ahead time |
| T_m | Torque input from the motor to a wheel |
| u_s | Steering servo input |
| u_t | Throttle input |
| v | Absolute vehicle velocity at the COG |
| v_i | Velocity in direction i |
| v_{des} | Desired absolute velocity |
| $v_{x,j}$ | Longitudinal velocity of wheel j |
| $v_{y,j}$ | Lateral velocity of wheel j |
| x_{la} | Look-ahead distance |
| g | Gravitational Acceleration |

Subscripts

| | |
|------|--|
| fl | Front-left wheel |
| fr | Front-right wheel |
| f | Combined front wheels |
| i | Identifier for direction x,y or z |
| j | Identifier for wheel fl,fr,rl or rr or combined wheels f and r |
| rl | Rear-left wheel |
| rr | Rear-right wheel |
| r | Combined rear wheels |
| x | Longitudinal direction |
| y | Lateral direction |
| z | Vertical direction |

Superscripts

| | |
|------|--|
| d | Gain belonging to the drift controller |
| eq | Equilibrium state value |
| tc | Gain belonging to the typical cornering controller |